

# Soft Inflatable Robotic Systems for Space Applications: A Survey

## Abstract

Soft inflatable robotic systems and structures are emerging as transformative technologies for space applications, offering compelling advantages in mass efficiency, compact stowage, compliance, and adaptability over traditional rigid-body systems. This survey provides a comprehensive review of the intersection of soft robotics, inflatable structures, and space engineering, organised around a unifying thesis: the same high-strength fabric technologies (Vectran, Kevlar, Nextel) that enable inflatable habitats also enable compliant debris capture mechanisms and large deployable shields. We examine two primary application domains—active debris removal, where soft compliant systems address the fragmentation paradox inherent in rigid capture, and space exploration, where inflatable habitats offer order-of-magnitude mass efficiency improvements over metallic modules. Eight enabling technology areas are reviewed: materials and structures, deployment mechanics, actuation, sensing and structural health monitoring, power systems, thermal management, attitude and orbit control, and robotic in-orbit assembly. We identify five critical research gaps, including the absence of quantitative soft-versus-rigid fragmentation comparisons, the lack of flight heritage for soft robotic capture, and the unexplored rigid-to-flexible assembly interface. A research roadmap spanning 5-year and 15-year horizons is proposed, with the most flight-ready near-term demonstrator identified as a gecko-adhesive gripper on an inflatable arm with fibre Bragg grating structural health monitoring. This survey differentiates itself from prior reviews in Progress in Aerospace Sciences by focusing specifically on soft and inflatable systems—a technology class not covered by existing reviews of rigid space robotics or contact/contactless debris removal.

## Contents

<b>1</b>	<b>Introduction</b>	<b>4</b>
<b>2</b>	<b>The Case for Soft Inflatables in Space</b>	<b>8</b>
2.1	Space Debris Crisis and the Need for Active Removal . . . . .	8
2.2	Human Exploration Beyond LEO: The Habitat Challenge . . . . .	11
2.3	Unifying Thesis: Shared Fabric Technology Across Applications . . . . .	12

33	<b>3 Use Cases: Active Debris Removal</b>	<b>15</b>
34	3.1 Rigid Capture Approaches and Fragmentation Risk	15
35	3.1.1 The Fragmentation Paradox	16
36	3.2 Soft and Compliant Capture Mechanisms	17
37	3.2.1 Gecko-Inspired Dry Adhesive Grippers	17
38	3.2.2 Dielectric Elastomer Minimum Energy Structure (DEMES) Grippers	19
39	3.2.3 Bistable and Passive Capture Grippers	19
40	3.2.4 Thermally Qualified Soft Grippers	20
41	3.2.5 Inflatable Robotic Arms for Capture	20
42	3.2.6 INSIDeR: Net Capture with Inflatable Deployment	20
43	3.3 Inflatable Debris Shields	23
44	<b>4 Use Cases: Habitats and Exploration</b>	<b>23</b>
45	4.1 Heritage Timeline: Echo to BEAM	24
46	4.1.1 Early Inflatables: Echo and Volga (1960–1965)	26
47	4.1.2 TransHab: Proving the Five-Layer Architecture (1997–2000)	26
48	4.1.3 Genesis and BEAM: Orbital Validation (2006–2016+)	27
49	4.2 Current Commercial Programs: LIFE, Orbital Reef, and Beyond	27
50	4.2.1 Sierra Space LIFE	27
51	4.2.2 Historical Context: B330 and Commercial Ecosystem Fragility	28
52	4.2.3 NextSTEP Competitive Landscape	28
53	4.3 Future Concepts: Lunar Surface, Mars Transit, Planetary Entry	28
54	4.3.1 Lunar Surface Habitats	28
55	4.3.2 Mars Transit and Surface Applications	29
56	4.3.3 European Programmes	29
57	4.4 Radiation Shielding: The BEAM SPE Findings and Design Implications	30
58	<b>5 State of the Art: Materials and Structures</b>	<b>31</b>
59	5.1 Space-Rated Fabrics: Vectran, Kevlar, Zylon, Nextel	31
60	5.2 Multi-Layer Shell Architecture	33
61	5.3 Rigidization Technologies	37
62	5.4 Environmental Degradation: AO, UV, Radiation, Creep	38
63	<b>6 State of the Art: Deployment Mechanics</b>	<b>39</b>
64	6.1 Fold Patterns and Packaging Efficiency	39
65	6.2 Inflation Sequencing and Control	39
66	6.3 Flight Heritage: InflateSail, LOFTID, BEAM Deployment Lessons	41
67	6.4 Comparison with Rigid Deployable Alternatives	42
68	<b>7 State of the Art: Actuation for Soft Space Systems</b>	<b>43</b>
69	7.1 Dielectric Elastomer Actuators and DEMES	43
70	7.2 Vacuum-Gap Electrostatic Actuators: Vacuum as Enabler	44
71	7.3 Ionic Electroactive Polymers: Space Tolerance Assessment	45
72	7.4 Tendon-Driven Continuum Manipulators	45
73	7.5 Shape Memory Alloys for Deployment	46

74	7.6	Jamming in Vacuum: A Novel Opportunity . . . . .	46
75	7.7	Sealed Pneumatic Actuation in Space . . . . .	48
76	7.8	Electroadhesion and Magnetic Actuation: Emerging Approaches . . . . .	48
77	<b>8</b>	<b>State of the Art: Sensing and Structural Health Monitoring</b>	<b>49</b>
78	8.1	Fibre Bragg Grating Sensors: From Proba-2 to Inflatable Webbing . . . . .	49
79	8.2	Multicore Fibre Optic Shape Sensing . . . . .	52
80	8.3	Capacitive, Resistive, and Alternative Soft Sensors . . . . .	52
81	8.4	Distributed Fibre Optic Sensing: Rayleigh and Brillouin Scattering . . . . .	53
82	8.5	Distributed Impact Detection . . . . .	53
83	<b>9</b>	<b>State of the Art: Power Systems for Large Inflatables</b>	<b>54</b>
84	9.1	Flexible Solar Array Landscape: ROSA to Perovskite . . . . .	54
85	9.2	The Inflatable-Power Integration Gap: PowerSphere and Beyond . . . . .	56
86	9.3	Energy Storage: Li-ion, RFC, and Mission-Dependent Selection . . . . .	57
87	<b>10</b>	<b>State of the Art: Thermal Management</b>	<b>58</b>
88	10.1	Multi-Layer Insulation for Inflatable Shells . . . . .	58
89	10.2	The JWST Sunshield as Deployable Thermal Barrier Precedent . . . . .	59
90	10.3	Variable Emissivity Coatings and Smart Radiators . . . . .	60
91	10.4	Loop Heat Pipes for Deployed Structures . . . . .	61
92	10.5	Phase Change Materials in Fabric Layers: The TRL 2–3 Gap . . . . .	61
93	<b>11</b>	<b>State of the Art: Attitude and Orbit Control</b>	<b>62</b>
94	11.1	Control-Structure Interaction for Flexible Spacecraft . . . . .	63
95	11.2	Gyroelastic Body Theory and Distributed Momentum Management . . . . .	63
96	11.3	Drag Budget for 100 m-Class LEO Structures . . . . .	64
97	11.4	The Missing Theory: AOCS for Pressure-Stabilised Membranes . . . . .	66
98	<b>12</b>	<b>State of the Art: Robotic In-Orbit Assembly</b>	<b>67</b>
99	12.1	Assembly Robot Heritage and Current Programmes . . . . .	68
100	12.2	Walking Robots for Large Structure Assembly: E-Walker . . . . .	68
101	12.3	The Rigid-to-Flexible Interface Gap . . . . .	69
102	12.4	Assembly-Enabled Inflatable Platforms: Design Requirements . . . . .	70
103	<b>13</b>	<b>Challenges, Open Questions, and Research Roadmap</b>	<b>71</b>
104	13.1	Critical Research Gaps . . . . .	71
105	13.2	Integration Challenges at System Level . . . . .	74
106	13.3	Proposed Research Roadmap: 5-Year and 15-Year Horizons . . . . .	75
107	13.4	The Path to Flight Demonstration . . . . .	79
108	<b>14</b>	<b>Conclusions</b>	<b>80</b>

# 1 Introduction

Two converging pressures threaten humanity’s long-term access to and presence in space. The first is the accelerating degradation of the orbital environment: the low Earth orbit (LEO) regime is increasingly populated with debris that endangers operational satellites, whose services — from climate monitoring to navigation — underpin the global economy. The second is the ambition for sustained human exploration beyond LEO, which demands habitable volumes an order of magnitude larger than current metallic modules allow within existing launch vehicle constraints. This survey argues that a single technology class — soft inflatable robotic systems based on high-strength technical fabrics — offers a coherent engineering response to both challenges through a shared material and structural foundation.

The orbital debris environment has reached a critical threshold. The European Space Agency’s 2025 Space Environment Report records approximately 44,870 tracked objects, with an estimated 54,000 objects larger than 10 cm, some 1.2 million objects between 1 and 10 cm, and an estimated 140 million fragments between 1 mm and 1 cm, totalling roughly 15,800 tonnes of mass in orbit [ESA Space Debris Office \[2025\]](#). The consequence is operational: SpaceX’s Starlink constellation executed 144,404 collision avoidance manoeuvres in the first half of 2025 alone, a 65-fold increase relative to 2021 [ESA Space Debris Office \[2025\]](#). Kessler and Cour-Palais identified in 1978 that mutual collision among catalogued objects could generate a self-sustaining fragment cascade [Kessler and Cour-Palais \[1978\]](#), and Liou and Johnson subsequently demonstrated with the LEGEND simulation suite that the current LEO population is already gravitationally unstable: even with a complete halt to new launches, the debris environment continues to grow through inter-object collisions [Liou and Johnson \[2006, 2008\]](#). Stabilising LEO requires the active removal of at least five large, rocket-body-class objects per year from the most critical orbital shells [Liou et al. \[2010\]](#).

Active Debris Removal (ADR) therefore transitions from a conceptual aspiration to an operational necessity. Yet the dominant design paradigm — rigid robotic arms similar to ClearSpace-1’s four-arm capturing system — carries an ironic risk: forceful contact with a tumbling, uncooperative object can fracture it, generating new fragments faster than they are removed. Simulation studies and ground tests indicate that peak joint torques of order 195 Nm can arise during ENVISAT-class capture operations [Ledkov and Aslanov \[2022\]](#), and the RemoveDebris harpoon demonstration saw a carbon-fibre boom snap on contact at 20 m/s [Aglietti et al. \[2020\]](#). The fragmentation paradox — rigid capture risks accelerating the very cascade it aims to halt — provides the primary motivation for compliant, soft capture architectures.

Simultaneously, the ambition to sustain human presence beyond LEO confronts a fundamental mass budget constraint. Metallic pressurised modules — Columbus (137 kg/m<sup>3</sup>) and Tranquility (205 kg/m<sup>3</sup>) — are delivered at densities an order of magnitude higher than fabric-based alternatives such as the TransHab concept (39 kg/m<sup>3</sup>) [Valle et al. \[2019a\]](#). Vectran high-tenacity yarn achieves a specific strength of 2,330 kN-m/kg, versus 220 kN-m/kg for Ti-6Al-4V [Valle et al. \[2019a\]](#) — a 10× advantage that directly translates to launch mass savings. The Bigelow Expandable Activity Module (BEAM), attached to the International Space Station (ISS) since 2016, has accumulated more than eight years of continuous pressurised operation on the ISS, with periodic crew access for inspection and cargo storage, at Technology Readiness Level (TRL) 9 [NASA Johnson Space Center \[2017\]](#).

153 The organising thesis of this survey is that the same high-strength fabric technology  
154 — Vectran restraint layers, Kevlar/Nextel debris shielding, Kapton thermal insulation —  
155 that enables BEAM’s pressure vessel integrity also enables compliant robotic capture arms,  
156 large deployable debris shields, and the next generation of deep-space habitats. Material  
157 qualification campaigns, manufacturing processes, and design heritage are shared across  
158 these application domains, providing an unusually coherent pathway from current flight-  
159 proven technology to future operational systems.

## 160 Scope and Organisation

161 This survey reviews the intersection of three mature fields: soft robotics, inflatable space  
162 structures, and the enabling subsystem technologies (materials, power, thermal manage-  
163 ment, attitude and orbit control, and robotic assembly) that together determine whether  
164 soft inflatable systems can be realised at mission-operational scale. The scope spans two  
165 primary application domains:

- 166 1. **Active Debris Removal** — soft and compliant capture mechanisms (TRL 2–5) and  
167 large inflatable debris shields (design stage), examined against the rigid-capture base-  
168 line.
- 169 2. **Human Space Exploration** — the heritage from Echo 1 (1960) through BEAM  
170 (2016+) to current commercial programmes (Sierra Space LIFE, Orbital Reef), and  
171 future concepts for lunar surface, Mars transit, and planetary entry decelerators.

172 Eight enabling technology areas are reviewed in depth: (1) materials and structures,  
173 (2) deployment mechanics, (3) actuation, (4) sensing and structural health monitoring,  
174 (5) power systems, (6) thermal management, (7) attitude and orbit control, and (8) robotic  
175 in-orbit assembly. The survey concludes with a consolidated gap analysis and a research  
176 roadmap spanning 5-year and 15-year horizons.

## 177 Relationship to Existing Reviews

178 Three prior surveys in *Progress in Aerospace Sciences* address adjacent territory, and this  
179 survey is positioned explicitly as their complement (Table 1). Flores-Abad et al. reviewed the  
180 state of space robotics for on-orbit servicing in 2014 Flores-Abad et al. [2014], establishing  
181 the four-phase capture framework (approach, tracking, capture, post-capture stabilisation)  
182 that remains the standard reference; however, that work predates the current wave of soft  
183 robotics innovation and does not address inflatable structures. Ledkov and Aslanov surveyed  
184 contact and contactless ADR approaches in 2022 Ledkov and Aslanov [2022], providing com-  
185 prehensive coverage of nets, harpoons, ion beam shepherds, and electrodynamic tethers, but  
186 soft and compliant capture mechanisms receive minimal treatment and inflatable structures  
187 for ADR are absent. Zhao et al. reviewed rigid robotic manipulators for in-orbit servicing and  
188 ADR in 2024 Zhao et al. [2024], covering Denavit-Hartenberg kinematics, impedance control,  
189 and comparative arm performance; soft and inflatable manipulators are outside scope.

190 The most relevant prior survey is Zhang et al. (2023), who examined soft robotics for  
191 space across actuation, sensing, and manipulation Zhang et al. [2023a]. That work identifies

192 vacuum as a challenge for pneumatic actuation and catalogues the soft gripper landscape;  
 193 however, it does not cover the inflatable structure platform on which soft robots operate, nor  
 194 the enabling subsystems (power, thermal, AOCS, assembly) necessary for mission viability,  
 195 nor the dual ADR-and-exploration organising principle developed here.

196 The unique contribution of this survey is threefold. First, it covers eight enabling tech-  
 197 nology areas through a single integrative lens, rather than the one or two areas addressed  
 198 by prior reviews. Second, it presents the first unified treatment of both ADR and explo-  
 199 ration applications as manifestations of the same fabric-based technology class. Third, it  
 200 maps cross-domain connections — between, for example, thermal management and actuator  
 201 design, or fold patterns and debris protection — that can only be identified from a broad  
 202 survey perspective.

Table 1: Comparison of this survey with prior reviews in *Progress in Aerospace Sciences* covering adjacent domains. ✓ = covered; – = not covered; ~ = partial coverage.

Topic	This survey	Zhao 2024	Ledkov 2022	Flores-Abad 2014
Soft/compliant capture	✓	–	~	–
Inflatable robotic arms	✓	–	–	–
Inflatable debris shields	✓	–	–	–
Inflatable habitats	✓	–	–	–
Rigid ADR approaches	~	✓	✓	✓
Rigid manipulators	~	✓	~	✓
Materials & fabrics	✓	–	–	–
Power systems	✓	–	–	–
Thermal management	✓	–	–	–
AOCS for large structures	✓	–	–	–
Robotic in-orbit assembly	✓	~	–	~
Sensing & SHM	✓	–	–	–
Deployment mechanics	✓	–	–	–
<b>Year</b>	2026	2024	2022	2014
<b>Soft/inflatable focus</b>	Primary	None	Minimal	None

## 203 The Paradigm Shift: Vacuum as Design Resource

204 A recurring theme throughout this survey is the inversion of the conventional assumption  
 205 that space vacuum is hostile to soft robotic systems. Three independent developments chal-  
 206 lenge this assumption. First, Sirbu et al. demonstrated vacuum-gap electrostatic multilayer  
 207 actuators in 2025 that *require* vacuum to function: thin-film polymer multilayers with inter-  
 208 nal vacuum gaps zip closed on electrical activation, producing forces exceeding 4 N from a  
 209 0.7 g actuator at bandwidths above 100 Hz [Sirbu et al. \[2025\]](#). On Earth, a vacuum pump  
 210 would be required to create this operating condition; in space, the environment provides it  
 211 at no mass or power cost. Second, the confining pressure for granular and layer jamming —  
 212 which terrestrially requires evacuating a sealed membrane with a pump — is provided for

213 free by the ambient vacuum differential against a pressurised inflatable interior [Fitzgerald](#)  
214 [et al. \[2020\]](#). Third, DEMES gripper geometry provides a passive negative feedback loop  
215 in microgravity: grip force increases as a floating target drifts away from the actuator tip,  
216 offering passive capture stability without active control — a property that is useful only in  
217 the microgravity environment [Araromi et al. \[2015\]](#).

218 These developments suggest that soft inflatable robotic systems are not merely terrestrial  
219 technology adapted for space, but a distinct engineering discipline with unique environment-  
220 enabled advantages.

## 221 **Review Methodology**

222 The literature for this survey was assembled through a structured search strategy span-  
223 ning multiple databases and source types. Primary databases searched include Scopus,  
224 Web of Science, NASA Technical Reports Server (NTRS), ESA’s publication repository, and  
225 Google Scholar, using the following search term families: (i) “inflatable space structure”  
226 OR “expandable habitat” OR “deployable membrane”; (ii) “soft robot\*” AND “space” OR  
227 “orbital”; (iii) “active debris removal” AND (“compliant” OR “soft” OR “inflatable”); and  
228 (iv) technology-specific terms for each of the eight enabling areas (e.g., “dielectric elastomer  
229 actuator space,” “fibre Bragg grating spacecraft,” “perovskite solar cell radiation”). The tem-  
230 poral scope spans 1960 (Project Echo) to early 2026, with no lower date restriction applied.  
231 Inclusion criteria required that sources address at least one of the two application domains  
232 (ADR or exploration) or one of the eight enabling technology areas in a space-relevant con-  
233 text. Conference proceedings were included when they represented the primary publication  
234 venue for mission results (e.g., AIAA, IAC, IEEE Aerospace). NASA technical memoranda,  
235 ESA reports, and agency mission documentation were included for heritage programme data  
236 not available in peer-reviewed form. Corporate press releases and datasheets were included  
237 only when no peer-reviewed alternative existed for specific mission or material property  
238 data. The eight technology areas were selected based on a preliminary scoping review that  
239 identified all subsystem-level capabilities required for an operational soft inflatable robotic  
240 system at mission scale, following the principle that reviews in *Progress in Aerospace Sci-*  
241 *ences* should enable the reader to assess system-level feasibility rather than component-level  
242 performance alone. TRL assessments throughout the paper follow the NASA NPR 7123.1B  
243 standard definitions [NASA \[2020\]](#).

## 244 **Survey Statistics**

245 This survey reviews approximately 120 primary sources spanning the period from 1960 to  
246 2026. Of these, approximately 74% are peer-reviewed journal papers or conference pro-  
247 ceedings from indexed venues; the remainder comprises NASA technical memoranda, ESA  
248 reports, and agency mission documentation. Coverage extends across eight technology areas  
249 and two application domains, with the deepest literature pools in actuation (Zhang 2023 and  
250 its references), inflatable habitats (Litteken 2019 and the TransHab programme), and space  
251 debris (Kessler 1978 through ESA 2025). The survey is organised with application use cases  
252 preceding the technology state-of-the-art review, following the principle that applications  
253 should motivate the technology landscape rather than the reverse.

## 2 The Case for Soft Inflatables in Space

### 2.1 Space Debris Crisis and the Need for Active Removal

The accumulation of orbital debris is the defining environmental challenge of the space age. Since Sputnik-1’s launch in 1957, every mission has contributed to a growing cloud of defunct satellites, spent rocket stages, and collision fragments. The debris environment is now characterised not merely by nuisance but by irreversible instability.

#### Current Debris Environment

The ESA Space Environment Report for 2025 provides the most current comprehensive characterisation [ESA Space Debris Office \[2025\]](#). As of early 2026, approximately 44,870 objects are tracked by ground-based surveillance networks, of which roughly one third are operational satellites and two thirds are debris. The total catalogued population has grown by more than 3,000 objects from fragmentation events in 2024 alone. At altitudes between 500 and 700 km — where ADR missions are most urgently needed — debris density is comparable to or exceeds the density of active satellites.

Table 2: Current LEO debris population by size category (data from ESA Space Environment Report 2025 [ESA Space Debris Office \[2025\]](#)).

Size category	Estimated count	Trackable?	Primary threat
> 10 cm	~54,000	Yes (radar)	Catastrophic collision
1–10 cm	~1,200,000	No	Mission-ending damage
1 mm – 1 cm	~140,000,000	No	Surface/solar panel damage
< 1 mm	> 10 <sup>12</sup>	No	Erosion/coating damage
Total mass	~15,800 tonnes	–	–

More than 650 fragmentation events have occurred in orbit since 1961, with significant contributors including the 2007 Chinese ASAT test (Fengyun-1C), the 2009 Cosmos-Iridium collision, and the 2021 Russian ASAT test (Cosmos-1408). These events collectively added thousands of trackable fragments and orders of magnitude more sub-centimetre particles.

#### The Kessler Syndrome: From Prediction to Confirmation

Kessler and Cour-Palais (1978) predicted that beyond a critical debris density, mutual collisions among catalogued objects would generate fragments faster than atmospheric drag could remove them, leading to an exponential growth cascade now called the Kessler syndrome [Kessler and Cour-Palais \[1978\]](#). For nearly three decades this remained a theoretical concern. Liou and Johnson (2006) demonstrated with the LEGEND orbital debris evolution model that the predicted threshold has already been crossed in the 800–1000 km altitude band: even if all future launches were halted immediately, the debris population in these shells would continue to grow due to existing collision rates among currently catalogued objects [Liou and Johnson \[2006\]](#). Extended 200-year projections (Liou and Johnson 2008)

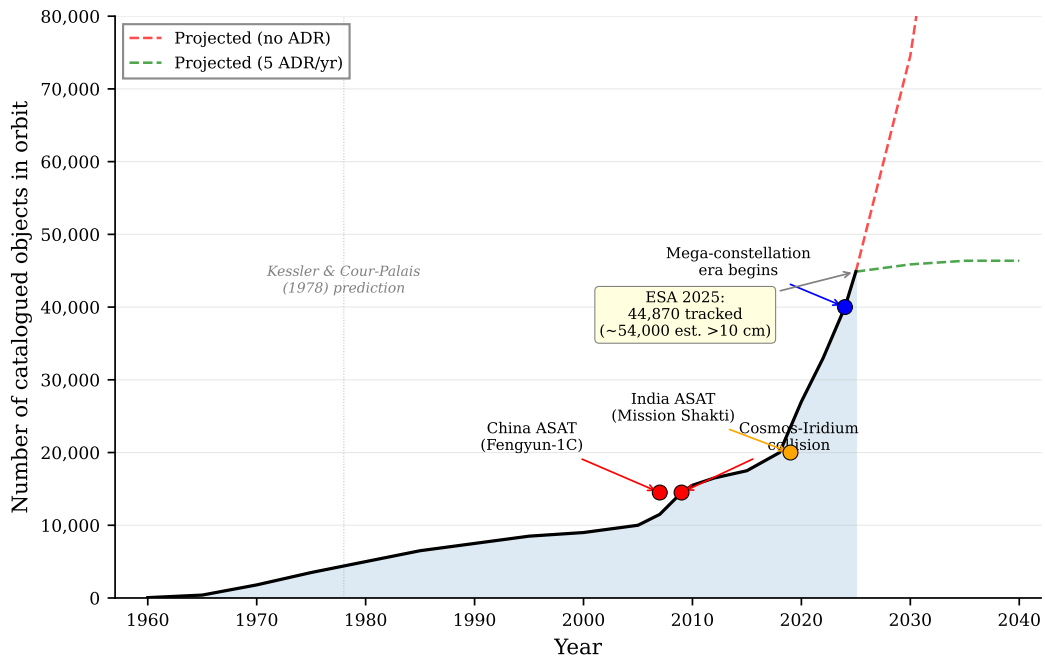


Figure 1: Growth of the catalogued orbital debris population from 1960 to 2025, with projections to 2040. Discrete fragmentation events (Chinese ASAT 2007, Cosmos-Iridium collision 2009) are visible as step increases. Red dashed line: projected growth without active debris removal. Green dashed line: projected stabilisation with five large-object removals per year [Liou et al. \[2010\]](#). Data from ESA Space Environment Report 2025 [ESA Space Debris Office \[2025\]](#).

282 confirmed that the instability is neither transient nor recoverable without active interven-  
283 tion [Liou and Johnson \[2008\]](#).

284 The required rate of removal has been quantified. Liou et al. (2010) showed that removing  
285 at least five large objects per year (primarily rocket bodies in the 800–1000 km band) is nec-  
286 essary and sufficient to stabilise the LEO population over a 200-year projection horizon [Liou](#)  
287 [et al. \[2010\]](#). This represents an annual ADR cadence comparable to the total number of sig-  
288 nificant deorbit missions conducted globally over the past decade — a formidable operational  
289 challenge.

## 290 The Fragmentation Paradox

291 The dominant design approach to ADR — rigid robotic arms, exemplified by ESA’s ClearSpace-  
292 1 mission targeting the PROBA-1 satellite — faces a fundamental tension. Rigid contact  
293 with a non-cooperative, tumbling debris object generates impulsive forces at the contact  
294 interface. For an 8-tonne ENVISAT-class object rotating at 5 deg/s, e.deorbit trajectory  
295 analyses reveal peak joint torques of 195 Nm at structural limits [Ledkov and Aslanov \[2022\]](#),  
296 while experimental harpoon tests in the RemoveDebris mission saw a carbon-fibre deploy-  
297 able boom snap on contact with the capture target at 20 m/s [Aglietti et al. \[2020\]](#). Wang  
298 et al. (2023) note explicitly that rigid manipulation “has the potential to generate fragments  
299 during the capturing phase” [Wang et al. \[2023\]](#), and Chen et al. (2024) characterise single  
300 contact-based caging approaches as “excessively risky for fast-tumbling targets” [Chen et al.](#)  
301 [\[2024a\]](#).

302 This fragmentation paradox is quantifiable in energetic terms. The NASA/ESA IMPACT  
303 model identifies a catastrophic fragmentation threshold of 10 J/g of specific energy at the con-  
304 tact interface [Liou and Johnson \[2006\]](#). A 100-kg debris object rotating at  $\omega = 5$  deg/s and  
305 grasped rigidly at a moment arm of 0.5 m experiences a contact energy of order  $\frac{1}{2}I\omega^2 \approx$  sev-  
306 eral hundred joules at the grasp point. If this energy is absorbed by the contact structure  
307 rather than dissipated, the resulting specific energy may approach or exceed the fragmen-  
308 tation threshold for lightweight aluminium honeycomb solar panel structures. No published  
309 paper has conducted a systematic quantitative comparison of fragment generation probabilit-  
310 ity between rigid and compliant capture mechanisms — this gap is identified as a priority  
311 experimental question in Section 13.

312 Compliant and soft capture systems address the paradox by absorbing and redistributing  
313 contact energy rather than transmitting impulsive forces. Eight distinct soft and compliant  
314 capture approaches are reviewed in Section 3, ranging from gecko-inspired dry adhesives  
315 (microgravity-validated at TRL 4–5 [Jiang et al. \[2017\]](#)) to DEMES grippers with mission  
316 heritage on CleanSpace One [Araromi et al. \[2015\]](#) and inflatable robotic arms [Palmieri et al.](#)  
317 [\[2023\]](#). None has yet demonstrated in-flight capture, establishing a clear technology gap that  
318 motivates the investment in flight demonstration infrastructure discussed in Section 13.

## 319 Operational Consequences

320 The operational burden of the debris environment is no longer theoretical. At 550 km altitude  
321 — the operating shell of many Starlink satellites — the trackable debris density is sufficient  
322 to require avoidance manoeuvres at a rate that consumes propellant reserves and interrupts

323 normal operations. Starlink’s 144,404 avoidance manoeuvres in H1 2025 (65-fold increase  
 324 from 2021 [ESA Space Debris Office \[2025\]](#)) represent a structural operational cost that scales  
 325 with constellation size. ESA’s own operational satellites execute hundreds of manoeuvres  
 326 annually, with collision avoidance emerging as a primary mission-operations driver. The  
 327 economic externality — uncontrolled debris imposes avoidance costs on all operators —  
 328 provides a market-failure argument for policy-mandated ADR that is increasingly reflected  
 329 in international guidelines [Liou et al. \[2010\]](#).

## 330 2.2 Human Exploration Beyond LEO: The Habitat Challenge

331 The second driver for soft inflatable systems is the ambition for sustained human presence  
 332 beyond the ISS. NASA’s Artemis programme, ESA’s Moon Village concept, and private  
 333 ventures such as Orbital Reef collectively assume that humans will occupy permanent or  
 334 semi-permanent outposts in cislunar space, on the lunar surface, in Mars transit, and even-  
 335 tually on the Martian surface. All of these scenarios require pressurised habitable volumes  
 336 substantially larger than any single rigid module that can be launched within existing fairing  
 337 constraints.

### 338 The Mass and Volume Efficiency Argument

339 Valle et al. (2019) provide the definitive comparative analysis of inflatable versus metallic  
 340 pressurised structures [Valle et al. \[2019a\]](#). The key metric is areal density (mass per unit  
 341 floor area, or equivalently, mass per unit pressurised volume):

Table 3: Mass efficiency comparison of representative pressurised space modules (adapted from Valle et al. 2019 [Valle et al. \[2019a\]](#)).

Module	Type	Press. Vol. (m <sup>3</sup> )	Mass (kg)	Density (kg/m <sup>3</sup> )
TransHab concept	Inflatable	339	13,200	39
BEAM (as-built)	Inflatable	16	1,415	88
Columbus (ESA)	Metallic	75	10,300	137
Tranquility (Node 3)	Metallic	74	15,200	205

342 The mass efficiency advantage derives directly from material specific strength. Vectran  
 343 HT, the primary restraint-layer fabric in BEAM and TransHab, has a tensile strength of  
 344 3.0 GPa at a density of 1.40 g/cm<sup>3</sup>, yielding a specific strength of 2,330 kN-m/kg [Valle  
 345 et al. \[2019a\]](#). Kevlar 49, similarly used for restraint and micrometeoroid and orbital debris  
 346 (MMOD) protection, achieves approximately 2,080 kN-m/kg at the fabric level (3.0 GPa  
 347 UTS, 1.44 g/cm<sup>3</sup> density) or 2,500 kN-m/kg at the filament level (3.6 GPa UTS) [DuPont  
 348 \[2019\]](#). These compare to Ti-6Al-4V at 220 kN-m/kg and aluminium 7075-T6 at 204 kN-  
 349 m/kg: the fabric advantage is approximately one order of magnitude. This difference directly  
 350 determines what pressurised volume can be delivered per kilogram of launch mass, and  
 351 therefore what human presence scenarios are economically feasible.

352 The volumetric launch efficiency is equally compelling. A 300 m<sup>3</sup> pressurised module at  
 353 metallic density would mass approximately 40,000 kg — exceeding the cargo capacity of any

354 current or planned launch vehicle for a single module. The Sierra Space LIFE 285 habitat,  
355 targeting approximately 300 m<sup>3</sup> of pressurised volume, folds into a fairing-compatible package  
356 and deploys on orbit, representing a volume achievable in a single launch that has no metallic-  
357 module equivalent [Sierra Space Corporation \[2024\]](#).

### 358 **BEAM as Technology Proof**

359 The BEAM module, delivered to the ISS by SpaceX CRS-8 in April 2016 and expanded  
360 in May 2016, constitutes the highest-TRL demonstration of crewed inflatable space struc-  
361 tures [NASA Johnson Space Center \[2017\]](#). BEAM provides 16 m<sup>3</sup> of pressurised volume at  
362 a deployed mass of 1,415 kg and has maintained pressure integrity for more than eight years  
363 without rigidisation. Operational experience includes periodic crew access for inspection and  
364 equipment storage, structural health monitoring via embedded accelerometers and impact  
365 detection systems, and characterisation of the thermal, radiation, and MMOD environment.

366 BEAM’s deployment was not without difficulty: initial expansion attempts on 28 May  
367 2016 required 25 pressurisation bursts over approximately seven hours to overcome friction  
368 between compressed softgoods layers, compared to the planned single-burst expansion. This  
369 experience provided critical engineering data on fold-compression set and deployment reli-  
370 ability that directly informs the design of future autonomous deployment systems. Kennedy  
371 (2002) documents the TransHab programme’s prior exploration of this challenge, including  
372 burst pressure tests to 4× operating pressure and the critical importance of restraint-layer  
373 preloading for deployment force prediction [Kennedy \[2002\]](#).

### 374 **Radiation: The Honest Assessment**

375 BEAM data from the September 2017 solar particle event (SPE) revealed a critical finding  
376 that must be stated clearly [NASA Johnson Space Center \[2017\]](#). Absorbed dose measure-  
377 ments in BEAM during the SPE were approximately 2–2.5 mGy, compared to approximately  
378 0.25 mGy measured simultaneously in adjacent metallic ISS habitable volumes — an 8–10×  
379 ratio. This finding demonstrates that fabric walls alone provide substantially less radiation  
380 shielding than the aluminium walls of conventional modules.

381 This is not a disqualifying result, but it is a design constraint. The TransHab architecture  
382 addressed this through a water-wall concept: a ~10 cm thick water reservoir integrated into  
383 the inner wall layers that provides both radiation shielding (hydrogen-rich material) and  
384 useful crew water storage. Norbury et al. (2025) review passive shielding materials for  
385 space and confirm that polyethylene achieves a 27.8% mass saving relative to aluminium  
386 for equivalent proton shielding at the same areal density [Norbury et al. \[2025\]](#). The design  
387 solution is established; its implementation requires deliberate integration rather than passive  
388 reliance on wall thickness.

## 389 **2.3 Unifying Thesis: Shared Fabric Technology Across Applications**

390 The central organising principle of this survey is that the high-strength fabric technology  
391 enabling inflatable habitats is the same technology enabling compliant ADR capture arms,

392 large deployable debris shields, and the soft robotic systems operating within and around  
 393 both. This material unity has engineering consequences that extend beyond mere analogy.

### 394 **Material Traceability Across Applications**

395 Table 4 maps the four primary fabric families across their roles in different application do-  
 396 mains. The key observation is that the same material qualification data — creep behaviour,  
 397 AO erosion yield, UV degradation rate, thermal cycling tolerance — is relevant across all  
 398 applications. A Vectran creep characterisation campaign conducted for habitat restraint-  
 399 layer lifetime prediction [Weadon \[2013\]](#) is directly applicable to Vectran inflatable robotic  
 400 arm links [Palmieri et al. \[2023\]](#). A Nextel/Kevlar debris shield hypervelocity test cam-  
 401 paign [Destefanis et al. \[2003\]](#) produces data applicable to both habitat MMOD protection  
 402 and inflatable debris shield design [Cha et al. \[2024\]](#).

Table 4: Shared fabric technology across application domains. The same material families serve multiple functions, sharing qualification heritage and manufacturing processes.

Material	Habitat role	ADR role	Robotic arm role
Vectran HT	Restraint layer (primary load)	Inflatable arm links	Inflatable manipulator links
Kevlar 49	MMOD rear wall; restraint co-layer	Net shield backing	Arm outer jacket
Nextel 440	MMOD bumper (ceramic)	Debris bumper layer	–
Kapton/Mylar	MLI outer layers; bladder liner	Shield thermal layer	Bladder inner liner
Beta cloth	AO-resistant outer cover	–	AO-resistant cover

### 403 **The Mars Airbag Precedent**

404 Vectran’s role in the Mars Pathfinder (1997), Mars Exploration Rover (2004), and subse-  
 405 quent airbag systems provides heritage that extends beyond Earth orbit. These missions  
 406 demonstrated that Vectran-based inflatable structures can survive the combined stresses of  
 407 launch vibration, interplanetary cruise, hypervelocity atmospheric entry, and impact landing  
 408 on an extraterrestrial surface [Litteken \[2019\]](#). The qualification data base thus spans not  
 409 merely LEO but the full range of conditions relevant to deep space exploration — a heritage  
 410 directly relevant to future Mars transit habitat designs.

### 411 **Origami Geometry Unifies Packaging and Protection**

412 A particularly striking example of cross-domain material unification is the Inflatable Modular  
 413 Space Shield (IMSS) proposed by Cha et al. (2024) [Cha et al. \[2024\]](#). The IMSS uses a wa-

414 terbomb origami tessellation to fold a multi-layer ultra-high-molecular-weight polyethylene  
415 (UHMWPE)/Kevlar/Nextel shield into a package achieving 90% volume reduction relative  
416 to a rigid Whipple shield of equivalent protection. The same Miura-ori and waterbomb  
417 fold patterns [Miura \[1985\]](#) used in IMSS for debris shield deployment are the canonical fold  
418 patterns for large membrane space structures generally [Schenk et al. \[2014\]](#) — packaging  
419 efficiency and multi-shock protection are simultaneously optimised by the same tessellation  
420 geometry.

## 421 **Scale-Dependent Challenges**

422 While the material foundation is shared, the engineering challenges depend strongly on scale.  
423 The scale-dependent challenge landscape can be summarised as follows: at centimetre scale  
424 (soft gripper fingers), actuation force and contact compliance dominate the design; at metre  
425 scale (inflatable arms, BEAM-class habitats), deployment mechanics and pressure-retention  
426 integrity dominate; at 10-metre scale (large solar concentrators, small debris shields), control-  
427 structure interaction begins to matter; at 100-metre scale (large debris shields, solar power  
428 collectors), attitude and orbit control, aerodynamic drag compensation, power generation,  
429 and thermal management become the primary engineering challenges, for which no flight  
430 heritage exists.

431 This survey is organised to trace the technology from its best-proven applications (TRL 9  
432 materials, TRL 9 BEAM habitat, TRL 8–9 rigid solar arrays) through to the most speculative  
433 future capabilities (TRL 2–3 pressure-stabilised membrane AOCS, TRL 3–4 vacuum-gap  
434 actuation), making explicit at each stage what is demonstrated, what is extrapolated, and  
435 what requires new research.

## 436 **Why Soft? Why Inflatable? Why Now?**

437 Three converging developments make this survey timely.

438 *Material advances.* Vectran and Kevlar have matured to TRL 9 in space environments.  
439 Perovskite/CIGS tandem solar cells, demonstrated at 2,100 W/kg with 85% proton radia-  
440 tion retention after equivalent 50-year LEO exposure [Lang et al. \[2020\]](#), promise to integrate  
441 power generation into inflatable membrane layers at specific powers unachievable with con-  
442 ventional rigid panels. Cryogenic metallic cable-based soft robots ([Foster-Hall et al. 2025](#))  
443 maintain full range of motion at  $-196\text{ }^{\circ}\text{C}$ , solving the elastomer embrittlement problem for  
444 deep-space applications [Foster-Hall et al. \[2025\]](#).

445 *Mission context.* The commercial station era (Orbital Reef, Axiom, LIFE, Starlab) cre-  
446 ates the first sustained market demand for habitable volume beyond ISS. ESA’s ClearSpace-1  
447 mission, targeting PROBA-1 for retrieval in the late 2020s, establishes ADR as an opera-  
448 tional rather than experimental activity. The convergence of launch cost reduction (SpaceX  
449 Falcon 9, Starship) with mission demand means that the technology development cost of  
450 inflatable systems is now justifiable against a credible mission pull.

451 *Paradigm shift.* As outlined in Section 1, the space environment is increasingly un-  
452 derstood as a *resource* for soft robotic systems rather than an obstacle. Vacuum-gap ac-  
453 tuation [Sirbu et al. \[2025\]](#), jamming without pumps [Fitzgerald et al. \[2020\]](#), and passive  
454 microgravity compliance [Araromi et al. \[2015\]](#) represent a qualitative shift in what the space

455 environment enables. This survey maps these opportunities systematically across the full  
456 technology stack.

457 The following sections develop the application use cases (Sections 3 and 4) before re-  
458 viewing the enabling technology state-of-the-art (Sections 5–12), and concluding with a  
459 consolidated gap analysis and research roadmap (Section 13).

## 460 3 Use Cases: Active Debris Removal

461 The orbital debris environment—characterised in Section 2.1—represents the most urgent  
462 operational motivation for soft inflatable robotic systems in space. With over 54,000 esti-  
463 mated objects larger than 10 cm, 15,800 tonnes of total orbital mass, and a 65-fold increase  
464 in Starlink collision avoidance manoeuvres since 2021 [ESA Space Debris Office \[2025\]](#), the  
465 operational urgency is undeniable.

466 The scientific foundation for active debris removal (ADR) was established by Kessler and  
467 Cour-Palais [Kessler and Cour-Palais \[1978\]](#), who developed the first mathematical model pre-  
468 dicting cascading collisional fragmentation in low Earth orbit (LEO). Their analysis identified  
469 three debris population regimes—stable, critical, and cascading—and predicted the forma-  
470 tion of a debris belt within a century. Subsequent Monte Carlo simulations by Liou and  
471 Johnson [Liou and Johnson \[2006, 2008\]](#) using the NASA LEGEND model with 200-year pro-  
472 jections across 50 runs demonstrated that the LEO debris population had already crossed  
473 the instability threshold: the number of objects would continue to grow even with zero future  
474 launches. Their work quantified the minimum intervention rate, establishing that at least  
475 five large objects per year must be removed from the 800–1000 km altitude bands to stabilise  
476 the environment [Liou et al. \[2010\]](#). At approximately 550 km altitude, debris spatial density  
477 now equals active satellite density—an unprecedented situation that fundamentally changes  
478 the risk calculus for orbital operations [ESA Space Debris Office \[2025\]](#).

479 This section examines the role of soft and inflatable systems in addressing the debris  
480 challenge. We first review conventional rigid capture approaches and their inherent fragmen-  
481 tation risk (Section 3.1), then survey eight distinct soft and compliant capture mechanisms  
482 (Section 3.2), and finally discuss inflatable debris shields as passive protection infrastructure  
483 (Section 3.3).

### 484 3.1 Rigid Capture Approaches and Fragmentation Risk

485 Active debris removal using rigid robotic manipulators has been the dominant paradigm in  
486 mission planning for the past two decades. Zhao et al. [Zhao et al. \[2024\]](#) provide the most  
487 recent comprehensive review in *Progress in Aerospace Sciences* of rigid manipulators for on-  
488 orbit servicing and ADR, covering flight-heritage systems such as the Canadarm and the  
489 European Robotic Arm (ERA), cancelled missions including ESA’s e.deorbit, and planned  
490 missions such as ClearSpace-1. The review documents the extensive engineering heritage of  
491 rigid robotic arms but also explicitly acknowledges the potential for fragmentation generation  
492 during debris capture [Zhao et al. \[2024\]](#).

493 Ledkov and Aslanov [Ledkov and Aslanov \[2022\]](#) survey the full spectrum of ADR meth-  
494 ods in *Progress in Aerospace Sciences*, including nets, harpoons, robotic arms, tentacles, ion

495 beam shepherding, laser ablation, electrostatic tractors, and electrodynamic tethers. Their  
496 analysis notes that contactless methods such as ion beam shepherding—capable of deorbit-  
497 ing a 2-tonne debris object in 3–4 months—carry zero mechanical impact risk, but require  
498 extended proximity operations and significant power budgets. Contact-based methods, while  
499 operationally faster, necessarily introduce mechanical loads to the target.

500 The only in-orbit ADR technology demonstration to date is the RemoveDebris mission,  
501 documented by Aglietti et al. [Aglietti et al. \[2020\]](#). This mission successfully demonstrated  
502 net capture of a CubeSat at 5 cm/s relative velocity and 7 m separation distance, as well  
503 as harpoon firing at 20 m/s into a target panel at 1.5 m range. Two results are particu-  
504 larly instructive. First, the net capture succeeded but was conducted against a cooperative  
505 2U CubeSat (expanded to approximately 1 m pyramidal target), which is not representative  
506 of real debris targets of 500 kg–8 tonnes tumbling at 1–5 deg/s. Second, and more critically,  
507 the harpoon test resulted in the *snapping of the carbon fibre boom* from impact forces, de-  
508 spite the harpoon itself being retained by its tether [Aglietti et al. \[2020\]](#). This structural  
509 failure during a controlled test illustrates the magnitude of impulse loads that contact-based  
510 capture imposes.

### 511 3.1.1 The Fragmentation Paradox

512 The central paradox of rigid-body ADR is that the very act of removing debris may generate  
513 new fragments, potentially worsening the environment it aims to protect. This concern is  
514 supported by multiple lines of evidence:

- 515 • Wang et al. [Zhang et al. \[2022\]](#) state explicitly that “rigid behaviour has the potential  
516 to generate fragments during [the] capturing phase, hence increase [the] risk of further  
517 space debris.”
- 518 • Chen et al. [Chen et al. \[2024a\]](#) assess that “single contact-based caging [is] excessively  
519 risky for fast-tumbling targets with unknown mass—momentum transfer could create  
520 new debris.”
- 521 • Dynamic simulations of the cancelled e.deorbit mission show peak torques of 195 Nm  
522 at the manipulator joints when attempting to capture a target tumbling at only 5 deg/s  
523 (the ENVISAT upper stage) [Stolfi et al. \[2017\]](#), reaching the operational limits of the  
524 robotic joints.
- 525 • The Aerospace Corporation’s IMPACT model establishes 10 J/g specific energy as the  
526 threshold for catastrophic fragmentation of a satellite [Aerospace Corporation \[2020\]](#).

527 ClearSpace-1, the first contracted commercial debris removal mission (ESA, €86M con-  
528 tract), plans to use four rigid robotic arms to capture the Proba-1 satellite (95 kg,  $0.6 \times 0.6 \times$   
529  $0.8$  m) [ClearSpace SA and European Space Agency \[2020\]](#). The mission’s planning was itself  
530 disrupted by the debris problem: the original target, the VESPA upper stage, was struck by  
531 a tracked debris object during mission preparation, illustrating the cascading urgency of the  
532 debris environment [ClearSpace SA and European Space Agency \[2020\]](#). Launch is currently  
533 planned for approximately 2029.

534 To place the fragmentation risk in perspective, we note that a rigid robotic arm exerting  
535 195 Nm of torque on a 100 kg target at a 0.5 m lever arm produces a contact force of 390 N.  
536 If this force acts over a contact area of 10 cm<sup>2</sup> on a honeycomb panel with typical crush  
537 strength of 1–3 MPa, the resulting stress of 0.39 MPa falls below the crush threshold of  
538 the primary structure. However, the fragmentation risk is not primarily to the strongest  
539 structural components, but to the most vulnerable: degraded solar panel hinge joints, aged  
540 thermal blanket fasteners, corroded aluminium alloy brackets, and antenna feed structures  
541 that have experienced decades of thermal cycling, UV degradation, and atomic oxygen ero-  
542 sion. These appendage materials may have lost 30–60% of their original strength through  
543 environmental degradation, reducing effective crush thresholds well below nominal values.

544 For a tumbling 1000 kg upper stage at 5 deg/s, the angular momentum is approximately  
545 50 N·m·s, and the impulsive loads during despin are proportionally larger. Applying the  
546 catastrophic fragmentation threshold of 10 J/g from the IMPACT model [Aerospace Corpo-](#)  
547 [ration \[2020\]](#), [Johnson et al. \[2001\]](#): if a rigid grasp concentrates 50 J of despin energy into a  
548 100 g solar panel hinge assembly, the resulting specific energy of 0.5 J/g remains below the  
549 10 J/g threshold, but contact with a 10 g degraded thermal blanket fastener at equivalent  
550 energy would yield 5 J/g—approaching the threshold. A compliant grasp distributing the  
551 same energy over a larger contact area and longer time period reduces peak specific energy  
552 by one to two orders of magnitude.

553 The fragmentation risk is therefore physically plausible and supported by qualitative as-  
554 sessments, though not yet experimentally quantified. This survey adopts the precautionary  
555 principle: compliant capture is preferred until quantitative data become available, on the  
556 basis that the consequences of inadvertent fragmentation during ADR—potentially generat-  
557 ing hundreds of new tracked objects—are severe enough to warrant risk-averse technology  
558 selection even in the absence of definitive comparative data. A comprehensive, quantita-  
559 tive comparison of fragmentation probability as a function of contact compliance remains  
560 the single highest-priority open experimental question the community must address (see  
561 Section 13).

562 Table 5 summarises the principal ADR technology classes, their technology readiness  
563 levels (TRL), contact characteristics, and assessed fragmentation risk.

## 564 3.2 Soft and Compliant Capture Mechanisms

565 The fragmentation risk inherent in rigid capture has motivated the development of soft and  
566 compliant alternatives that absorb, rather than transmit, kinetic energy during the capture  
567 interaction. Eight distinct soft and compliant capture approaches have been documented in  
568 the literature, all currently at TRL 2–5. We review each in turn, organised by their operating  
569 principle: adhesion-based, bistable/passive, inflatable-arm, and net-plus-inflatable systems.

### 570 3.2.1 Gecko-Inspired Dry Adhesive Grippers

571 The most mature soft capture technology is the gecko-inspired dry adhesive gripper demon-  
572 strated by Jiang et al. [Jiang et al. \[2017\]](#). Published in *Science Robotics*, this system uses  
573 shear-activated van der Waals adhesion pads with a load-sharing tendon-pulley mechanism  
574 that scales adhesion from small patches to large contact areas. Critically, a nonlinear pas-

Table 5: Comparison of active debris removal technology classes. Fragmentation risk is assessed qualitatively based on published evidence; a quantitative comparison remains an open research gap.

<b>Method</b>	<b>TRL</b>	<b>Contact</b>	<b>Frag. Risk</b>	<b>Key Limitation</b>
Rigid robotic arm	5–6	Direct, rigid	High	Peak torques at joint limits; brittle appendage damage
Harpoon	6	Penetrative	Very high	Boom failure in RemoveDebris; target perforation
Thrown net	7	Enveloping	Moderate	Impulse at net closure; entanglement dynamics
Ion beam shepherd	4	Contactless	None	3–4 month timeline; high power
Laser ablation	3	Contactless	None	Pointing accuracy; space weapon concerns
Gecko adhesive	4–5	Shear adhesion	Very low	Clean surfaces assumed; no tumbling test
Soft/inflatable arm	2–3	Compliant	Low	Precision; pneumatic in vacuum
Bistable gripper	2–3	Passive snap	Low	Energy barrier tuning; untested in vacuum
Net + inflatable (INSIDeR)	~4	Controlled net	Low	System integration unproven in orbit

575 sive wrist provides high stiffness during normal manipulation but becomes compliant under  
576 overload, offering inherent protection against excessive contact forces.

577 The gecko gripper was validated in actual microgravity during NASA parabolic flight  
578 campaigns, achieving capture success rates of 100% for spherical targets, 75% for cubic tar-  
579 gets, and 81% for cylindrical targets, with objects up to approximately 400 kg and diameters  
580 exceeding 1 m [Jiang et al. \[2017\]](#). Failures were attributed to human operator misalignment  
581 rather than adhesive performance. The system achieves essentially zero mechanical impact  
582 force—a fundamental advantage for fragmentation avoidance. We note, following the taxon-  
583 omy of [Shintake et al. \[2018\]](#), that the gecko gripper is more precisely classified  
584 as a compliant end-effector mechanism on a rigid platform rather than a fully soft robotic  
585 system; nevertheless, its compliant capture interface directly addresses the fragmentation  
586 concern. At TRL 4–5, it represents the highest-readiness soft capture technology, though  
587 significant gaps remain: all testing used cooperative (stationary) targets, and performance  
588 under space vacuum, UV radiation, atomic oxygen exposure, and thermal cycling has not  
589 been demonstrated.

### 590 3.2.2 Dielectric Elastomer Minimum Energy Structure (DEMES) Grippers

591 [Araromi et al. \[2015\]](#) developed a DEMES-based deployable gripper explic-  
592 itly for the CleanSpace One ADR mission. The device uses dielectric elastomer actuators  
593 (DEAs) bonded to a flexible frame, achieving rollable compact storage and deployment to  
594 a multi-segment gripper with bending angles exceeding 60°. Each arm produces forces in  
595 the mN range, sufficient only for microgravity manipulation of small, lightweight targets.  
596 The system demonstrated over 860,000 actuation cycles with individual arm mass below  
597 0.65 g [Araromi et al. \[2015\]](#). At TRL 3–4, the DEMES gripper is notable as the only soft  
598 capture device explicitly designed for an actual ADR mission, although the CleanSpace One  
599 mission architecture subsequently evolved without the gripper flying. Key limitations in-  
600 clude the high operating voltage ( $\sim$ kV) required for DEAs in vacuum (arcing risk) and the  
601 absence of cryogenic or thermal cycling testing.

### 602 3.2.3 Bistable and Passive Capture Grippers

603 Two distinct bistable gripper concepts have been proposed for ADR. [Liu et al. \[2022\]](#)  
604 developed a bistable snap-through gripper that captures targets using the kinetic  
605 energy of the collision itself, requiring no external power for the grasping action. The gripper  
606 deforms on contact, absorbs kinetic energy, triggers a bistable snap, and locks into the closed  
607 configuration. The energy barrier is adjustable through pre-deformation of the bistable  
608 elements, allowing tuning for different target masses and approach velocities [Liu et al. \[2022\]](#).  
609 This passive capture concept eliminates the need for precise actuation timing—a significant  
610 advantage for tumbling, non-cooperative targets.

611 [Zhang et al. \[2023b\]](#) propose a Venus flytrap-inspired bistable origami gripper  
612 actuated by a shape memory alloy spring actuator (SMASA) that provides slow energy  
613 storage followed by rapid release, with a DEA bristle-locking structure that prevents target  
614 escape after capture. Capture is achieved within approximately 300 ms, and the device has  
615 been demonstrated on complex geometries including asteroid models and spacecraft mock-

ups [Zhang et al. \[2023b\]](#). Both bistable concepts remain at TRL 2–3, with no vacuum, thermal, or microgravity testing.

### 3.2.4 Thermally Qualified Soft Grippers

Addressing the thermal environment is critical for any space capture mechanism. Ruiz Vincueria et al. [Ruiz Vincueria et al. \[2023\]](#) developed a multi-layered soft gripper combining TPU, silicone, PTFE, and aerogel layers, tested across the full orbital thermal range from  $-180^{\circ}\text{C}$  to  $+220^{\circ}\text{C}$ . A counter-intuitive but operationally significant finding is that grasping forces *increase* by 220% at cryogenic temperatures due to cold stiffening of the elastomeric layers, while decreasing by at most 50% at the hot extreme [Ruiz Vincueria et al. \[2023\]](#). The gripper uses  $\text{MoS}_2$  solid lubricant for vacuum compatibility and is available in dual and quad arm configurations. This work provides the most quantitative thermal performance data for any soft capture device and explicitly compares its approach against the ClearSpace-1 and Astroscale rigid arm architectures. However, all testing was conducted in laboratory conditions without vacuum, radiation, or microgravity validation (TRL 2).

Foster-Hall et al. [Foster-Hall et al. \[2025\]](#) introduce a fundamentally different approach to the cryogenic challenge: metallic cable-driven soft robotic structures tested at  $-196^{\circ}\text{C}$  in liquid nitrogen. Unlike elastomeric soft robots that embrittle at cryogenic temperatures, the modular metallic cable structures exhibited only 5% stiffness increase over 100 actuation cycles, maintained full range of motion, and showed no microfractures under scanning electron microscopy—consistent with cold-working behaviour in stainless steel rather than brittle failure [Foster-Hall et al. \[2025\]](#). Two-dimensional grasping was demonstrated at  $-196^{\circ}\text{C}$ . At TRL 2–3, this work opens a new design paradigm for soft space robotics beyond elastomers, though three-dimensional manipulation and vacuum testing remain to be demonstrated.

### 3.2.5 Inflatable Robotic Arms for Capture

Palmieri et al. [Palmieri et al. \[2023\]](#) developed the POPUP robot: a 7-DOF manipulator with inflatable links and rigid electric motor joints, incorporating visual servoing via dual cameras and high-stiffness fibre reinforcement. The inflatable links provide significant mass and volume reduction compared to equivalent rigid arms, and simulation demonstrates debris capture feasibility despite the inherent compliance of the links [Palmieri et al. \[2023\]](#). A 3-DOF ground prototype has been statically characterised (TRL 3), but key challenges remain: the compliance of inflatable links reduces end-effector positioning precision, the pneumatic inflation system must operate in vacuum, and no thermal or radiation testing has been performed.

### 3.2.6 INSIDeR: Net Capture with Inflatable Deployment

The Innovative Net and Space Inflatable structure for active Debris Removal (INSIDeR) is a patented CNES/ESA-funded concept that combines the proven in-orbit heritage of net capture (demonstrated by RemoveDebris) with inflatable deployment structures [CT Ingénierie et al. \[2017, 2021\]](#). The system architecture comprises an inflatable ring and two inflatable masts that deploy and guide a capture net, followed by a deorbit tether for removal. The complete capture sequence proceeds through six phases: inflation of the ring

656 and masts, net deployment, approach boost, mast detachment and deflation, net capture,  
 657 and tether-assisted deorbit [CT Ingénierie et al. \[2017\]](#).

658 A key innovation is that the inflatable masts provide controlled, slow net dynamics,  
 659 eliminating the large impulse peaks associated with conventional spring-ejected nets and  
 660 thereby reducing momentum transfer to the target [CT Ingénierie et al. \[2021\]](#). The system  
 661 packages into a cube of approximately 50 cm per side, forming a plug-and-play ADR kit  
 662 adaptable to any target mass, morphology, or tumbling rate. Developed over 15 years by  
 663 CT Ingénierie and AirCaptif (Michelin group) with CNES and ESA co-funding, INSIDeR has  
 664 reached TRL  $\sim 4$  at the system level (individual subsystem technologies at TRL 5+), with  
 665 a ground demonstrator under construction as of 2021 [CT Ingénierie et al. \[2021\]](#). ABAQUS  
 666 finite element simulations have confirmed net capture feasibility.

667 Table 6 provides a comprehensive comparison of all documented soft and compliant cap-  
 668 ture approaches.

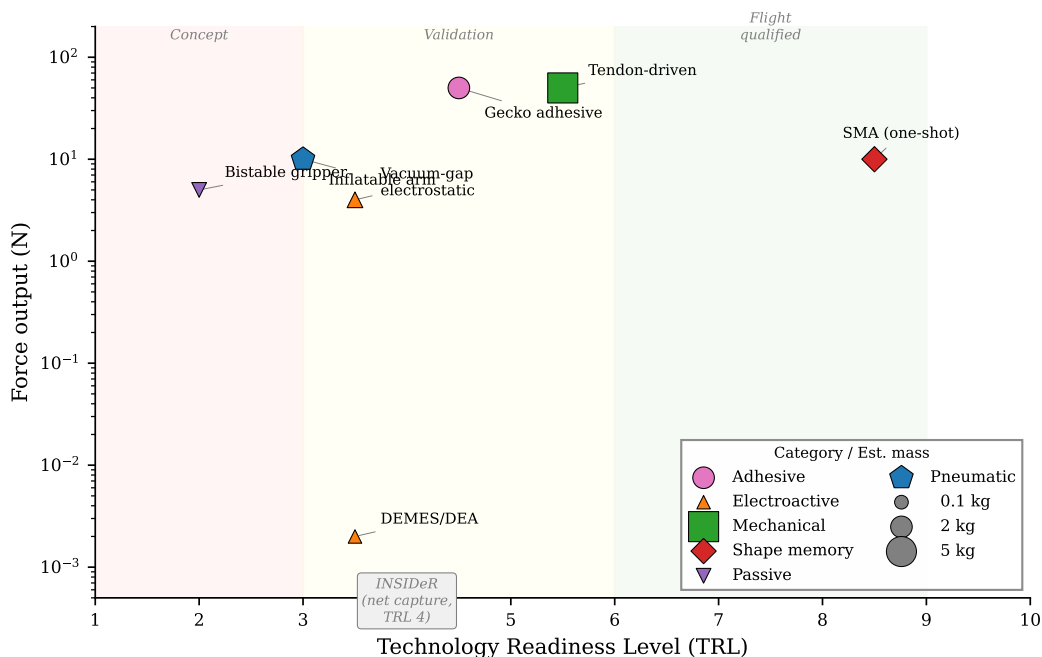


Figure 2: Force output versus technology readiness level (TRL) for soft and compliant capture approaches. Marker size indicates system mass. The gecko adhesive gripper occupies the highest-TRL, highest-force quadrant, representing the most flight-ready soft capture technology.

669 The most significant observation from this landscape is the absence of orbital flight  
 670 heritage for any soft capture system. The gecko adhesive gripper, at TRL 4 with microgravity  
 671 validation, and INSIDeR, at TRL 4 with system-level ground demonstration, represent the  
 672 nearest-term candidates for flight demonstration. We identify the combination of a gecko  
 673 adhesive gripper mounted on an inflatable arm with fibre Bragg grating structural health  
 674 monitoring (see Section 8.1) as the most flight-ready near-term soft ADR demonstrator—a  
 675 system that leverages the highest-TRL end-effector, the mass efficiency of inflatable links,  
 676 and embedded sensing for operational awareness.

Table 6: Technology readiness and performance comparison of soft and compliant capture mechanisms for active debris removal. No soft capture system has flown an orbital capture mission to date.

Approach	Key Reference	TRL	Force Output	$\mu g$ Test	Key Limitation
Gecko adhesive	Jiang 2017 <a href="#">Jiang et al. [2017]</a>	4 <sup>a</sup>	$\leq 400$ kg objects	Yes	Clean surfaces; no tumbling
DEMES/DEA	Araromi 2015 <a href="#">Araromi et al. [2015]</a>	3 <sup>b</sup>	mN range	No	Very low force; HV arcing
Inflatable arm	Palmieri 2023 <a href="#">Palmieri et al. [2023]</a>	3	Not quantified	No	Low precision; pneumatic in vacuum
Flytrap origami	Zhang 2023 <a href="#">Zhang et al. [2023b]</a>	2–3	Bistable snap	No	SMA slow reset; HV in vacuum
Bistable gripper	Liu 2023 <a href="#">Liu et al. [2022]</a>	2	Passive (KE input)	No	Energy barrier tuning
Cryo metallic	Foster-Hall 2025 <a href="#">Foster-Hall et al. [2025]</a>	2–3	Not quantified	No	2D only; no vacuum
Thermal multi-layer	Ruiz 2024 <a href="#">Ruiz Vincueria et al. [2023]</a>	2	+220% at cryo	No	Lab only; no vacuum
INSIDeR (net+infl.)	ESA SDC 2017/21 <a href="#">CT Ingénierie et al. [2017, 2021]</a>	4	N/A (net)	Sim. only	System integration

<sup>a</sup>TRL 4 per NASA NPR 7123.1B: parabolic flight ( $\sim 20$  s  $\mu g$  per parabola) constitutes component validation in a simulated relevant environment rather than a fully relevant orbital environment (TRL 5).

<sup>b</sup>TRL 3: 860,000 cycles demonstrated in ambient conditions, but no space environment testing (vacuum, thermal cycling, radiation) performed.

### 677 3.3 Inflatable Debris Shields

678 Beyond active capture, inflatable structures offer a complementary approach to the debris  
679 problem through passive shielding. Conventional rigid Whipple shields [Arnold et al. \[2009\]](#),  
680 which use spaced aluminium bumper plates to disrupt and disperse hypervelocity projectiles  
681 before they reach the pressure wall, are effective but carry significant mass and volume  
682 penalties. The substitution of rigid bumper plates with flexible fabric layers—using the  
683 same high-strength materials (Nextel ceramic fabric, Kevlar, and ultra-high molecular weight  
684 polyethylene, UHMWPE) that form the basis of inflatable habitat walls—enables deployable  
685 shields with dramatically improved packaging efficiency.

686 Destefanis et al. [Destefanis et al. \[2006\]](#) demonstrated that stuffed Whipple shields using  
687 Nextel and Kevlar layers protect against projectiles twice the diameter of those stopped by  
688 standard aluminium Whipple shields at equal areal density. This finding established the  
689 performance advantage of fabric-based shielding architectures that underlies both habitat  
690 micrometeoroid and orbital debris (MMOD) protection and standalone shield concepts.

691 Cha et al. [Cha et al. \[2024\]](#) present the Inflatable Multi-Shock Shield (IMSS), which ap-  
692 plies waterbomb tessellation origami to create a deployable multi-bumper debris shield that  
693 expands approximately 80% beyond its initial radius while achieving 90% volume savings  
694 compared to an equivalent rigid Whipple shield. The IMSS uses UHMWPE fibre for ballistic  
695 protection within a five-bumper configuration, with 50 mm bumper spacing accommodated  
696 in a 400 mm stowed stack [Cha et al. \[2024\]](#). A critical design feature is that all material  
697 in the deployed configuration contributes to debris protection—there is no structural dead  
698 weight. The origami fold geometry that enables compact packaging simultaneously creates  
699 the inter-bumper spacing required for effective hypervelocity projectile disruption, embody-  
700 ing a dual-functionality design principle applicable to large deployable structures generally  
701 (see Section 4.3 for related deployment mechanics).

702 At TRL 2–3, the IMSS concept requires further development in hypervelocity impact  
703 validation, large-scale (>10 m) deployment demonstration, and inflation system design.  
704 Nevertheless, the material commonality between inflatable debris shields, inflatable habi-  
705 tat MMOD layers, and inflatable robotic arm structural fabrics reinforces the survey’s  
706 central thesis: the same high-strength fabric technology base—Vectran, Kevlar, Nextel,  
707 UHMWPE—enables debris capture, debris protection, and habitable volume creation.

708 For very large-scale applications, inflatable debris shields of 100 m class have been pro-  
709 posed as orbital infrastructure to protect high-value assets or clear debris corridors. Such  
710 structures would require the attitude and orbit control technologies discussed in Section 11  
711 and the robotic in-orbit assembly capabilities reviewed in Section 12, linking the passive  
712 protection concept back to the active robotic systems that are the primary focus of this  
713 survey.

## 714 4 Use Cases: Habitats and Exploration

715 Inflatable space structures for human habitation represent the second major application  
716 domain where soft and flexible technologies offer transformative advantages over conventional  
717 rigid systems. The fundamental value proposition is mass efficiency: high-strength fabrics

718 such as Vectran and Kevlar possess specific tensile strengths of 2,330 and 2,080 kN·m/kg  
 719 respectively at the fabric level (or 2,500 kN·m/kg for Kevlar 49 filament)—more than an  
 720 order of magnitude greater than titanium alloy Ti-6Al-4V at 220 kN·m/kg or aluminium  
 721 7075 at 204 kN·m/kg Valle et al. [2019a]. This advantage translates directly into the ability  
 722 to launch habitable volumes that would be physically impossible with metallic construction  
 723 within current launch vehicle fairing constraints. A fabric-walled habitat is not merely a  
 724 lighter alternative to a metallic module; it enables architectural possibilities—volumes of  
 725 300–1,400 m<sup>3</sup>—that have no rigid equivalent.

726 This section traces the heritage of inflatable space habitation from its origins in 1960 to  
 727 the present day (Section 4.1), reviews current commercial programs (Section 4.2), surveys  
 728 future concepts for lunar, Martian, and planetary applications (Section 4.3), and addresses  
 729 the critical issue of radiation shielding with an honest assessment of the BEAM solar particle  
 730 event findings (Section 4.4).

### 731 4.1 Heritage Timeline: Echo to BEAM

732 The heritage of inflatable space structures spans over six decades, progressing through a  
 733 non-linear TRL trajectory marked by both remarkable successes and programmatic setbacks.  
 734 Table 7 summarises the key milestones.

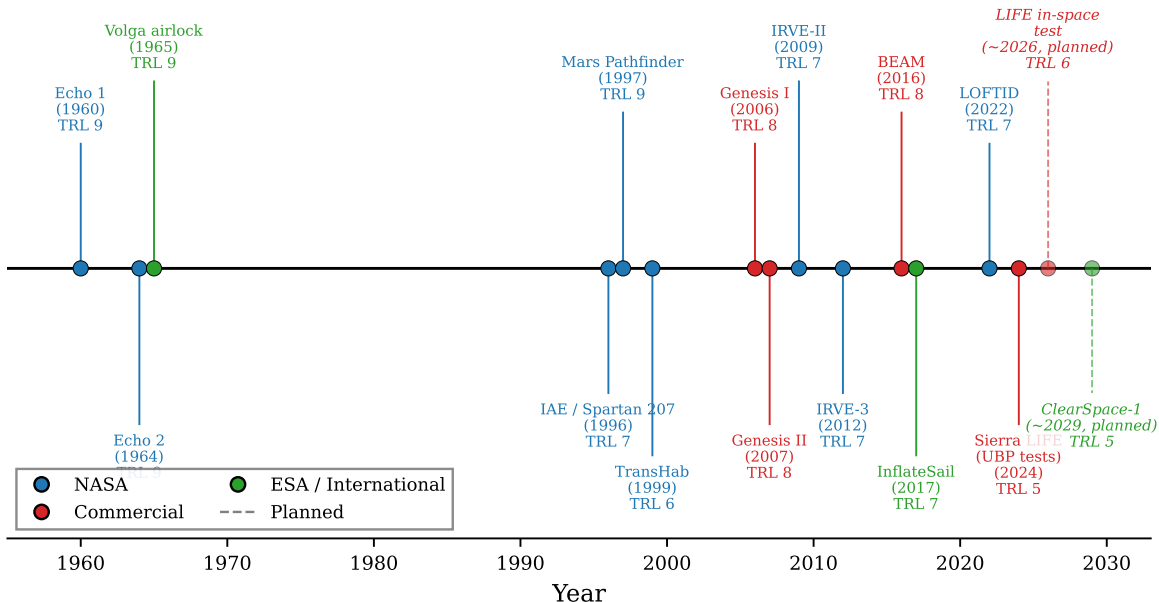


Figure 3: Heritage timeline of inflatable space structures from Echo 1 (1960) to LOFTID (2022), illustrating the progression from passive communication reflectors through human-rated habitats to active aerodynamic decelerators. Colour coding indicates programme origin; marker size reflects achieved TRL.

Table 7: Heritage timeline of inflatable space structures, from passive communication reflectors to human-rated orbital habitats. TRL ratings reflect achieved (not planned) readiness at programme conclusion or present status.

<b>Year</b>	<b>Programme</b>	<b>TRL</b>	<b>Key Achievement</b>
1960	Echo 1 (NASA)	9	30.5 m (100 ft) Mylar sphere; 8+ years on-orbit; global communications relay
1965	Volga airlock (USSR)	9	First human-rated inflatable; Voskhod-2 EVA (Leonov); 40 airbags, 3 independent groups, 7 min inflation
1996	IAE/Spartan 207 (NASA)	7	14 m antenna; 28 m Kevlar/Neoprene booms; Shuttle deployment demonstration
1997	Mars Pathfinder airbags	9	Vectran fabric; operational landing on 3 missions (Pathfinder, Spirit, Opportunity)
1997–2000	TransHab (NASA JSC)	5–6	8.2 m × 11 m; 5-layer shell; tested to 4× operating pressure; cancelled by Congress (HR 1654)
2006–07	Genesis I/II (Bigelow)	7–8	Orbital validation; 2.5+ years on-orbit; pressure retention confirmed
2009	IRVE-II (NASA LaRC)	7	3 m inflatable reentry vehicle experiment; suborbital demonstration
2016+	BEAM (Bigelow/NASA)	9	16 m <sup>3</sup> ; 1,415 kg; 8+ years on ISS; converted to cargo storage; operational
2022	LOFTID (NASA)	7–8	6 m inflatable aerodecelerator; orbital reentry at Mach 30

#### 735 4.1.1 Early Inflatables: Echo and Volga (1960–1965)

736 Project Echo, initiated by NASA in 1960, deployed Echo 1 as a 30.5 m diameter Mylar  
737 balloon serving as a passive communications reflector [Litteken \[2019\]](#). The satellite operated  
738 for over eight years and enabled global communications experiments and geodetic measure-  
739 ments. Echo 2 (1964) advanced the concept with a rigidisable aluminium foil/Mylar laminate  
740 structure. While neither was habitable, the Echo programme demonstrated that large, thin-  
741 walled inflatable structures could survive the LEO environment for extended periods.

742 The Volga airlock, deployed for the Voskhod-2 mission in 1965, represents the first human-  
743 rated inflatable space structure [Litteken \[2019\]](#). Designed for Alexei Leonov’s historic first  
744 spacewalk, the Volga used 40 airbags arranged in three independent groups to inflate a 2.4 m  
745 long, 1.2 m diameter cylindrical airlock in seven minutes. The successful EVA validated  
746 the fundamental concept that pressurised inflatable structures could safely support human  
747 operations in space, albeit for a single use.

#### 748 4.1.2 TransHab: Proving the Five-Layer Architecture (1997–2000)

749 The Transit Habitat (TransHab) programme at NASA Johnson Space Center represented the  
750 most ambitious inflatable habitat development prior to BEAM. Under Principal Architect  
751 Kriss Kennedy [Kennedy \[2002\]](#) and shell lead Gerard Valle, the team developed an 8.2 m  
752 diameter, 11 m long module with a five-layer shell architecture that has become the standard  
753 for all subsequent inflatable habitat designs [Valle et al. \[2019a\]](#):

- 754 1. **Inner liner:** Nomex scuff protection layer.
- 755 2. **Bladder:** Multiple redundant layers, oversized relative to the restraint layer and car-  
756 rying zero structural load.
- 757 3. **Restraint layer:** Tight basket-weave Kevlar/Vectran biaxial membrane, designed to  
758 a safety factor of  $4.0\times$  per NASA-STD-5001.
- 759 4. **MMOD shield:** Ceramic (Nextel) bumper, open-cell foam spacer, and Kevlar rear  
760 wall—vacuum-packed for launch, with foam self-expanding in orbit.
- 761 5. **Multi-layer insulation (MLI):** 19 layers of double-aluminised Mylar/Kapton, with  
762 perforated inner layers for venting during depressurisation.

763 TransHab was tested to  $4\times$  ambient pressure ( $>54$  psig) in a September 1998 hydrostatic  
764 burst test, and full-scale vacuum deployment was demonstrated [Kennedy \[2002\]](#). Hyperveloc-  
765 ity impact testing confirmed that the MMOD shield outperformed the aluminium structure  
766 of ISS modules. The programme also pioneered the water wall radiation shelter concept,  
767 positioning crew quarters within a rigid central core surrounded by water-filled containers  
768 for radiation protection [Kennedy \[2002\]](#).

769 Despite reaching TRL 5–6, TransHab was cancelled by Congressional action (HR 1654,  
770 2000). The technology investment was preserved through patent licensing to Bigelow Aerospace,  
771 which continued development commercially [Kennedy \[2002\]](#).

### 772 4.1.3 Genesis and BEAM: Orbital Validation (2006–2016+)

773 Bigelow Aerospace launched Genesis I (2006) and Genesis II (2007) as uncrewed orbital test  
774 modules, demonstrating pressure retention (69.6–72.4 kPa for Genesis II) and thermal per-  
775 formance (average 26°C, range 4.5–32°C for Genesis I) over 2.5+ years [Litteken \[2019\]](#). These  
776 missions validated the TransHab-derived shell architecture in the actual orbital environment  
777 for the first time.

778 The Bigelow Expandable Activity Module (BEAM), launched to the International Space  
779 Station in April 2016, represents the culmination of this heritage. BEAM provides 16 m<sup>3</sup> of  
780 habitable volume at a mass of 1,415 kg (88 kg/m<sup>3</sup>), compared to 137 kg/m<sup>3</sup> for the Columbus  
781 module and 205 kg/m<sup>3</sup> for the Tranquility node [Valle et al. \[2019a\]](#). While BEAM’s mass-  
782 per-volume ratio is higher than TransHab’s projected 39 kg/m<sup>3</sup>—reflecting BEAM’s small  
783 size and relatively heavy end-fittings—the comparison to metallic modules demonstrates the  
784 efficiency advantage of fabric-walled construction [Valle et al. \[2019a\]](#).

785 BEAM’s deployment provided a critical engineering lesson. Initial expansion attempts  
786 failed, and the module required 25 short pressure bursts over approximately 7 hours to  
787 achieve full deployment—in contrast to the planned rapid inflation sequence [NASA Johnson  
788 Space Center \[2017\]](#). The root cause was attributed to softgoods layers adhering after years  
789 of compression in the launch configuration. For future free-flying deep-space modules where  
790 ISS crew intervention would not be available, this deployment failure mode must be resolved  
791 through autonomous inflation protocols.

792 After its planned two-year demonstration, BEAM’s mission was extended to at least 2028.  
793 The module has been converted to active cargo storage (approximately 130 cargo transfer  
794 bags), demonstrating practical volumetric value beyond its test objectives [NASA Johnson  
795 Space Center \[2017\]](#). No pressure loss, structural degradation, or significant MMOD impacts  
796 have been recorded in over eight years of operation. The Distributed Impact Detection  
797 System (DIDS) has continuously monitored for debris impacts throughout the mission.

## 798 4.2 Current Commercial Programs: LIFE, Orbital Reef, and Be- 799 yond

### 800 4.2.1 Sierra Space LIFE

801 The Large Integrated Flexible Environment (LIFE) programme by Sierra Space represents  
802 the most advanced current inflatable habitat development. The programme has conducted  
803 a systematic Ultimate Burst Pressure (UBP) test campaign at NASA Marshall Space Flight  
804 Center, producing two landmark results [Sierra Space Corporation \[2024\]](#):

- 805 • **January 2024 (full-scale):** A full-scale LIFE 285 expandable structure (approx-  
806 imately 300 m<sup>3</sup>, over 6 m tall) burst at 77 psi (531 kPa), exceeding NASA’s rec-  
807 ommended threshold of 60.8 psi (4× the 15.2 psi maximum operating pressure per  
808 NASA-STD-5001) by 27% [Sierra Space Corporation \[2024\]](#).
- 809 • **October–November 2024 (1/3 scale):** The LIFE 10 module burst at 255 psi  
810 (1,758 kPa), achieving a factor of safety of 16× for LEO operations (at 15.2 psi) and  
811 23× for lunar surface operations (at 10.8 psi) [Sierra Space Corporation \[2024\]](#).

812 The LIFE product line spans three variants: LIFE 10 ( $\sim 100\text{ m}^3$  equivalent, 1/3 scale,  
813 for lunar surface applications), LIFE 285 ( $\sim 300\text{ m}^3$ , full-scale, for ISS-attached or free-  
814 flying stations), and LIFE 500 ( $600\text{--}1,440\text{ m}^3$ , exceeding the total pressurised volume of the  
815 ISS) [Sierra Space Corporation \[2024\]](#). The restraint layer uses Vectran straps manufactured  
816 by ILC Dover, the same organisation responsible for TransHab, Mars Exploration Rover, and  
817 BEAM softgoods. Sierra Space is partnered with Blue Origin for the Orbital Reef commercial  
818 space station, which received a \$130M NASA Commercial LEO Destinations (CLD) award  
819 in December 2021. An in-space test is targeted for no earlier than 2026.

#### 820 4.2.2 Historical Context: B330 and Commercial Ecosystem Fragility

821 The history of Bigelow Aerospace provides a cautionary counterpoint. The B330 ( $330\text{ m}^3$ ,  
822  $18,500\text{--}23,000\text{ kg}$ , 24–36 layers totalling approximately  $0.46\text{ m}$  wall thickness [Valle et al.](#)  
823 [\[2019a\]](#)) was the most advanced commercial inflatable habitat design as of 2019, with a full-  
824 scale ground prototype (XBASE) tested under NASA’s NextSTEP programme. The B330’s  
825 restraint design used a distinctive hoop webbing approach (US Patent 7,100,874) differing  
826 from NASA’s basket-weave architecture [Valle et al. \[2019a\]](#).

827 Bigelow Aerospace ceased operations in March 2020 following COVID-19 layoffs, and  
828 BEAM’s ownership was transferred to NASA JSC in December 2021. The collapse of the  
829 most mature commercial inflatable habitat programme illustrates that high TRL does not  
830 guarantee commercial viability. Future programmes cannot rely on government safety nets  
831 to preserve technology investments, and the commercial ecosystem supporting inflatable  
832 habitat development remains fragile.

#### 833 4.2.3 NextSTEP Competitive Landscape

834 NASA’s NextSTEP-2 programme (2016–2019) selected six companies—Bigelow, Boeing,  
835 Lockheed Martin, Orbital ATK, Sierra Nevada Corporation, and NanoRacks—to develop  
836 habitat prototypes for evaluation [NASA \[2016\]](#). Lockheed Martin’s inflatable prototype  
837 achieved a burst pressure of 285 psi with hundreds of sensors and high-speed cameras mon-  
838 itoring the failure [Lockheed Martin \[2022\]](#). However, this programme subsequently pivoted:  
839 the Starlab commercial station (originally Lockheed Martin/NanoRacks) adopted a rigid  
840 architecture with Airbus as partner, abandoning the inflatable approach. Of the six original  
841 NextSTEP-2 companies, only Sierra Space (evolved from Sierra Nevada Corporation) has  
842 continued to develop inflatable habitats. This consolidation, combined with Bigelow’s exit,  
843 suggests that the inflatable habitat technology faces unresolved commercialisation challenges  
844 that complement the technical risks discussed elsewhere.

### 845 4.3 Future Concepts: Lunar Surface, Mars Transit, Planetary En- 846 try

#### 847 4.3.1 Lunar Surface Habitats

848 Multiple concepts have been proposed for inflatable habitats on the lunar surface, where  
849 the reduced gravity ( $1/6\text{ g}$ ) and absence of orbital debris shift the design requirements  
850 from MMOD protection toward radiation shielding and dust management. The ESA-Hassell

851 collaboration has designed a scalable inflatable pod system at the Shackleton Crater (lunar  
852 south pole), partially constructed from lunar regolith via 3D printing and expandable to  
853 house up to 144 people [Hassell Studio and European Space Agency \[2024\]](#). The ESA-SOM  
854 Moon Village concept proposes a semi-inflatable shell that doubles its internal volume upon  
855 deployment, supporting a four-person crew for up to 300 days [Skidmore, Owings & Merrill  
856 and European Space Agency \[2019\]](#). The ESA Pneumocell concept is specifically designed  
857 for burial under 4–5 m of regolith, using the lunar soil itself as radiation shielding [European  
858 Space Agency \[2018\]](#)—an elegant solution that leverages the inflatable structure’s compliance  
859 to conform to the excavated cavity.

860 For lunar operations, the MMOD layer that constitutes approximately 68% of the shell  
861 mass in LEO [Valle et al. \[2019a\]](#) can be substantially reduced or eliminated, offering signifi-  
862 cant mass savings. However, lunar dust intrusion and abrasion present a new challenge for  
863 flexible fabric surfaces that has not been addressed in any inflatable habitat design to date.

### 864 4.3.2 Mars Transit and Surface Applications

865 TransHab was originally conceived as a Mars transit vehicle, and the deep-space habitat  
866 architecture inherits directly from this heritage. Valle et al. [Valle et al. \[2019a\]](#) present a  
867 launch-to-activation deployment flowchart for a deep-space inflatable habitat, identifying key  
868 operational challenges: autonomous deployment without crew intervention, up to 4 kW of  
869 heater power required post-inflation to bring the bladder above minimum operating tem-  
870 perature, and up to 24 hours before crew entry is permitted. For a three-year Mars transit  
871 mission at solar minimum with three solar particle events (SPEs), radiation shielding re-  
872 quirements range from 25 cm to 400 cm of water equivalent depending on the allowable bone  
873 marrow dose [Valle et al. \[2019a\]](#)—a significant design driver discussed further in Section 4.4.

874 Mars surface applications extend to entry systems. The Low-Earth Orbit Flight Test of  
875 an Inflatable Decelerator (LOFTID, 2022) demonstrated a 6 m diameter inflatable aerodecel-  
876 erator at Mach 30 during orbital reentry [NASA \[2022\]](#), achieving TRL 7–8 and establishing  
877 the viability of inflatable heat shields for planetary entry. The Inflatable Reentry Vehicle  
878 Experiment (IRVE-II, 2009) had previously validated a 3 m prototype in suborbital flight [Lit-  
879 teken \[2019\]](#). For Mars, where the thin atmosphere limits the effectiveness of parachutes for  
880 large payloads, inflatable aerodecelerators offer the only viable path to landing human-scale  
881 masses (>20 tonnes) on the surface. More exotic concepts include the HAVOC Venus air-  
882 ship and the Titan Aerover blimp, both leveraging inflatable structures for buoyancy-based  
883 exploration [Litteken \[2019\]](#).

### 884 4.3.3 European Programmes

885 European contributions to inflatable habitat development include the ASI-funded FLECS  
886 (Flexible Commercial Structure), the ESA-funded IHAB (Inflatable Habitation) and IMOD  
887 (Inflatable Module) programmes, and the 2002 ESA/ESTEC First European Workshop  
888 on Inflatable Space Structures (ESA-WPP-200) [ESA/ESTEC \[2002\]](#). These programmes  
889 have contributed materials characterisation, hypervelocity impact testing of flexible MMOD  
890 shields (notably Destefanis et al. [Destefanis et al. \[2006\]](#)), and architectural concepts. How-  
891 ever, it must be noted that no European inflatable has flown in a habitation role. After

892 more than two decades of investment, all European inflatable habitat programmes remain at  
893 TRL 2–4. The Volga airlock (1965) remains the only European-adjacent (Soviet-era) flight  
894 precedent for a human-rated inflatable in space.

#### 895 4.4 Radiation Shielding: The BEAM SPE Findings and Design Im- 896 plications

897 Radiation shielding represents the single most serious unresolved technical challenge for  
898 inflatable habitats in deep space. The BEAM module has provided the only in-flight radiation  
899 data for an inflatable habitat, and the findings demand honest assessment.

900 During the September 2017 solar particle event (SPE), radiation dosimeters inside BEAM  
901 recorded approximately 2–2.5 mGy, compared to approximately 0.25 mGy measured in typ-  
902 ical ISS metallic habitable modules during the same event—a ratio of 8–10× higher dose  
903 inside the inflatable module [NASA Johnson Space Center \[2017\]](#). For galactic cosmic ra-  
904 diation (GCR), which is continuous rather than episodic, BEAM dose rates were similar  
905 to other ISS modules at baseline, indicating that the fabric shell provides adequate GCR  
906 shielding in LEO where the Earth’s magnetic field supplies primary protection.

907 The SPE finding has significant implications:

- 908 • **Fabric walls alone are insufficient for SPE protection.** The multi-layer shell  
909 (60+ individual layers, 30–50 cm total thickness) provides substantially less shielding  
910 than the aluminium structure of ISS modules during particle events.
- 911 • **The mitigation is designed-in, not absent.** Both TransHab and the LIFE archi-  
912 tecture incorporate a rigid central core functioning as a storm shelter during SPEs.  
913 Crew quarters are positioned within this core, surrounded by water wall containers  
914 (a concept originating with Kennedy’s TransHab design [Kennedy \[2002\]](#)) that provide  
915 effective hydrogen-rich shielding. The inflatable volume provides habitable space for  
916 non-storm operations, while the rigid core provides radiation protection.
- 917 • **Material selection matters.** Polyethylene provides 27.8% mass savings compared to  
918 aluminium for equivalent radiation shielding effectiveness, and three-layer composite  
919 shields (combining high-Z, medium-Z, and low-Z materials) achieve up to 70% total  
920 ionising dose improvement for electrons and 50% for protons [Norbury et al. \[2025\]](#).

921 For deep-space missions beyond Earth’s magnetosphere, the GCR environment is more  
922 severe and continuous. Valle et al. [Valle et al. \[2019a\]](#) model that a three-year deep-space  
923 mission at solar minimum with three SPEs requires between 25 cm and 400 cm of water-  
924 equivalent shielding depending on the allowable bone marrow dose—translating to substan-  
925 tial mass within the rigid core. Active magnetic shielding and pharmaceutical countermea-  
926 sures remain at low TRL and are not viable near-term solutions.

927 The honest framing is that inflatable habitats are *not* radiation protection structures,  
928 and were never designed to be. They are mass-efficient volume structures with integrated  
929 MMOD protection. Radiation protection is the responsibility of the rigid core and water wall  
930 architecture. The BEAM SPE data confirms this design philosophy rather than undermining  
931 it, but the data must be presented without minimisation to maintain credibility with the

932 radiation protection community. The absence of post-2017 follow-up publications detailing  
933 BEAM’s continued radiation environment data over its now eight-year mission represents a  
934 gap in the available evidence base that future studies should address.

## 935 5 State of the Art: Materials and Structures

936 The material systems underpinning inflatable space structures occupy a unique design space:  
937 they must combine the tensile strength of structural metals, the flexibility to package into  
938 compact launch volumes, and the environmental durability to survive atomic oxygen, ultra-  
939 violet radiation, and micrometeoroid impacts for mission lifetimes spanning years to decades.  
940 This section reviews the four dominant fabric families, the canonical multi-layer shell archi-  
941 tecture derived from TransHab, established rigidisation technologies, and the environmental  
942 degradation mechanisms that govern long-term performance.

### 943 5.1 Space-Rated Fabrics: Vectran, Kevlar, Zylon, Nextel

944 Four high-performance fabric families dominate inflatable space structure design, each oc-  
945 cupying a distinct functional niche determined by the intersection of mechanical properties,  
946 environmental tolerance, and flight heritage.

947 **Vectran HT** (liquid crystal polymer, Kuraray Co.) has emerged as the preferred ma-  
948 terial for restraint layers in inflatable habitats. With a tensile strength of approximately  
949 3.0 GPa at a density of 1.40 g/cm<sup>3</sup>, Vectran achieves a specific strength of 2,330 kN·m/kg—  
950 an order of magnitude above Ti-6Al-4V (220 kN·m/kg) and Al 7075 (204 kN·m/kg) [Valle](#)  
951 [et al. \[2019b\]](#). Vectran’s principal advantage over the earlier-generation Kevlar is its superior  
952 creep resistance: under sustained load at the NASA-mandated factor of safety of 4.0 (corre-  
953 sponding to 25% of ultimate tensile strength), Vectran fabric exhibits no failure over extended  
954 test periods of months [Weadon \[2013\]](#). This characteristic is critical because creep is the life-  
955 limiting mechanism for restraint layers in pressure-stabilised structures. However, Weadon’s  
956 systematic characterisation revealed that time-to-failure is exponentially sensitive to load  
957 level, and manufacturing variability in ultimate tensile strength ( $\pm 10\%$  for 12K webbing,  
958  $\pm 6\%$  for 6K webbing) introduces significant uncertainty in lifetime prediction—at 75–85%  
959 UTS, time-to-failure ranges from 4 minutes to 5.5 months for identical test configurations  
960 [Weadon \[2013\]](#). This finding underscores the importance of quality control in inflatable  
961 habitat fabrication. Two important qualifications must be noted. First, Weadon’s creep  
962 characterisation was conducted at room temperature; no published Vectran creep dataset  
963 exists for space-representative thermal cycling conditions (approximately  $-100^{\circ}\text{C}$  to  $+120^{\circ}\text{C}$   
964 for LEO), and the effective creep rate under such cycling may differ significantly from room-  
965 temperature data—this represents a critical materials gap for habitat lifetime prediction.  
966 Second, the “no failure over extended test periods” result at 25% UTS, while encouraging, is  
967 based on a limited number of specimens at the design operating point; given the wide man-  
968 ufacturing variability, confidence intervals on lifetime prediction remain large, and the creep  
969 behaviour exhibits bimodal characteristics where some specimens show substantially earlier  
970 failure than others at identical load levels. Vectran’s flight heritage includes Mars Pathfinder  
971 airbags (1997), BEAM restraint layers (2016–present), and the Sierra Space LIFE program

972 [Litteken \[2019\]](#).

973 **Kevlar 49** (poly-paraphenylene terephthalamide, DuPont) was the original restraint  
974 layer material for TransHab, with a tensile strength of approximately 3.0 GPa at the fabric  
975 level and 3.6 GPa at the individual filament level, at a density of 1.44 g/cm<sup>3</sup> [Valle et al.](#)  
976 [\[2019b\]](#), [DuPont \[2019\]](#). The corresponding specific strength is 2,080 kN·m/kg (fabric) or  
977 2,500 kN·m/kg (filament); throughout this survey, fabric-level properties are reported un-  
978 less otherwise noted, as these are the engineering-relevant values for woven restraint layers.  
979 While Kevlar’s fabric-level specific strength is comparable to Vectran’s, its higher creep rate  
980 under sustained biaxial loading led to its replacement by Vectran in subsequent habitat de-  
981 signs [Kennedy \[2002\]](#). Kevlar retains an important role as a rear-wall material in multi-layer  
982 micrometeoroid and orbital debris (MMOD) shields, where its combination of high energy  
983 absorption and relatively low cost makes it the material of choice for fragment capture layers  
984 [Destefanis et al. \[2003\]](#). Space environment characterisation by Destefanis et al. confirmed  
985 that Kevlar suffers UV-induced discoloration and embrittlement but shows acceptable perfor-  
986 mance when shielded from direct solar exposure within the MMOD sub-assembly [Destefanis](#)  
987 [et al. \[2009\]](#).

988 **Zylon** (poly-p-phenylene-2,6-benzobisoxazole, PBO; Toyobo Co.) offers the highest ten-  
989 sile strength of any commercially available high-performance fibre at 5.8 GPa, yielding a  
990 specific strength of 3,840 kN·m/kg [Toyobo Co., Ltd. \[2005\]](#). However, Zylon exhibits catas-  
991 trophic UV degradation: strength loss of approximately 35% within 6 months of unshielded  
992 exposure, rendering it unsuitable for any application without comprehensive UV protec-  
993 tion [Toyobo Co., Ltd. \[2005\]](#), [Said et al. \[2006\]](#). Despite this limitation, Zylon has found  
994 niche space applications where UV shielding is inherently provided: SpaceX Crew Dragon  
995 parachute risers and NASA high-altitude balloon tendons [Litteken \[2019\]](#). For inflatable  
996 structures, Zylon could serve in interior tensile elements (e.g., floor suspension webbings  
997 within pressurised habitats) where the multi-layer shell provides UV shielding, but its UV  
998 sensitivity effectively precludes use in any externally exposed role.

999 **Nextel 440** (3M alumina-boria-silica ceramic fabric) occupies a unique position as the  
1000 only ceramic fibre used in inflatable space structures. With a density of 3.05 g/cm<sup>3</sup> and con-  
1001 tinuous use temperature of 1370°C, Nextel is employed exclusively as the outer bumper layer  
1002 in MMOD shielding [Christiansen and Davis \[2019\]](#), [Destefanis et al. \[2003\]](#). Upon hyperveloc-  
1003 ity impact, Nextel fragments incoming particles into smaller, more widely dispersed debris,  
1004 reducing the energy density impinging on subsequent shield layers. The stuffed Whipple  
1005 configuration (Nextel bumper + open-cell foam + Kevlar rear wall) protects against projec-  
1006 tiles approximately twice the diameter of those defeated by a standard aluminium Whipple  
1007 shield at equal areal density [Destefanis et al. \[2003\]](#). Nextel is inherently immune to UV and  
1008 atomic oxygen degradation due to its ceramic composition, but its high density limits its use  
1009 to the thin bumper layer.

1010 Two additional materials complete the palette for inflatable structures. **Beta cloth**  
1011 (PTFE-coated fibreglass) serves as the outermost atomic oxygen protection cover layer, with  
1012 LDEF flight data demonstrating excellent durability over 68 months of LEO exposure [Linton](#)  
1013 [et al. \[1993\]](#), [Banks et al. \[2004\]](#). **Kapton H** (polyimide, DuPont) is the workhorse film for  
1014 multi-layer insulation, operating from  $-269^{\circ}\text{C}$  to  $+400^{\circ}\text{C}$ , though it is susceptible to atomic  
1015 oxygen erosion at a rate of  $3.0 \times 10^{-24}$  cm<sup>3</sup>/atom [Banks et al. \[2004\]](#), [Finckenor and Dooling](#)  
1016 [\[1999\]](#).

1017 Table 8 presents a comprehensive comparison of these material systems across eight  
 1018 performance parameters relevant to inflatable space structures.

Table 8: Comparison of space-rated materials for inflatable structures.

Material	Type	$\sigma_{\text{UTS}}$ (GPa)	$\rho$ (g/cm <sup>3</sup> )	$T_{\text{max}}$ (°C)	UV Sens.	AO Resist.	Primary Role	TRL
Vectran HT	LCP fibre	3.0	1.40	330	Mod.	Low	Restraint	9
Kevlar 49	Aramid	3.0	1.44	427	High	Low	MMOD rear	9
Zylon AS	PBO fibre	5.8	1.54	650	V. High	Low	Interior only	7
Nextel 440	Ceramic	—	3.05	1370	None	N/A	MMOD bumper	9
Kapton H	Polyimide	0.23	1.42	400	Low	Low	MLI layers	9
Beta cloth	PTFE/glass	0.34	—	650	Low	High	AO cover	9

Table 9: Specific strength comparison: high-performance fabrics versus structural metals  
 (data from Valle et al. [Valle et al. \[2019b\]](#)).

Material	$\sigma_{\text{UTS}}$ (GPa)	$\rho$ (g/cm <sup>3</sup> )	Specific Strength (kN·m/kg)	Ratio to Ti-6Al-4V
Zylon AS	5.8	1.54	3,840	17.5×
Kevlar 49 (fabric)	3.0	1.44	2,080	9.5×
Vectran HT	3.0	1.40	2,330	10.6×
Ti-6Al-4V	0.95	4.43	220	1.0×
Al 7075-T6	0.57	2.81	204	0.9×

## 1019 5.2 Multi-Layer Shell Architecture

1020 The TransHab program (1997–2000) established the canonical five-layer shell architecture  
 1021 that remains the reference design for all subsequent inflatable habitats [Kennedy \[2002, 2016\]](#).  
 1022 From innermost to outermost, the layers are:

- 1023 1. **Liner:** Nomex fabric backed by Kevlar felt provides the crew-contact interior surface,  
 1024 offering acoustic attenuation and a substrate for equipment mounting.
- 1025 2. **Bladder:** Three redundant layers of polymeric gas barrier (Combitherm or urethane-  
 1026 coated Nylon), each sandwiched between Kevlar felt separators. The bladder is deliber-  
 1027 ately oversized relative to the restraint layer so that it carries no structural load—the  
 1028 positive pressure differential is transmitted entirely to the restraint layer [Kennedy](#)  
 1029 [\[2016\]](#). The triple redundancy ensures continued pressure containment after a single-  
 1030 layer puncture.
- 1031 3. **Restraint layer:** The primary load-carrying element, comprising Kevlar (TransHab)  
 1032 or Vectran (BEAM and subsequent designs) in a biaxial basket-weave configuration.  
 1033 TransHab’s restraint layer was designed to sustain 12,500 lb/in hoop loading and

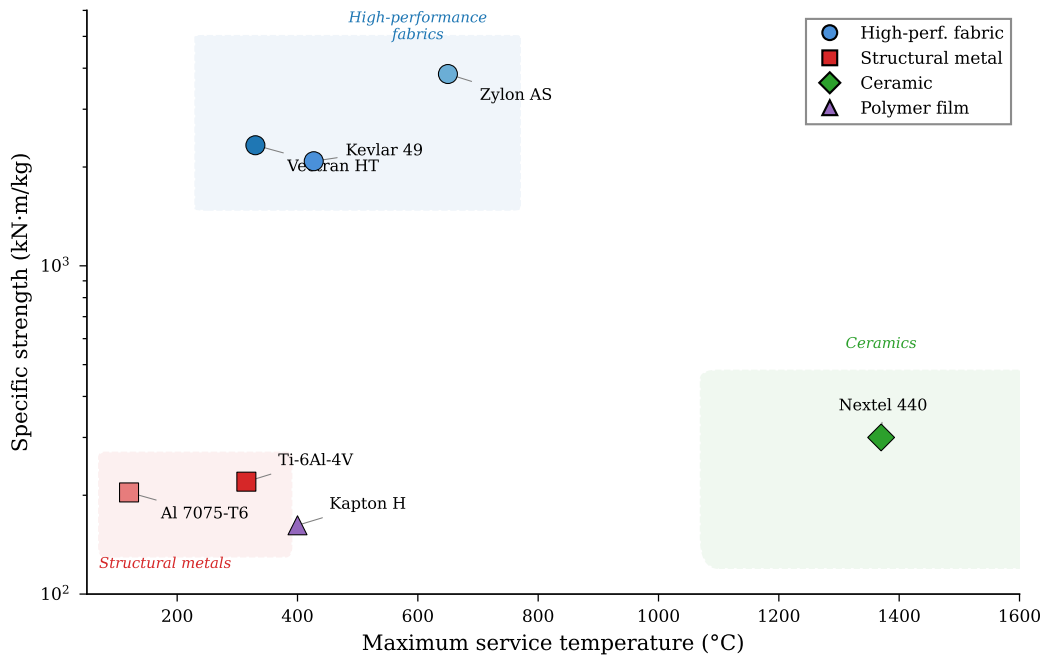


Figure 4: Materials Ashby chart comparing specific strength versus maximum service temperature for space-rated fabrics and structural metals. High-performance fabrics (Vecran, Kevlar, Zylon) occupy a design space inaccessible to metals, combining an order-of-magnitude advantage in specific strength with adequate thermal performance for LEO applications.

1034  
1035  
1036  
1037  
1038  
  
1039  
1040  
1041  
1042  
1043  
1044  
1045  
1046  
1047  
1048  
  
1049  
1050  
1051  
1052  
1053  
1054  
1055  
  
1056  
1057  
1058  
1059  
1060  
1061

6,000 lb/in axial loading at a factor of safety of 4.0 per NASA-STD-5001 Kennedy [2016]. The restraint layer attaches to rigid bulkheads via clevis fittings that transfer membrane loads to the metallic core structure. Ground testing demonstrated sustained pressure at 4× operating pressure (60 psid) without failure, and burst at 196 psid in sub-scale articles Kennedy [2002].

4. **MMOD shield:** A stuffed Whipple configuration comprising Nextel 440 ceramic fabric bumper layers, open-cell polyurethane foam spacers, and Kevlar rear walls Deste-fanis et al. [2003]. The MMOD assembly is vacuum-packed during launch to maintain the folded configuration and expands passively on orbit when exposed to vacuum. TransHab’s MMOD design was tested against projectiles up to 1.7 cm diameter at hypervelocity, meeting the no-penetration probability requirement of  $P_{NP} \geq 0.9820$  Kennedy [2002]. Damage tolerance testing by Trevino et al. demonstrated that a 2 in × 3.5 in hole in the restraint layer at 25% of burst pressure resulted in load redistribution without catastrophic failure—an inherent advantage of woven textile structures over metallic shells Edgecombe et al. [2009].
5. **Thermal protection system (TPS):** Multi-layer insulation comprising nylon-reinforced double-aluminized Mylar and double-aluminized Kapton layers, with inner layers perforated for gas venting during deployment Finckenor and Dooling [1999]. The outermost element is an atomic oxygen cover of Beta glass fabric for LEO operations Kennedy [2016]. Effective emittance values for properly installed MLI range from 0.015 to 0.05, though practical performance with seams, penetrations, and attachment hardware typically falls at the upper end of this range Finckenor and Dooling [1999], Gilmore [2002].

The total shell assembly comprises 60+ individual layers deployed to a thickness of 30–50 cm Valle et al. [2019b]. For TransHab, the overall packaged dimensions were 10.5 m length with a deployed width of 8.3 m, yielding an internal habitable volume of approximately 161 m<sup>3</sup> and a total packaged shell volume of 329 m<sup>3</sup> Kennedy [2016]. BEAM, the flight-demonstrated derivative, achieves a habitable volume of 16 m<sup>3</sup> in a 1,415 kg module Valle et al. [2019b].

Table 10: Layer-by-layer specification of the TransHab/BEAM shell architecture. The heritage convention identifies five functional sub-assemblies; the AO cover (Beta cloth) is the outermost element of the TPS sub-assembly but is listed separately here for clarity, yielding six table rows for five sub-assemblies.

Sub-assy	Layer	Material(s)	Function	Key Specific
1	Liner	Nomex + Kevlar felt	Crew contact, acoustic	Non-structural
2	Bladder (×3)	Combitherm / Urethane-Nylon	Gas barrier	3× redundant,
3	Restraint	Vectran basket-weave	Primary structure	FOS = 4.0, 12
4	MMOD	Nextel + foam + Kevlar	Debris protection	$P_{NP} \geq 0.9820$
5	TPS/MLI	Aluminized Mylar/Kapton	Thermal control	$\varepsilon_e = 0.015\text{--}0.0$
	AO cover	Beta glass fabric	AO protection (outer TPS)	LDEF-validate

## TransHab / BEAM Shell Architecture

(five functional sub-assemblies, not to scale)

**Exterior (space environment)**

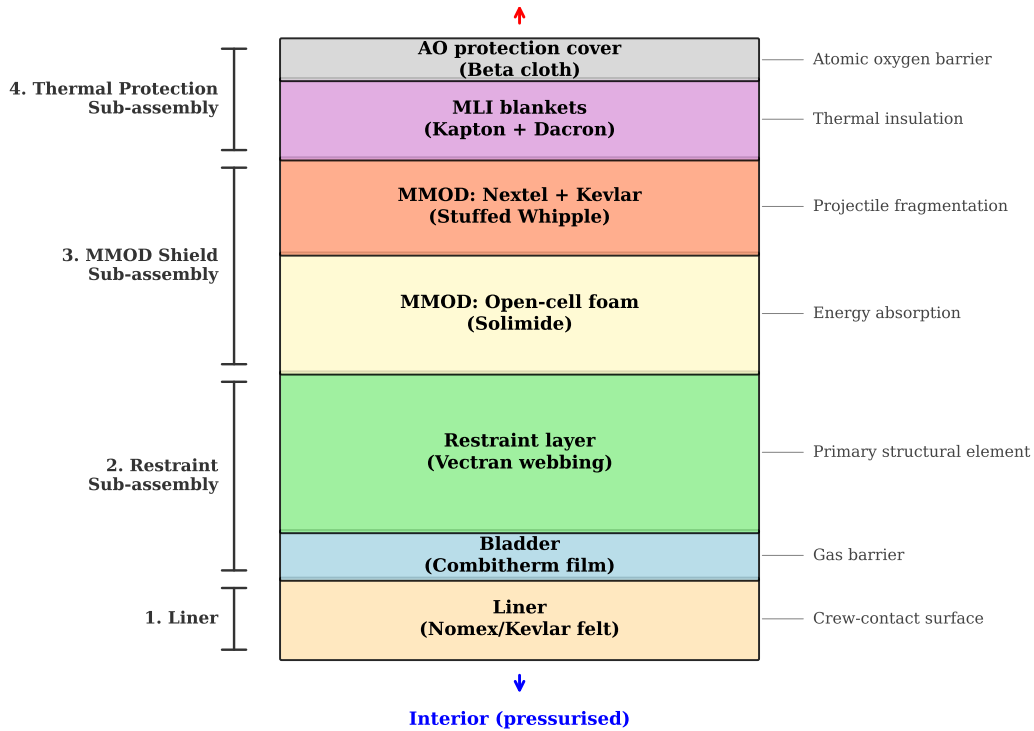


Figure 5: TransHab/BEAM multi-layer shell architecture, showing the five functional sub-assemblies from the crew-contact liner (innermost) to the atomic oxygen protection cover (outermost). The restraint layer (Vectran basket-weave) carries all pressure loads; the bladder, MMOD shield, and thermal protection system are non-structural. Total deployed thickness: 30–50 cm; total number of individual layers: 60+.

### 5.3 Rigidization Technologies

While habitats remain pressure-stabilised throughout their operational life (at a factor of safety of 4.0), many inflatable components—particularly booms, masts, and structural supports—require rigidisation after deployment to eliminate dependence on continued gas containment. Cadogan and Scarborough established the canonical classification of rigidisation technologies into three families [Cadogan and Scarborough \[2001\]](#):

**Mechanical (strain hardening):** Aluminum-polymer laminates (e.g., 14.5  $\mu\text{m}$  Al / 16  $\mu\text{m}$  Mylar / 14.5  $\mu\text{m}$  Al) undergo plastic deformation during inflation, work-hardening the aluminium layers and locking the deployed shape [Schenk et al. \[2014\]](#). This approach has the longest flight heritage, from Echo 2 (1964) through InflateSail (2017), where a 1 m strain-rigidized mast achieved deployment in approximately 2 seconds via CO<sub>2</sub> pressurization [Viquerat et al. \[2019\]](#), [Underwood et al. \[2017\]](#). Lenticular boom cross-sections achieve packaging ratios of approximately 10:1, while circular cross-sections achieve approximately 5:1 under z-fold [Schenk et al. \[2014\]](#). Current TRL: 8–9.

**Physical (sub- $T_g$  and shape memory):** Resin-impregnated composites heated above their glass transition temperature ( $T_g$ ) become pliable for packaging; upon deployment and cooling below  $T_g$  in the space thermal environment, the resin solidifies and rigidizes the structure [Cadogan and Scarborough \[2001\]](#), [Defoort et al. \[2005\]](#). This approach is reversible in principle, enabling re-stowage. Shape memory polymers extend this concept with engineered  $T_g$  transitions. Current TRL: 4–5.

**Chemical (UV-curable):** Cationic epoxy resins cure upon exposure to solar UV radiation, achieving the highest post-rigidisation stiffness of the three approaches [Allred et al. \[2002\]](#). The Rigidization on Command (ROC) technology demonstrated by Adherent Technologies achieves mechanical properties equivalent to thermally cured composites using sunlight alone [Adherent Technologies Inc. \[2001\]](#). However, UV curing requires unobstructed solar access and is sensitive to shadowing by other spacecraft elements. Current TRL: 4–5.

An emerging fourth approach uses shape memory alloy (SMA) elements integrated into inflatable toroidal structures. Patel et al. developed an analytical framework for SMA-based rigidisation where NiTi alloy wires, embedded in the inflatable wall and heated above their austenite finish temperature, contract and lock the deployed geometry [Rastogi et al. \[2024\]](#). This approach remains at the analytical stage (TRL 2–3) but offers the potential for active shape control during rigidisation.

Table 11: Rigidization technology comparison for inflatable space structures.

Method	Mechanism	TRL	Heritage	Best Application
Strain hardening	Al-polymer plastic deformation	8–9	Echo 2, InflateSail	Thin booms, sails
Sub- $T_g$ resin	Glass transition solidification	4–5	Ground demos	Structural booms
UV curing	Solar-initiated polymerization	4–5	Ground demos	Max. stiffness booms
SMA rigidisation	Thermoelastic contraction	2–3	Analytical only	Toroidal structures

A critical distinction: large inflatable habitats (BEAM, TransHab, LIFE) do not employ rigidisation. They remain pressure-stabilised structures throughout their operational life, relying on the continuous pressure differential across the multi-layer shell to maintain

1097 structural integrity at a factor of safety of 4.0 [Valle et al. \[2019b\]](#). Rigidization is primar-  
1098 ily relevant for booms, masts, and structural supports where prolonged gas containment is  
1099 impractical or where a loss-of-pressure failure mode is unacceptable.

## 1100 5.4 Environmental Degradation: AO, UV, Radiation, Creep

1101 Four environmental mechanisms govern the long-term performance of inflatable structures  
1102 in the space environment, each affecting different layers of the shell assembly.

1103 **Atomic oxygen (AO)** is the dominant surface degradation threat in LEO. At ISS  
1104 altitude ( $\sim 400$  km), AO flux is approximately  $10^{15}$  atoms/cm<sup>2</sup>/s, and Kapton H exhibits  
1105 an erosion yield ( $E_y$ ) of  $3.0 \times 10^{-24}$  cm<sup>3</sup>/atom—the practical erosion rate (thickness loss  
1106 per unit time) is  $E_y \times \Phi$ , where  $\Phi$  is the AO flux, which varies with altitude, solar activity,  
1107 and ram direction; at ISS altitude this corresponds to approximately 1  $\mu\text{m}/\text{year}$  [Banks  
1108 et al. \[2004\]](#). Unprotected Mylar, Kevlar, and Vectran all exhibit comparable erosion rates.  
1109 SiO<sub>2</sub> coatings reduce Kapton erosion by 2–3 orders of magnitude, and novel AO-resistant  
1110 polymers (TOR, COR) developed at NASA Glenn demonstrate near-zero erosion [Banks  
1111 et al. \[2004\]](#). In practice, inflatable habitats are protected by the outermost Beta cloth  
1112 layer, which is inherently AO-resistant due to its PTFE coating. In-situ measurements from  
1113 JAXA’s SLATS satellite (160–560 km altitude range) have recently provided direct on-orbit  
1114 validation of erosion models [Verker et al. \[2023\]](#).

1115 **UV degradation** primarily affects Kevlar (discoloration and embrittlement) and Zylon  
1116 (catastrophic strength loss of  $\sim 35\%$  in 6 months) [Destefanis et al. \[2009\]](#), [Toyobo Co., Ltd.  
1117 \[2005\]](#). Vectran shows moderate UV sensitivity. The multi-layer shell architecture naturally  
1118 provides UV shielding for interior layers, but any externally exposed fabric elements require  
1119 dedicated UV protection.

1120 **Radiation effects** on high-performance fabrics are comparatively modest for LEO mis-  
1121 sions. The primary radiation concern for inflatable habitats is crew dose rather than material  
1122 degradation—BEAM measurements during a September 2017 solar particle event recorded  
1123 2–2.5 mGy inside BEAM versus approximately 0.25 mGy in adjacent ISS metallic modules,  
1124 an 8–10 $\times$  ratio attributable to the lower areal density of the fabric shell [NASA Johnson Space  
1125 Center \[2017\]](#). Polyethylene supplemental shielding offers 27.8% mass savings over equivalent  
1126 aluminium shielding, and multi-layer configurations achieve up to 70% total ionizing dose  
1127 improvement for electrons and 50% for protons [Norbury et al. \[2025\]](#).

1128 **Creep** is the life-limiting mechanism for Vectran and Kevlar restraint layers under sus-  
1129 tained biaxial pressure loading. Weadon’s characterisation demonstrated three-stage vis-  
1130 coelastic creep with exponential sensitivity to the ratio of applied load to ultimate tensile  
1131 strength [Weadon \[2013\]](#). At the design operating point of 25% UTS (FOS = 4.0), specimens  
1132 showed no failure over test periods of months. However, the wide manufacturing variability  
1133 in UTS ( $\pm 10\%$ ) dominates lifetime uncertainty—not the average material properties them-  
1134 selves. Combined synergistic effects (AO + UV + thermal cycling + sustained load) remain  
1135 inadequately characterised, representing a research gap that limits confidence in multi-decade  
1136 lifetime predictions for deep-space habitats [Zhai et al. \[2023\]](#).

## 6 State of the Art: Deployment Mechanics

The deployment of inflatable structures in the space environment presents a unique engineering challenge: a large, compliant membrane must transition from a compactly folded launch configuration to a precise deployed geometry under vacuum conditions where gas dynamics, thermal gradients, and material memory effects all influence the final state. This section reviews fold pattern selection, inflation control strategies, and lessons from flight heritage.

### 6.1 Fold Patterns and Packaging Efficiency

The choice of fold pattern determines deployment reliability, packaging efficiency, and the number of actuators required for controlled deployment. Three primary pattern families are employed, each optimised for a different structural geometry.

**Miura-ori** [Miura \[1985\]](#) is the foundational pattern for flat membrane deployment. The tessellation of parallelogram facets creates a one-degree-of-freedom rigid-foldable mechanism: the entire membrane deploys via a single actuator force without requiring elastic deformation of the panels. This property is critical for fragile thin films (metallized Mylar, ceramic-coated Kapton) that cannot sustain repeated fold stress. The negative Poisson's ratio characteristic—contraction in one direction when extended in the perpendicular direction—assists controlled deployment by preventing bunching [Miura \[1985\]](#). Compaction is theoretically unlimited: an  $N \times M$  panel array compacts to a stack of 2 panels thick, achieving compaction ratios of  $N/2$  in each direction. Miura-ori is optimal for solar sails, antenna reflectors, and drag sails where flat-membrane deployment is required.

For **cylindrical structures** (booms, masts), Schenk and Guest adapted the Miura-ori pattern to cylindrical geometry, enabling origami-based compaction of inflatable booms with geometrically determined deployment kinematics [Schenk et al. \[2013, 2014\]](#). The z-fold variant offers the simplest implementation and highest packaging ratio but lower deployment reliability, as individual folds must sequentially release without jamming. Wrapping (coiling) provides more controlled deployment at lower packaging ratios. The lenticular boom cross-section achieves  $\sim 10:1$  packaging ratios versus  $\sim 5:1$  for circular cross-sections [Schenk et al. \[2014\]](#).

For **habitats**, a 7-gore S-fold approach is employed: the bladder and restraint layers are folded in an S-pattern around the rigid central core, with individual MMOD and MLI gore panels attached separately [Kennedy \[2016\]](#), [Valle et al. \[2019b\]](#). The habitat packaging ratio is substantially lower than for membranes or booms because the rigid core occupies a significant fraction of the stowed volume. TransHab achieved a stowed-to-deployed volume ratio of approximately 2.1:1 (habitable volume), while BEAM achieves approximately 4.4:1 (16 m<sup>3</sup> deployed /  $\sim 3.6$  m<sup>3</sup> stowed) [Valle et al. \[2019b\]](#).

### 6.2 Inflation Sequencing and Control

Inflation rate control is critical for successful deployment: inflation that is too rapid generates shock waves in the gas column that can damage thin films and cause asymmetric expansion, while inflation that is too slow allows thermal gradients to develop that affect the final geometry [Jenkins \[2001\]](#). Minimum tension requirements must be maintained throughout

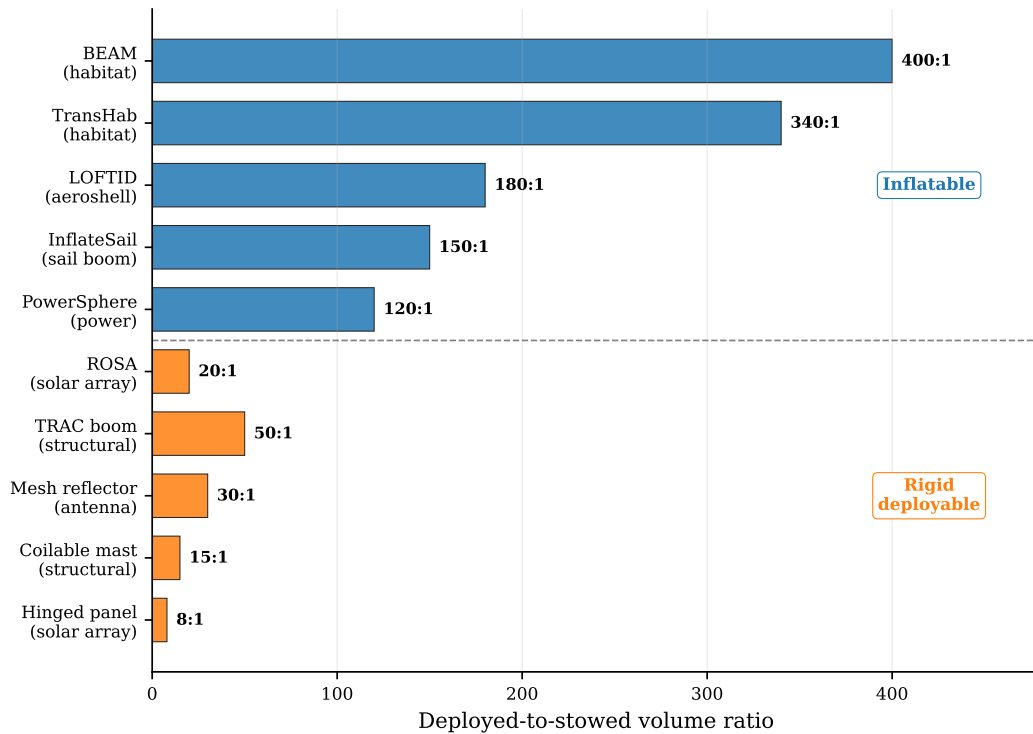


Figure 6: Deployed-to-stowed volume ratio comparison between inflatable and rigid deployable structures. Inflatable systems achieve packaging ratios an order of magnitude higher than rigid deployable alternatives, with BEAM demonstrating a 400:1 ratio. Data compiled from mission documentation and manufacturer specifications.

Table 12: Packaging efficiency by structure type for inflatable space systems.

Structure Type	Fold Pattern	Packaging Ratio	Heritage Example
Flat membrane (sail)	Miura-ori / z-fold	~500:1 (membrane)	InflateSail (10 m <sup>2</sup> )
Boom (lenticular)	Origami / coil	~10:1	InflateSail (1 m boom)
Boom (circular)	z-fold	~5:1	Various CubeSat booms
Habitat (with rigid core)	7-gore S-fold	2–5:1	BEAM (~4.4:1), TransHab
Origami shield	Waterbomb tessellation	~5:1 (80% expansion)	IMSS concept <a href="#">Cha et al. [20]</a>

1177 inflation to prevent wrinkling, which can create permanent creases in metallized films and  
1178 compromise thermal or RF performance.

1179 The BEAM deployment sequence provides the most instructive flight data on inflation  
1180 control challenges. Initial deployment in May 2016 failed to expand BEAM beyond a small  
1181 fraction of its intended volume. Over the following 7 hours, mission controllers executed  
1182 25 sequential pressure bursts, each providing a small increment of expansion, before BEAM  
1183 reached its full deployed geometry [NASA Johnson Space Center \[2017\]](#). This arduous recovery  
1184 illustrates a fundamental tension: the folded softgoods develop stronger memory effects  
1185 during extended stowed periods than ground testing predicted, requiring more expansion  
1186 energy than designed. For autonomous missions (lunar surface habitats, Mars transit mod-  
1187 ules), such manual intervention is not viable, and deployment reliability must be established  
1188 at substantially higher confidence levels [Valle et al. \[2019b\]](#).

1189 Several inflation methodologies have been demonstrated or proposed. **Stored gas** (typi-  
1190 cally CO<sub>2</sub> or N<sub>2</sub>) provides the most controllable inflation but requires tanks, regulators, and  
1191 plumbing that add mass and failure modes. InflateSail used a cold-gas CO<sub>2</sub> system for boom  
1192 deployment [Viquerat et al. \[2019\]](#). **Sublimation-based inflation** eliminates gas handling  
1193 hardware: benzoic acid or naphthalene powder generates sufficient vapour pressure at ambi-  
1194 ent space temperatures to inflate simple structures, though residual air in the packed struc-  
1195 ture can cause premature partial inflation [Horn \[2017\]](#). The PowerSphere concept employed  
1196 passive vapour-pressure inflation from sublimation powder for a multifunctional sphere [Cado-  
1197 gan et al. \[2006\]](#). **Active pressure control** using real-time pressure-volume feedback with  
1198 variable inflation rates has been studied analytically by Wei et al., who demonstrated that  
1199 instantaneous optimal control of inflation rate can minimise deployment loads and improve  
1200 final shape accuracy [Li et al. \[2022a\]](#).

### 1201 **6.3 Flight Heritage: InflateSail, LOFTID, BEAM Deployment Lessons**

1202 Three flight demonstrations provide the primary deployment heritage for inflatable struc-  
1203 tures, each operating at a different scale and in a different deployment regime.

1204 **InflateSail** (2017) demonstrated the most compact packaging and fastest deployment: a  
1205 1 m aluminium-Mylar laminate boom (14.5  $\mu\text{m}$  Al / 16  $\mu\text{m}$  Mylar / 14.5  $\mu\text{m}$  Al) and 10 m<sup>2</sup>  
1206 aluminized Mylar drag sail packaged into a 0.5U volume ( $\sim$ 50 mm cube), deploying and  
1207 strain-rigidizing in approximately 2 seconds via CO<sub>2</sub> pressurization [Viquerat et al. \[2019\]](#).  
1208 The deployed membrane-to-stowed volume ratio of approximately 500:1 represents the high-  
1209 est documented packaging efficiency for a complete deployable system. InflateSail de-orbited  
1210 from 505 km in 72 days, compared to an estimated 4+ years without the sail, validating the  
1211 drag deorbit concept at TRL 8–9 [Viquerat et al. \[2019\]](#).

1212 **IRVE-3** (Inflatable Reentry Vehicle Experiment, 2012) demonstrated a 3 m diameter in-  
1213 flatable aeroshell surviving Mach 10 reentry with peak heating of 14.4 W/cm<sup>2</sup> [Hughes et al.  
1214 \[2005\]](#). Its successor, **LOFTID** (Low-Earth Orbit Flight Test of an Inflatable Decelerator,  
1215 2022), scaled this concept to 6 m diameter and survived Mach 30 reentry, achieving TRL 8–9  
1216 for inflatable aerodynamic decelerators. These demonstrations establish the thermal protec-  
1217 tion performance of flexible fabric systems under extreme heating conditions, confirming that  
1218 multi-layer woven ceramic and polymer fabrics can provide thermal protection comparable  
1219 to rigid ablative shields at a fraction of the mass.

1220 **BEAM** (2016–present) provides the definitive deployment lesson for large pressurised  
 1221 habitats. Beyond the 25-burst recovery described above, BEAM demonstrated that pack-  
 1222 aged softgoods develop adhesion between layers during extended stowage that significantly in-  
 1223 creases deployment energy requirements [NASA Johnson Space Center \[2017\]](#). Post-deployment,  
 1224 thermal performance was “more benign than predicted” because folded softgoods create addi-  
 1225 tional insulation beyond the designed MLI performance. BEAM has now operated on ISS for  
 1226 over 8 years, providing the most extensive in-service data for any inflatable habitat. These  
 1227 deployment lessons directly inform the design of future autonomous systems: residual fold  
 1228 adhesion must be characterised and accounted for, deployment energy budgets must include  
 1229 substantial margin, and passive deployment mechanisms (sublimation, spring) may be more  
 1230 reliable than active pressurization for autonomous operations.

## 1231 6.4 Comparison with Rigid Deployable Alternatives

1232 The survey’s thesis—that inflatables offer advantages over rigid systems—requires adequate  
 1233 characterisation of the rigid deployable baseline. Three competing technology classes merit  
 1234 explicit comparison.

1235 **Composite booms** (e.g., CFRP bi-stable tape springs, Triangular Rollable and Col-  
 1236 lapsible (TRAC) booms) achieve packaging ratios exceeding 50:1 and are flight-proven at  
 1237 TRL 9 [Murphey et al. \[2015\]](#), [Banik and Murphey \[2010\]](#). The TRAC boom, used on  
 1238 LightSail-2 and the Aeroboom Innovative Mechanism (AIM), provides high deployed stiffness  
 1239 with no inflation requirement. Sickinger and Herbeck [Sickinger and Herbeck \[2004\]](#) charac-  
 1240 terised CFRP boom deployment for solar sails, demonstrating that non-inflatable composite  
 1241 booms are the dominant competing technology for CubeSat-class deployables.

1242 **Mesh reflector antennas** (e.g., Harris/L3Harris AstroMesh, 12–22 m deployed diam-  
 1243 eter, TRL 9) achieve large deployed apertures through cable-net tensioned mesh without  
 1244 requiring inflation [Santiago-Prowald and Rodrigues \[2018\]](#). These are the primary competi-  
 1245 tor to inflatable antenna concepts and represent the state of the art for deployable high-gain  
 1246 antennas.

1247 **Mechanically hinged trusses** (e.g., NASA Langley’s Compact Telescoping Array,  
 1248 CIRAS) provide high stiffness and precise geometry through articulated rigid elements, at  
 1249 the cost of higher mass and complexity compared to inflatable deployment.

1250 Table 13 presents a comparative assessment.

Table 13: Comparison of inflatable and rigid deployable technologies.

Technology	Pkg Ratio	Deployed Stiff.	Mass/m	TRL	Key Limitation
TRAC composite boom	50–100:1	High	Low	9	Length <10 m
AstroMesh reflector	10–20:1	High	Medium	9	Complex cable-net
Mech. hinged truss	3–10:1	Very high	High	9	Mass, complexity
Inflatable boom (Al-lam.)	5–10:1	Med. (post-rigid.)	Very low	8–9	Rigidisation req’d
Inflatable membrane	100–500:1	Low (press.-stab.)	Very low	7–9	Pressure maint.

1251 The inflatable approach offers its greatest advantage at the largest scales (>10 m), where  
 1252 composite boom stiffness-to-length scaling becomes unfavourable and mesh reflector cable-

1253 net complexity grows prohibitively. For CubeSat-class deployables (<3 m), TRAC booms  
1254 are the dominant technology; for medium-scale antennas (5–22 m), mesh reflectors compete  
1255 strongly. Inflatables become uniquely enabling above approximately 30 m, where no rigid  
1256 deployable alternative exists at acceptable mass.

## 1257 7 State of the Art: Actuation for Soft Space Systems

1258 The space environment imposes four principal constraints on actuator selection for soft in-  
1259 flatable systems: (1) ultrahigh vacuum eliminates ambient pressure support for unsealed  
1260 pneumatic systems; (2) extreme temperature cycling ( $-150^{\circ}\text{C}$  to  $+120^{\circ}\text{C}$  in LEO) chal-  
1261 lenges elastomers, smart materials, and ionic actuators; (3) high-energy particle and UV  
1262 radiation degrades polymers, electrodes, and electrolytes; and (4) the absence of conven-  
1263 tional lubricants eliminates standard gearing options. Against this backdrop, research has  
1264 converged on several non-pneumatic actuation principles. This section reviews six technol-  
1265 ogy families, organised from highest space-mission specificity to most novel, and presents a  
1266 comparative assessment for inflatable system integration.

### 1267 7.1 Dielectric Elastomer Actuators and DEMES

1268 Dielectric Elastomer Actuators (DEAs) convert high-voltage electrical input into mechanical  
1269 deformation of a thin elastomer membrane sandwiched between compliant electrodes. Di-  
1270 electric Elastomer Minimum Energy Structures (DEMES) extend this principle by bonding a  
1271 pre-stretched DEA membrane to a flexible frame, creating a self-deploying bending actuator  
1272 that rolls compactly for stowage [Araromi et al. \[2014, 2015\]](#).

1273 The most mission-specific DEA application is the DEMES gripper developed by Araromi et al.  
1274 for ESA’s CleanSpace One microsatellite, targeting the 820 g SwissCube CubeSat for active  
1275 debris removal [Araromi et al. \[2014\]](#). The four-arm gripper achieves the following specifica-  
1276 tions: mass less than 0.65 g per arm, tip angle change of approximately  $60^{\circ}$ , gripping force  
1277 of 0.8 mN at 5 mm deflection (up to 2.2 mN in optimised frame variants), and over 860,000  
1278 actuation cycles at 1 Hz and 2000 V without degradation. The actuator stores rolled to a  
1279 14 mm diameter cylinder and deploys by burning a retaining Nylon wire. A mechanically  
1280 elegant property emerges from the force-displacement characteristic: grip force *increases* as  
1281 the target drifts away from the actuator tip, creating a passive negative feedback loop that  
1282 enhances capture stability without active control [Araromi et al. \[2014\]](#).

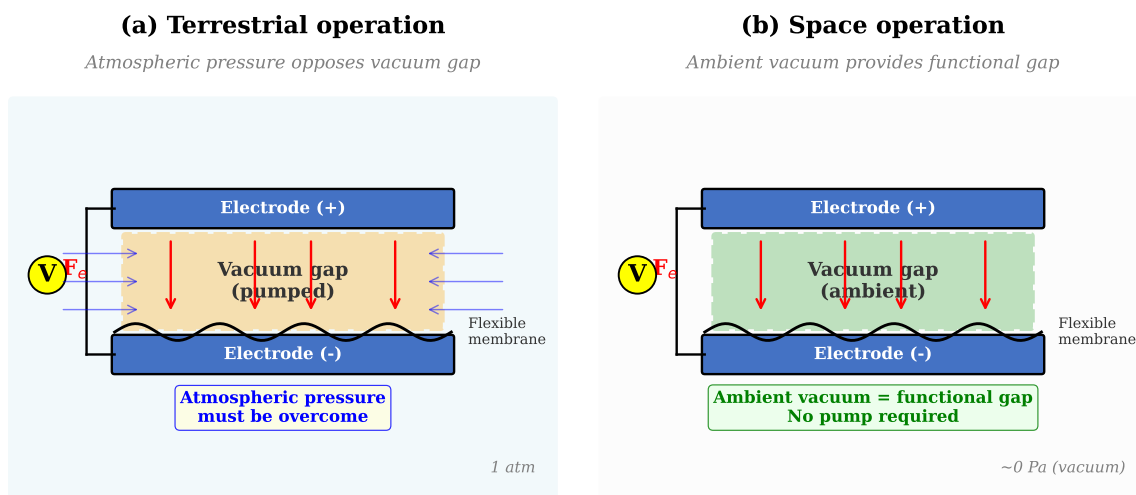
1283 Li et al. subsequently extended the 2D DEMES concept to a three-dimensional configura-  
1284 tion specifically designed for on-orbit servicing, enabling triaxial manipulation of irregularly  
1285 shaped targets [Liang et al. \[2023\]](#). The 3D configuration achieves higher load capacity and  
1286 more favorable specific force output than planar DEMES.

1287 The critical limitation of DEA/DEMES for space applications is force output: the sub-  
1288 millinewton to millinewton range, while sufficient for microgravity contact-only operations  
1289 on CubeSat-class targets, is inadequate for structural loads or capture of debris exceeding  
1290 a few kilograms. DEA membranes (PDMS, acrylic) are also vulnerable to outgassing in  
1291 vacuum and UV degradation, though neither has been systematically quantified under space  
1292 conditions—a notable gap.

## 7.2 Vacuum-Gap Electrostatic Actuators: Vacuum as Enabler

A paradigm-shifting development emerged in 2025 with Sirbu et al.’s introduction of vacuum-gap electrostatic multilayer actuators [Sirbu et al. \[2025\]](#). These devices use thin-film polymer multilayer structures enclosing vacuum gaps that zip closed upon electrical activation—a mechanism that fundamentally benefits from, rather than suffers from, the space vacuum. In terrestrial operation, the vacuum gaps must be maintained against atmospheric pressure; in space, the ambient ultrahigh vacuum ( $\sim 10^{-7}$  Pa in LEO) is the default state.

The performance specifications represent a qualitative advance over existing soft actuator technologies: actuators weighing 0.7 g deliver forces exceeding 4 N, operate at bandwidths above 100 Hz, and achieve specific power of 1.4 kW/kg [Sirbu et al. \[2025\]](#). For comparison, DEMES achieves 0.8–2.2 mN force at comparable mass—vacuum-gap actuators thus exceed DEA performance by three orders of magnitude in force at the same mass scale. The gearless, lubricant-free construction eliminates two major space reliability concerns.



*Sirbu et al. 2025: 0.7 g, >4 N force, >100 Hz bandwidth, specific power 614 W/kg*

Figure 7: Vacuum-gap electrostatic actuator operating principle (after Sirbu et al. 2025 [Sirbu et al. \[2025\]](#)). (a) In terrestrial operation, vacuum gaps between electrodes must be maintained against atmospheric pressure, requiring a vacuum pump. (b) In space, the ambient vacuum provides the functional dielectric gap directly, eliminating the pump and enabling higher bandwidth ( $>100$  Hz) at extremely low mass (0.7 g,  $>4$  N, specific power 614 W/kg).

The thin-film polymer construction of vacuum-gap actuators is structurally analogous to the multilayer membrane systems already used in inflatable habitat construction. The possibility of laminating vacuum-gap actuator layers to the inner liner of an inflatable robotic arm, combined with fibre optic shape sensors woven into the restraint webbing, suggests a pathway toward fully sensorized, actively controlled inflatable manipulators—a system architecture not yet demonstrated in the literature. The primary unresolved qualification gaps are thermal cycling ( $-150^{\circ}\text{C}$  to  $+120^{\circ}\text{C}$ ), radiation tolerance, and scale-up beyond the current laboratory-scale prototypes.

### 1314 7.3 Ionic Electroactive Polymers: Space Tolerance Assessment

1315 Ionic electroactive polymer (IEAP) actuators operate through ion migration within a polymer  
1316 membrane, producing bending deformation at low voltages (1–5 V). Punning et al. conducted  
1317 the only systematic, large-sample space environment tolerance study for this actuator class,  
1318 testing 320 samples across 7 IEAP material types under six space-relevant conditions: X-ray  
1319 irradiation (167.4 Gy), gamma irradiation (2036 Gy from  $^{60}\text{Co}$ ), UV exposure (180 hours,  
1320 xenon lamp), vacuum ( $<1$  mbar, 2 weeks), and cryogenic storage at 77 K (liquid  $\text{N}_2$ , 2 weeks)  
1321 and 4.22 K (liquid He) [Punning et al. \[2014\]](#).

1322 The results establish three design rules for space IEAP deployment:

- 1323 1. **Use ionic liquid electrolytes:** IEAP types employing ionic liquid (IL) electrolytes  
1324 (EMIBF<sub>4</sub>, EMITF, EMITFSI) showed no notable degradation under vacuum or cryo-  
1325 genic conditions. Aqueous IPMC actuators (Type A) dry out in vacuum, requiring  
1326 encapsulation for space use.
- 1327 2. **Provide UV shielding for external applications:** UV irradiation destroys PE-  
1328 DOT and PEO-based IEAP materials via photo-oxidation. This is the primary space  
1329 environment threat. Materials using carbonaceous or conducting polymer electrodes  
1330 with ionic liquid electrolytes (Types B, C, G) survived UV testing with no notable  
1331 effect.
- 1332 3. **Plan for cryogenic dormancy:** All tested IEAP types survived cryogenic stor-  
1333 age (77 K for 2 weeks, 4.22 K for 15 minutes) and recovered full functionality upon  
1334 warming—the materials cannot operate while frozen but survive and revive [Punning  
1335 et al. \[2014\]](#).

1336 A counter-intuitive finding is that X-ray radiation initially *increases* IEAP performance  
1337 through radiation-induced doping of conducting polymer electrodes, an effect that normalizes  
1338 within a few actuation cycles [Punning et al. \[2014\]](#). The force output of current IEAPs  
1339 remains in the low-millinewton range, limiting applications to sensing-adjacent tasks and  
1340 micro-manipulation.

### 1341 7.4 Tendon-Driven Continuum Manipulators

1342 Tendon-driven continuum manipulators represent the highest-force soft actuation approach  
1343 compatible with space constraints. NASA’s Tendril robot (Mehling et al., 2006) established  
1344 the heritage origin: a 1:1000 aspect-ratio inspection robot designed for confined-space inspec-  
1345 tion inside the Space Shuttle external tank [Mehling et al. \[2006\]](#). The Tendril architecture—  
1346 multiple antagonistic tendons routed along a compliant backbone—provides both the force  
1347 density and bandwidth necessary for structural manipulation tasks.

1348 Ouyang et al. proposed a hybrid rigid-continuum dual-arm space robot combining a rigid  
1349 primary arm for strength and reach with a continuum secondary arm for dexterity and com-  
1350 pliance [Ouyang et al. \[2021\]](#). The Generalized Jacobian Matrix analysis demonstrated coordi-  
1351 nated motion planning for free-floating operations, establishing the mathematical frame-  
1352 work for hybrid architectures where inflatable continuum arms complement rigid primary  
1353 manipulators.

1354 For space-compatible tendon routing, MoS<sub>2</sub> solid lubricant enables vacuum-compatible  
1355 sliding contacts, addressing the lubrication challenge that would otherwise limit tendon-  
1356 driven systems to short operational lifetimes [Ruíz et al. \[2023\]](#). The primary limitation  
1357 of tendon-driven approaches is that routing tendons over long lengths (>1 m) introduces  
1358 increasing friction and hysteresis, requiring careful mechanical design.

## 1359 7.5 Shape Memory Alloys for Deployment

1360 Shape memory alloys (SMAs), principally NiTi (Nitinol), have the highest flight TRL (8–  
1361 9) among actuator technologies applicable to soft inflatable systems, though primarily for  
1362 one-shot deployment rather than cyclic actuation. Nitinol achieves up to 10% recoverable  
1363 strain and cycle life up to 600,000 activation cycles under controlled conditions [Costanza and](#)  
1364 [Tata \[2020\]](#). Space heritage includes Mars Pathfinder deployment hinges, numerous CubeSat  
1365 solar array release mechanisms, and ESA satellite solar array root hinges [Costanza and Tata](#)  
1366 [\[2020\]](#), [Blanc et al. \[2013\]](#).

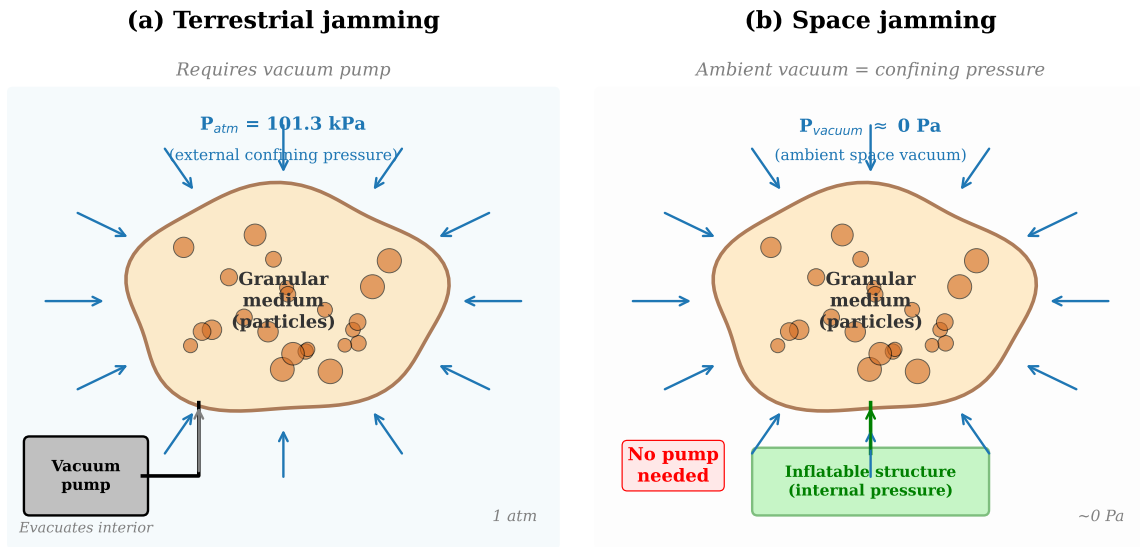
1367 For inflatable structures specifically, the critical limitation of SMA is its slow cooling  
1368 rate in the vacuum thermal environment. Without convective cooling, SMA actuators rely  
1369 on radiative heat transfer alone, limiting cyclic actuation frequency to well below 1 Hz for  
1370 typical element sizes. This effectively restricts SMA to single-deployment or low-frequency  
1371 repositioning applications in space.

1372 An emerging application combines SMA with inflatable structures: Patel et al. devel-  
1373 oped an analytical framework for SMA-based rigidisation of inflatable toroidal structures,  
1374 where NiTi wires embedded in the inflatable wall contract upon heating to lock the deployed  
1375 geometry [Rastogi et al. \[2024\]](#). This represents a potential fourth rigidisation approach be-  
1376 yond the three families established by Cadogan and Scarborough [Cadogan and Scarborough](#)  
1377 [\[2001\]](#), though it remains at the analytical stage (TRL 2–3).

## 1378 7.6 Jamming in Vacuum: A Novel Opportunity

1379 Variable stiffness by granular or layer jamming presents a counter-intuitive advantage in  
1380 the space environment that has not been previously identified in the literature. In terres-  
1381 trial soft robotics, jamming requires a dedicated vacuum pump to evacuate the jammed  
1382 medium’s enclosure, with external atmospheric pressure (~101 kPa) providing the confining  
1383 force [Fitzgerald et al. \[2020\]](#). Zhang et al. noted that jamming structures are “more likely  
1384 to be used in soft space robots because of scalability, easy fabrication, and low cost” [Zhang](#)  
1385 [et al. \[2023c\]](#), but did not explore the vacuum-specific advantage.

1386 In the space environment, this constraint inverts: the ambient vacuum of LEO (~10<sup>-7</sup> Pa)  
1387 serves as the external confining medium, while an inflatable structure’s internal pressuriza-  
1388 tion (~100 kPa) provides the pressure differential across the membrane wall. A sealed jam-  
1389 ming structure integrated into or attached to a pressurised inflatable therefore achieves stiff-  
1390 ness modulation without any vacuum pump—a simplification *unavailable* on Earth. Layer  
1391 jamming, which achieves stiffness ratios exceeding 25:1 in terrestrial systems [Fitzgerald et al.](#)  
1392 [\[2020\]](#), could be particularly well-suited for variable-stiffness robotic elements embedded in  
1393 inflatable arms.



*Stiffness transition: compliant (unjammed) to rigid (jammed) via pressure differential*

Figure 8: Jamming-in-vacuum principle for variable stiffness in space. (a) Terrestrial configuration: a vacuum pump evacuates the sealed granular membrane, and atmospheric pressure ( $\sim 101 \text{ kPa}$ ) provides the external confining force that locks the particles. (b) Space configuration: the ambient space vacuum provides external confining pressure directly; the internal pressurisation of the host inflatable structure provides the pressure differential. The vacuum pump is eliminated, and the stiffness transition from compliant to rigid is achieved passively.

1394 The primary engineering challenges are: (1) selecting space-compatible granular media  
1395 that do not outgas (candidates include hollow glass microspheres and sintered ceramic gran-  
1396 ules); (2) maintaining gas-tight seals over mission duration against micrometeoroid puncture;  
1397 and (3) characterising friction behaviour of jammed interfaces in vacuum, where the absence  
1398 of adsorbed water layers may alter surface friction coefficients. This insight represents a logi-  
1399 cal deduction from known physics and inflatable structure operating principles, and requires  
1400 experimental validation—a 5-year research priority identified in Section 13.3.

## 1401 7.7 Sealed Pneumatic Actuation in Space

1402 The opening constraint of this section—that ultrahigh vacuum eliminates ambient pressure  
1403 support for unsealed pneumatic systems—does not preclude *sealed* pneumatic actuators that  
1404 carry their own gas supply. BEAM itself is the supreme example of a sealed pneumatic  
1405 structure in space. Ataka et al. [Ataka et al. [2020]] demonstrated a closed-loop pneumatic  
1406 eversion arm with observer-based control that is directly relevant to inflatable continuum  
1407 manipulators for space inspection tasks. Eversion robots, which navigate their environment  
1408 through growth by turning inside-out [Hawkes et al. [2017]], are particularly promising for  
1409 space applications because the growth mechanism inherently manages the gas supply within  
1410 the extending structure.

1411 Sealed pneumatic actuation with onboard gas storage is viable for missions where the total  
1412 number of actuation cycles is bounded (limiting gas consumption) or where the inflatable  
1413 structure’s own pressurisation system can serve as the gas source. The mass penalty of gas  
1414 storage—approximately 0.5–2 kg per litre at 200 bar, depending on tank technology—makes  
1415 this approach less competitive for sustained cyclic actuation than electrical alternatives, but  
1416 appropriate for deployment and one-shot or low-cycle capture operations.

## 1417 7.8 Electroadhesion and Magnetic Actuation: Emerging Approaches

1418 Two additional actuation families, while not yet proposed for space inflatable systems, merit  
1419 assessment for completeness.

1420 **Electroadhesion** (electrostatic adhesion to a target surface) differs from the vacuum-gap  
1421 actuators of Section 7.2 in operating principle: Coulombic attraction to an external target  
1422 surface rather than internal gap zipping. Guo et al. [Guo et al. [2020]] demonstrated elec-  
1423 troadhesion pads integrated with soft robotic grippers for manipulation of non-cooperative  
1424 surfaces, achieving adhesion pressures of 1–5 kPa on conductive substrates. For debris cap-  
1425 ture on metallic spacecraft surfaces, electroadhesion offers a contactless-force alternative to  
1426 mechanical grasping. The primary space qualification gaps are dielectric breakdown in par-  
1427 tial vacuum (outgassing-induced), surface contamination from space debris, and radiation  
1428 degradation of the dielectric layer.

1429 **Magnetic soft actuators** with programmed 3D magnetisation profiles [Kim et al. [2018]]  
1430 represent a fundamentally different approach that avoids the vacuum and temperature limi-  
1431 tations of pneumatics and elastomers. While not yet proposed for space, magnetic actuation  
1432 in the field-free environment of orbit would require onboard field sources (permanent magnets  
1433 or electromagnets), adding mass but eliminating the outgassing and embrittlement concerns  
1434 of polymer-based actuators. This approach remains at TRL 2 for space applications.

1435 Table 14 presents a comparative assessment of the nine actuation technologies assessed  
 1436 for inflatable space systems.

Table 14: Actuator technology comparison for soft inflatable space systems.

Technology	Force	Speed	Mass	TRL (Space)	Critical Space Gap
DEA/DEMES	0.8–2.2 mN	~1 Hz	<0.65 g	3–4	UV, outgas., low force
Vacuum-gap electrost.	>4 N	>100 Hz	0.7 g	3–4	Radiation, thermal
IL-IEAP (types B,C)	Very low	Medium	Excellent	3–4	UV (shield), frozen op.
Tendon-driven	High	High	Good	5–6	Long-path friction
SMA (one-shot)	Medium	Slow	Low	8–9	Slow cooling, fatigue
Jamming (layer)	Stiffness only	Medium	Good	2–3	Unvalidated in vacuum
Sealed pneumatic	High	Medium	Mod. (gas)	4–5	Gas supply mass
Electroadhesion	1–5 kPa	Fast	Low	2–3	Surface contam., diel. brkdn
Magnetic (programmed)	Medium	Fast	Mod. (magnet)	1–2	Requires onboard field

## 1437 8 State of the Art: Sensing and Structural Health Mon- 1438 itoring

1439 Structural health monitoring (SHM) for inflatable space structures must address three simul-  
 1440 taneous requirements: detection of micrometeoroid and orbital debris (MMOD) impacts that  
 1441 may compromise pressure integrity, continuous monitoring of creep deformation in restraint  
 1442 layers under sustained pressure loading, and shape sensing for actively controlled inflatable  
 1443 manipulators. Fibre Bragg Grating (FBG) sensors have emerged as the leading technology  
 1444 platform for all three functions, with a coherent maturation pathway from rigid spacecraft  
 1445 heritage through soft actuator integration to inflatable habitat application.

### 1446 8.1 Fibre Bragg Grating Sensors: From Proba-2 to Inflatable Web- 1447 bing

1448 The FBG sensing principle—wavelength-selective reflection from a periodic refractive index  
 1449 modulation inscribed in a fibre core—enables wavelength-division multiplexing (WDM) and  
 1450 time-division multiplexing (TDM) of large sensor arrays on a single fibre strand. A single  
 1451 fibre can carry 100+ independent FBG sensors, each at a distinct Bragg wavelength, pro-  
 1452 viding distributed strain and temperature measurement with no electrical connections at  
 1453 the measurement points [Mckenzie et al. \[2021\]](#). Temperature sensitivity is approximately  
 1454 10 pm/°C in the 1500–1600 nm wavelength range.

1455 ESA’s 20+ year investment in fibre optic sensing for spacecraft culminated in the Fiber  
 1456 Sensor Demonstrator (FSD) aboard Proba-2, launched in November 2009—the first fibre  
 1457 optic sensor network demonstrated in the space environment [Mckenzie et al. \[2021\]](#). The  
 1458 FSD incorporated 12 temperature sensors, a high-temperature thruster sensor, and a xenon  
 1459 tank pressure sensor, establishing TRL 7–8 for FBG technology on rigid spacecraft platforms.

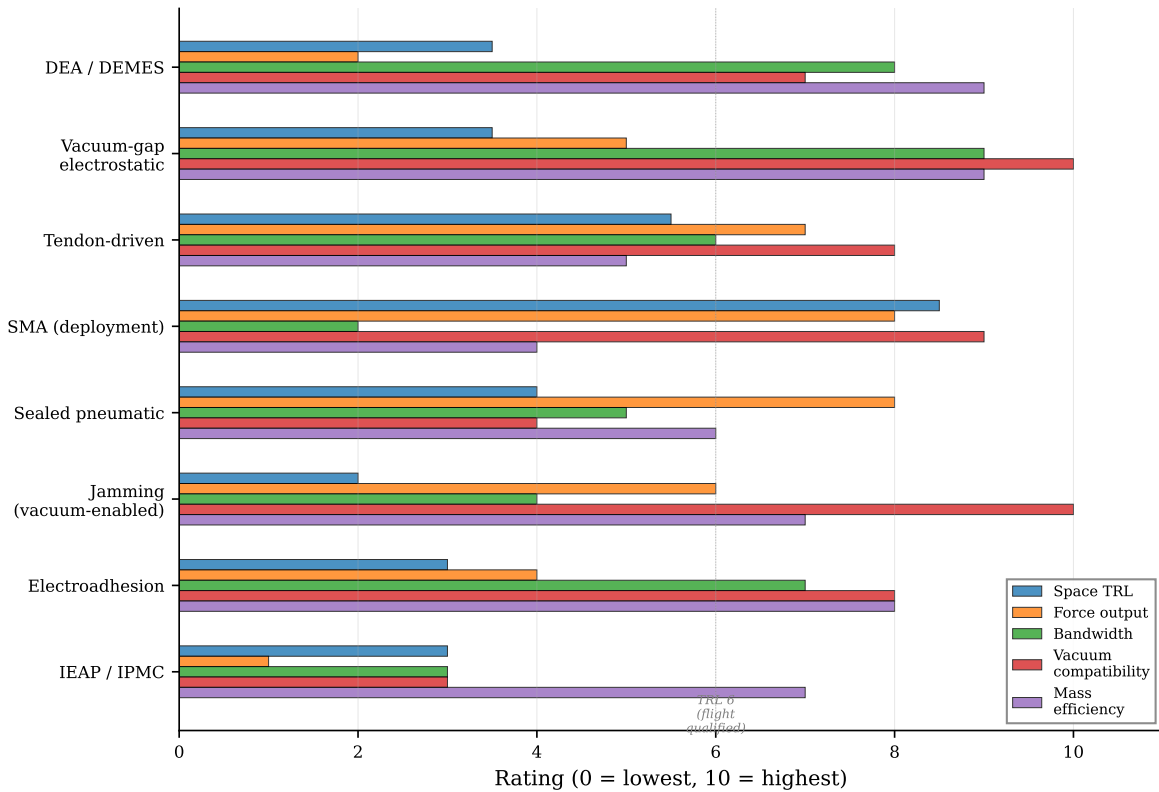


Figure 9: Comparative assessment of actuation technologies for soft inflatable space systems across five performance dimensions: space TRL, force output, bandwidth, vacuum compatibility, and mass efficiency. Ratings on a 0–10 scale reflect the combined evidence from literature reviewed in Sections 7.1–7.8. Vacuum-gap electrostatic actuators [Sirbu et al. \[2025\]](#) and jamming [Fitzgerald et al. \[2020\]](#) score highest on vacuum compatibility, reflecting the “vacuum as enabler” paradigm shift.

1460 Radiation tolerance of appropriately selected fibre types (nitrogen-doped, fluorine-doped) has  
 1461 been confirmed through ground testing, with Type II and Type III FBGs showing the highest  
 1462 radiation hardness [Girard et al. \[2022\]](#), [Baba et al. \[2025\]](#).

1463 The critical transition from rigid spacecraft to inflatable structures was demonstrated by  
 1464 Bally Ribbon Mills (BRM) and Luna Innovations under a NASA SBIR program [Bally Ribbon  
 1465 Mills and Luna Innovations \[2020\]](#). High-Definition Fibre Optic Sensing (HD-FOS) elements  
 1466 were woven directly into Vectran structural restraint webbing during the manufacturing  
 1467 process—not bonded after fabrication. Testing on 0.61 m and 2.74 m (1/3-scale) inflatable  
 1468 habitat test articles at NASA Johnson Space Center demonstrated detection of:

- 1469 • Creep deformation under sustained pressure loading
- 1470 • Internal pressure changes during inflation and operational cycling
- 1471 • Micrometeoroid impact events (confirmed via hypervelocity impact testing on inflated  
 1472 articles)

1473 The partnership included NASA, Sierra Nevada Corporation, ILC Dover, BRM, and Luna  
 1474 Innovations, targeting applications for the Lunar Gateway and Mars transit habitats [Bally  
 1475 Ribbon Mills and Luna Innovations \[2020\]](#). However, these results have been reported only  
 1476 in technical briefs and SBIR documentation, not in peer-reviewed publications—a gap that  
 1477 limits independent assessment of sensitivity metrics, minimum detectable impact size, and  
 1478 long-term reliability.

1479 The TRL assessment for FBG sensing across application domains is:

- 1480 • FBG on rigid spacecraft: TRL 7–8 (Proba-2 FSD flight heritage, 2009)
- 1481 • FBG in Vectran restraint webbing: TRL 4–5 (NASA JSC ground testing, 0.61 m and  
 1482 2.74 m articles)
- 1483 • FBG in operational inflatable habitat (flight): TRL 2–3 (not yet demonstrated)

Table 15: Sensing technology comparison for inflatable structural health monitoring.

<b>Technology</b>	<b>Accuracy</b>	<b>Channels /Fiber</b>	<b>Space Heritage</b>	<b>Demo Scale</b>	<b>TRL</b>
FBG (rigid s/c)	$\pm 10 \mu\epsilon / \pm 1^\circ\text{C}$	100+	Proba-2 (2009)	Satellite	7–8
FBG (Vectran webbing)	Creep/MMOD det.	Multiple	JSC ground	2.74 m	4–5
Multicore FOSS	0.64 mm tip	Multicore	Lab only	Actuator	3–4
DFOS (Rayleigh)	$\pm 1 \mu\epsilon$	Continuous	Lab only	m-scale	2–3
Capacitive (stretch.)	$\pm 5\%$ strain	Per-sensor	Lab only	cm-scale	2–3
Resistive (fabric)	$\pm 2\%$ strain	Per-sensor	Lab only	cm-scale	2–3
Piezoelectric (PVDF)	Impact detection	Array	Lab only	Panel	2–3

## 1484 8.2 Multicore Fibre Optic Shape Sensing

1485 For soft actuator shape sensing, Galloway et al. demonstrated the first integration of a  
1486 monolithic multicore Fibre Optic Shape Sensor (FOSS) into a fibre-reinforced soft pneumatic  
1487 actuator [Galloway et al. \[2019\]](#). The multicore fibre contains multiple sensing cores within a  
1488 single cladding, enabling three-dimensional shape reconstruction from differential curvature  
1489 measurements without requiring multiple separate fibre installations. Key results include a  
1490 mean tip position error of 0.64 mm, successful reconstruction of six distinct planar shape  
1491 profiles, and simultaneous detection of collision events, environmental shape changes, and  
1492 material stiffness variations within a single sensing modality.

1493 The field has advanced significantly since Galloway’s initial demonstration. Paloschi et al. [Paloschi](#)  
1494 [et al. \[2020\]](#) developed improved 3D shape reconstruction algorithms for multicore optical  
1495 fibres, comparing transformation matrix approaches with Frenet-Serret equations for real-  
1496 time applications and demonstrating that transformation matrix methods achieve superior  
1497 accuracy for large-curvature deformations characteristic of soft actuators. Sefati et al. [Sefati](#)  
1498 [et al. \[2021\]](#) demonstrated real-time 3D shape reconstruction using multicore FBG sensors  
1499 on continuum robot manipulators, achieving sub-millimetre accuracy relevant to the tendon-  
1500 driven continuum arms discussed in Section 7.4. These advances collectively bring multicore  
1501 FOSS from a proof-of-concept to a viable shape sensing modality for soft space manipulators,  
1502 though the interrogator hardware miniaturisation and radiation tolerance gaps remain.

1503 The multicore FOSS approach offers two advantages over distributed single-core FBG  
1504 arrays for soft structure applications. First, the monolithic construction eliminates the need  
1505 for multiple fibre routing paths through complex soft geometries. Second, the differential  
1506 curvature measurement provides inherent common-mode rejection of temperature-induced  
1507 wavelength shifts, improving strain measurement accuracy in the thermally variable space en-  
1508 vironment. The primary barriers to space qualification are the mass and power requirements  
1509 of the multicore FOSS interrogator (readout) hardware, which has not yet been miniaturized  
1510 for spacecraft integration, and the radiation tolerance of the multicore fibre itself, which has  
1511 not been characterised.

1512 For broader context, Rajan et al. [Rajan et al. \[2021\]](#) provide a comprehensive review of  
1513 FBG sensors for structural health monitoring across aerospace applications, confirming that  
1514 FBG-based SHM is the most mature fibre optic sensing technology for spacecraft structures  
1515 and identifying the key challenges for transitioning from rigid to flexible substrates.

## 1516 8.3 Capacitive, Resistive, and Alternative Soft Sensors

1517 While FBG sensors dominate the space-qualified sensing landscape, alternative soft sensing  
1518 technologies merit assessment for completeness. Zhang et al. [Zhang et al. \[2023a\]](#) devote  
1519 significant attention to stretchable capacitive sensors, resistive fabric sensors, and liquid  
1520 metal strain sensors for soft space robots. The advantages of these technologies include: no  
1521 requirement for specialised interrogator hardware (unlike FBG, which requires wavelength-  
1522 swept laser sources), simpler integration into soft structures via printing or embedding, and  
1523 lower per-sensor cost. However, for space applications, three significant limitations arise:

- 1524 • **Electromagnetic interference (EMI) sensitivity:** Capacitive and resistive sensors  
1525 operate in the electrical domain and are vulnerable to the charged particle environ-

1526 ment of LEO, solar radio bursts, and EMI from onboard electronics. FBG sensors,  
1527 operating in the optical domain, are inherently immune to EMI—a decisive advantage  
1528 for spacecraft.

- 1529 • **Radiation vulnerability:** Liquid metal sensors (e.g., eutectic gallium-indium, EGaIn)  
1530 and conductive polymer sensors have not been characterised for radiation tolerance.  
1531 Ionising radiation can alter the resistivity of conductive polymers and the wetting prop-  
1532 erties of liquid metals, degrading sensor calibration over mission-duration timescales.
- 1533 • **Multiplexing limitations:** A single optical fibre can carry 100+ independent FBG  
1534 sensors via wavelength-division multiplexing; achieving comparable channel density  
1535 with electrical sensors requires extensive wiring harnesses that add mass and failure  
1536 modes to flexible structures.

1537 For inflatable habitat applications, capacitive pressure sensors could complement FBG  
1538 strain sensors by providing direct pressure measurement at locations inaccessible to fibre  
1539 routing. For soft robotic manipulators, resistive bend sensors offer simplicity advantages for  
1540 prototype development, though FBG remains the preferred technology for flight systems.

## 1541 8.4 Distributed Fibre Optic Sensing: Rayleigh and Brillouin Scat- 1542 tering

1543 Distributed fibre optic sensing (DFOS) by Rayleigh or Brillouin scattering provides contin-  
1544 uous strain and temperature profiles along the entire fibre length, rather than at discrete  
1545 FBG grating locations. Rayleigh-based DFOS (e.g., Luna Inc. ODiSI platform) achieves  
1546 spatial resolution of approximately 0.65 mm with strain resolution better than  $\pm 1 \mu\epsilon$ , while  
1547 Brillouin-based systems provide sensing over distances up to 100 km at reduced spatial res-  
1548 olution (typically 0.5–1 m). For inflatable habitats with large membrane areas requiring  
1549 continuous monitoring (rather than point-by-point FBG interrogation), DFOS offers the  
1550 potential for comprehensive strain mapping of the entire restraint layer from a single fibre  
1551 installation.

1552 The principal barriers to space deployment of DFOS are: (i) interrogator size, mass,  
1553 and power (current laboratory DFOS systems exceed 10 kg and 50 W, compared to <2 kg  
1554 and <10 W for space-grade FBG interrogators); (ii) sensitivity to fibre bending loss, which  
1555 is exacerbated by the tight bend radii in folded inflatable structures during stowage; and  
1556 (iii) the absence of any space-environment characterisation data. DFOS is assessed at TRL 2–  
1557 3 for space inflatable applications, but its unique capability for continuous spatial coverage  
1558 makes it a high-priority development target for large-scale habitat SHM systems.

## 1559 8.5 Distributed Impact Detection

1560 The Distributed Impact Detection System (DIDS) installed on BEAM represents the highest-  
1561 TRL implementation of impact sensing for inflatable habitats. DIDS uses distributed sensors  
1562 to detect and locate MMOD impacts on the inflatable shell, providing real-time structural  
1563 integrity monitoring.

1564 Beyond the BEAM DIDS, two emerging approaches extend impact detection capabilities.  
1565 The BRM/Luna FBG-in-Vectran-webbing system described in Section 8.1 detected hyperveloc-  
1566 ity impacts during ground testing, with the woven integration providing inherent coverage  
1567 of the restraint layer structural grid [Bally Ribbon Mills and Luna Innovations \[2020\]](#). Sepa-  
1568 rately, Liao et al. demonstrated on-demand fabrication of PVDF-trFE piezoelectric sensors  
1569 via in-space manufacturing techniques, enabling the production of impact detection arrays  
1570 directly on deployed inflatable structures [White et al. \[2024\]](#). This approach could address  
1571 the challenge of instrumenting structures that are too large or complex to pre-instrument  
1572 before launch.

1573 Wei et al. proposed a complementary SHM approach based on low-frequency vibration  
1574 response characterisation of pressurised inflatable structures, where changes in modal fre-  
1575 quencies indicate structural degradation [Li et al. \[2022b\]](#). This global monitoring approach  
1576 could complement the local sensing provided by FBG arrays, together forming a hierarchical  
1577 SHM architecture: global vibration monitoring for overall structural health assessment, and  
1578 local FBG sensing for precise damage location and magnitude quantification.

1579 The pathway from current demonstrated capabilities to a flight-qualified inflatable SHM  
1580 system requires: (1) formal peer-reviewed publication of the BRM/Luna FBG-in-webbing  
1581 results with full sensitivity characterisation; (2) space qualification of FOSS interrogator  
1582 hardware (mass, power, radiation tolerance); (3) development of data fusion algorithms  
1583 combining local FBG and global vibration sensing; and (4) a flight demonstration, potentially  
1584 as an ISS external payload experiment, to bridge the TRL 4–5 to TRL 7–8 gap.

## 1585 9 State of the Art: Power Systems for Large Inflatables

1586 The integration of electrical power generation with inflatable space structures is a critical  
1587 enabling challenge for large deployable platforms. Unlike rigid spacecraft, where solar ar-  
1588 rays are mechanically decoupled from the primary structure, inflatable systems present the  
1589 possibility—and the engineering challenge—of co-locating photovoltaic generation on the de-  
1590 ployable membrane itself. This section reviews the flexible solar array landscape, the singular  
1591 attempt at inflatable-power integration (PowerSphere), and energy storage considerations for  
1592 mission architectures ranging from 100 m-class debris shields to inflatable habitats.

### 1593 9.1 Flexible Solar Array Landscape: ROSA to Perovskite

1594 The current state of the art in flexible solar arrays for space is defined by the Roll-Out Solar  
1595 Array (ROSA), which achieved TRL 9 via ISS flight demonstration in June 2017 as part  
1596 of the STP-H5 experiment [Spence et al. \[2018\]](#). The demonstration unit (5.40 m × 1.67 m)  
1597 deployed successfully using stored strain energy in carbon-fibre-reinforced polymer (CFRP)  
1598 slit-tube booms, requiring no motors. The subsequent production variant, iROSA, scaled  
1599 to 6 m × 13.7 m wings generating over 28 kW per wing at beginning of life with XTJ Prime  
1600 triple-junction cells at 30.7% efficiency. Six iROSA wings installed on the ISS between  
1601 2021 and 2023 added over 120 kW of generation capacity. At system level (blanket plus  
1602 booms, excluding spacecraft attachment hardware), ROSA achieves a specific power exceed-  
1603 ing 100 W/kg—approximately 3.7× the legacy ISS silicon rigid-panel arrays at ~27 W/kg

1604 [Spence et al. \[2018\]](#), [Yan et al. \[2025\]](#). Critically, however, ROSA’s flexible photovoltaic  
 1605 blanket is deployed on rigid composite booms; the deployment mechanism is structurally  
 1606 distinct from inflatable substrate concepts.

1607 Beyond ROSA, three deployment architectures compete for next-generation high-power  
 1608 arrays [Yan et al. \[2025\]](#): (i) Z-fold accordion panels on a central mast, representing the  
 1609 ISS legacy approach at TRL 9; (ii) fan-fold blankets on deployable masts, exemplified by  
 1610 China’s CST arrays on the Wentian laboratory module (2022), achieving approximately  $4\times$   
 1611 the specific power of rigid baselines; and (iii) roll-out arrays (ROSA/iROSA class). Mega-  
 1612 ROSA and SOLAROSA concepts target 200–500 W/kg for systems exceeding 100 kW, though  
 1613 these remain at TRL 4–5 [Yan et al. \[2025\]](#). For very large arrays approaching the kilometre  
 1614 scale (Space Solar Power Station concepts), wireless power transmission between modules  
 1615 has been identified as a necessity [Yan et al. \[2025\]](#).

1616 A paradigm shift in flexible photovoltaic technology is emerging from perovskite-based  
 1617 tandem cells. [Lang et al. \[2020\]](#) provided the critical finding that perovskite/CIGS  
 1618 (copper indium gallium selenide) tandem cells are radiation-hard, while perovskite/silicon  
 1619 heterojunction (SHJ) tandems are emphatically not. Under 68 MeV proton irradiation at a  
 1620 fluence of  $2 \times 10^{12} \text{ p}^+/\text{cm}^2$  (equivalent to over 50 years at ISS altitude), perovskite/CIGS  
 1621 tandems retained approximately 85% of initial power conversion efficiency, whereas per-  
 1622 ovskite/SHJ devices degraded catastrophically to  $\sim 1\%$  retention due to proton-induced deep  
 1623 trap states in the silicon bottom cell [Lang et al. \[2020\]](#). The perovskite top cell itself was  
 1624 essentially unaffected, with quasi-Fermi level splitting changing by only 0.004 eV. With ac-  
 1625 tive layers only  $4.38 \mu\text{m}$  thick ( $2.8 \text{ mg}/\text{cm}^2$ ), perovskite/CIGS achieves a specific power of  
 1626  $7,400 \text{ W}/\text{kg}$  at the active-layer level, or  $2,100 \text{ W}/\text{kg}$  when including a  $25 \mu\text{m}$  flexible poly-  
 1627 imide substrate [Lang et al. \[2020\]](#). More recently, [Kim et al. \[2024\]](#) demonstrated  
 1628 23.6% efficient flexible perovskite/CIGS tandems surviving 100,000 bending cycles with a  
 1629 specific power of approximately  $6,150 \text{ W}/\text{kg}$  at the cell level.

1630 These figures represent a  $10\text{--}60\times$  improvement over ROSA’s system-level specific power,  
 1631 though the comparison requires careful attention to system boundaries: cell-only figures  
 1632 exclude interconnects, encapsulant, wiring harness, and structural substrate, which collec-  
 1633 tively reduce specific power by a factor of  $3\text{--}6\times$  at the system level. Table 16 summarises  
 1634 the specific power versus TRL landscape across flexible photovoltaic technologies.

Table 16: Specific power versus TRL for flexible photovoltaic technologies for space applica-  
 tions. Cell-only and system-level figures are distinguished where data are available.

Technology	Specific Power (W/kg)	Efficiency (%)	TRL	Ref.
Legacy ISS SAW (rigid)	$\sim 27$ (system)	14	9	<a href="#">Spence et al. [20</a>
ATK UltraFlex	$\sim 150$ (system)	28–30	9	—
ROSA/iROSA	$>100$ (system)	30.7	9	<a href="#">Spence et al. [20</a>
Mega-ROSA (target)	$>200\text{--}400$	30.7	4–5	<a href="#">Yan et al. [202</a>
Perovskite/CIGS ( $25 \mu\text{m}$ sub.)	2,100 (cell+sub.)	19.2	3–4	<a href="#">Lang et al. [20</a>
Perovskite/CIGS (Kim 2024)	$\sim 6,150$ (cell)	23.6	3–4	<a href="#">Kim et al. [202</a>
PowerSphere (a-Si, measured)	$\sim 7$ (system)	10	4–5	<a href="#">Cadogan et al. [2</a>
PowerSphere (proj. w/ III-V)	$\sim 85$ (projected)	27–30	—	<a href="#">Cadogan et al. [2</a>

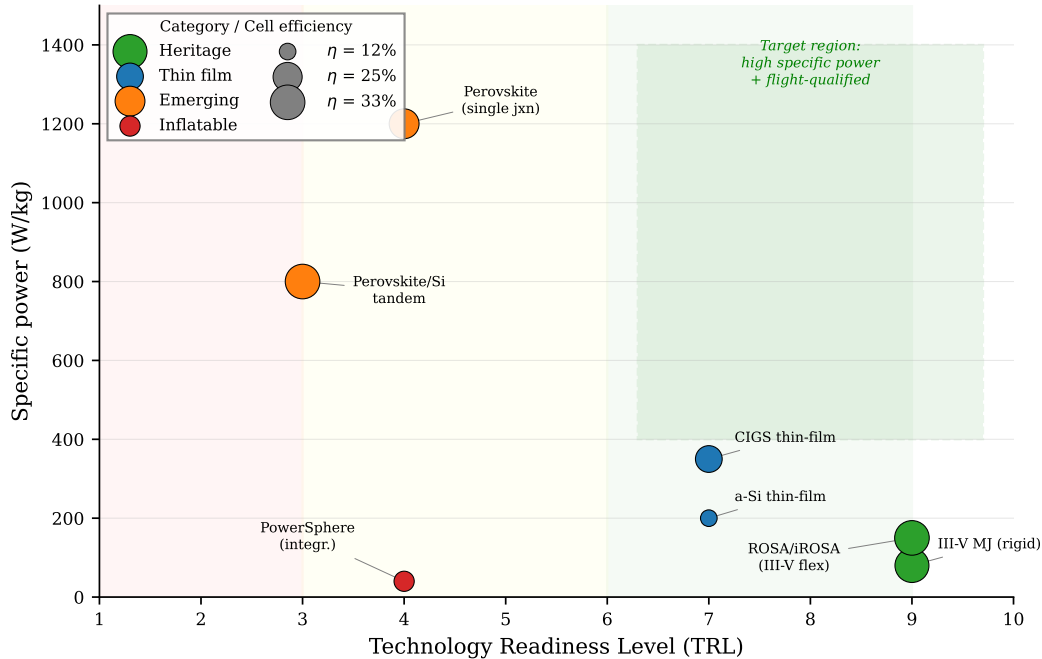


Figure 10: Specific power versus technology readiness level for flexible photovoltaic technologies relevant to inflatable space structures. Marker size indicates cell efficiency. Perovskite-based technologies Lang et al. [2020], Kim et al. [2024] offer 10–60× improvements over heritage ROSA systems Spence et al. [2018] at the cell level, but remain at TRL 3–4. The green shaded region indicates the target design space for next-generation inflatable-power integration: high specific power (>400 W/kg) at flight-qualified TRL (>6).

## 9.2 The Inflatable-Power Integration Gap: PowerSphere and Beyond

The most direct attempt to integrate thin-film photovoltaics with an inflatable deployable structure was NASA’s PowerSphere programme (2004–2009), led by ILC Dover (structure), NASA Glenn Research Center (cells), and Sandia National Laboratories (interconnects) Cadogan et al. [2003], Scheiman et al. [2005]. The PowerSphere Engineering Development Unit was a 0.6 m diameter UV-rigidisable inflatable geodesic sphere clad with thin-film amorphous silicon (a-Si) solar cells on a polyimide substrate. The complete system comprised a 1 kg PowerSphere subsystem mounted on a 3 kg bus, with 15 cells per hemisphere (9 hexagonal, 6 pentagonal) connected via copper wrap-around flex-circuit interconnects that could survive folding during stowage without cracking Cadogan et al. [2003], Scheiman et al. [2005].

The UV-rigidisation mechanism is particularly significant for the survey’s themes. Thirty hinges per sphere used S-glass fibre reinforced with ATI-P600-2 UV-curing epoxy (glass transition temperature  $T_g = 211\text{ }^\circ\text{C}$ ), encapsulated in UV-transparent 1-mil Mylar film. Upon exposure to solar UV radiation ( $\lambda < 385\text{ nm}$ ) for 10–45 minutes post-deployment, the resin polymerised, converting the inflatable into a self-supporting rigid structure and eliminating the requirement for long-term inflation gas retention Cadogan et al. [2003]. Inflation was

1652 achieved passively through vapour pressure from sublimation powder at approximately 1 psi  
1653 ( $\sim 6.9$  kPa).

1654 Thermal cycling tests ( $-120^\circ\text{C}$  to  $+80^\circ\text{C}$ , 1000 cycles per NASA specification) demon-  
1655 strated cell and interconnect survival with less than 2% power degradation, although one  
1656 of four interconnect coupons failed, prompting the addition of a titanium binder layer as a  
1657 design modification. Cell interconnect technology was partially validated on the MISSE-5  
1658 experiment aboard the ISS [Cadogan et al. \[2003\]](#). At 10% a-Si cell efficiency, the 0.6 m  
1659 prototype generated approximately 29 W at design point, yielding a system specific power  
1660 of  $\sim 7.25$  W/kg. With projected III-V triple-junction cells at 27–30% efficiency, the concept  
1661 was estimated to reach  $\sim 85$  W/kg.

1662 The PowerSphere programme reached TRL 4–5 but never flew. Planned missions—the  
1663 PowerSphere Flight Experiment and PSIREX (Pico Satellite Inflatable Reflector Experiment)—  
1664 were not implemented, and the programme appears inactive since the final publication by  
1665 Jenkins in 2009 on thermal cycling results [Jenkins et al. \[2009\]](#). No successor programme inte-  
1666 grating thin-film photovoltaics with inflatable structure deployment has been identified. This  
1667 represents a critical gap: ROSA (TRL 9) demonstrates that flexible photovoltaic blankets  
1668 function reliably in space, and PowerSphere (TRL 4–5) demonstrated that cells can survive  
1669 fold/deploy on an inflatable substrate, but nobody is currently pursuing inflatable-integrated  
1670 photovoltaics. A revival of the PowerSphere concept using modern perovskite/CIGS cells—  
1671 which offer 200–300 $\times$  higher specific power than the original a-Si cells and validated radiation  
1672 hardness [Lang et al. \[2020\]](#)—represents a logical and compelling research direction.

### 1673 **9.3 Energy Storage: Li-ion, RFC, and Mission-Dependent Selection**

1674 Energy storage for large inflatable structures follows established space heritage, with tech-  
1675 nology selection driven primarily by eclipse duration and mission architecture. The current  
1676 standard is lithium-ion, with state-of-the-art cell-level specific energy of 200–300 Wh/kg  
1677 and system-level (including battery management, thermal control, and structure) of 100–  
1678 160 Wh/kg [Sharma and Santasalo-Aarnio \[2025\]](#). The ISS lithium-ion upgrade programme  
1679 (2017–2021), replacing nickel-hydrogen (Ni-H<sub>2</sub>) with 24 lithium-ion Orbital Replacement  
1680 Units (ORUs) at 4 kWh each, provides direct heritage for large-structure lithium-ion energy  
1681 storage.

1682 For a 100 m-class inflatable debris shield in LEO (90-minute orbit, 36-minute eclipse),  
1683 the power demand is driven by supporting subsystems rather than the passive membrane  
1684 itself. Station-keeping via electric propulsion dominates at 1–50 kW depending on orbit and  
1685 attitude strategy (Section 11.3); attitude control, telemetry, and sensors add 1–7 kW. A total  
1686 system power demand in the range of 2–50 kW is appropriate, requiring 4–40 kWh of eclipse  
1687 energy storage—translating to 25–250 kg of lithium-ion battery mass at 160 Wh/kg system  
1688 level. This is a non-trivial but manageable fraction of the estimated 5,000 kg total system  
1689 mass.

1690 For missions requiring extended eclipse storage—notably lunar surface operations (354-  
1691 hour lunar night) or deep-space transit—regenerative fuel cells (RFCs) offer 400–1,000 Wh/kg  
1692 at system level but remain at TRL 5–6 for space applications [Sharma and Santasalo-Aarnio](#)  
1693 [\[2025\]](#). Supercapacitors (5–15 Wh/kg) are poorly suited for eclipse energy storage but may  
1694 serve pulsed-load applications such as electric propulsion ignition or deployment actuators.

1695 Table 17 summarises the energy storage technology comparison.

Table 17: Energy storage technologies for large inflatable space structures.

Technology	Sp. Energy (Wh/kg)	Cycle Life	TRL	Best Use Case
Li-ion (cell)	200–300	>30,000	9	LEO eclipse storage
Li-ion (system)	100–160	>30,000	9	LEO eclipse storage
Ni-H <sub>2</sub> (legacy)	30–60	>40,000	9	Heritage only
RFC (H <sub>2</sub> /O <sub>2</sub> )	400–1,000	—	5–6	Lunar night, deep space
Supercapacitor	5–15	>500,000	7	Pulsed loads
RTG	N/A	—	9	No-sun environments

## 1696 10 State of the Art: Thermal Management

1697 Thermal management for inflatable space structures presents unique challenges that stem  
 1698 from the fundamental nature of the structural material: thin fabric membranes offer minimal  
 1699 thermal mass, poor through-thickness conductivity, and large surface area-to-volume ratios.  
 1700 These characteristics amplify the orbital thermal cycling environment and demand thermal  
 1701 control approaches that are compatible with the fold/deploy lifecycle, vacuum exposure, and  
 1702 the mechanical flexibility of the host structure. This section reviews established approaches  
 1703 (multi-layer insulation, loop heat pipes), the JWST sunshield as a large-area deployable  
 1704 thermal barrier precedent, and emerging technologies (variable emissivity coatings, phase  
 1705 change materials) that offer particular promise for inflatable applications.

### 1706 10.1 Multi-Layer Insulation for Inflatable Shells

1707 Multi-layer insulation (MLI) is the primary passive thermal control technology for spacecraft  
 1708 and achieves effective emittance  $\varepsilon_{\text{eff}} = 0.005\text{--}0.05$  for 10–40 layer blankets [Gilmore \[2002\]](#),  
 1709 [Finckenor and Dooling \[1999\]](#). For conventional rigid spacecraft, MLI is draped over external  
 1710 surfaces with controlled layer separation maintained by low-conductance spacers (typically  
 1711 Dacron netting). For inflatable structures, MLI integration is more complex: the insulation  
 1712 must survive folding, accommodate deployment kinematics, and maintain layer separation  
 1713 without rigid structural support.

1714 The TransHab/BEAM heritage shell architecture represents the current standard for  
 1715 inflatable habitat thermal design [Kennedy \[2002\]](#), [Valle et al. \[2019a\]](#). In this architecture,  
 1716 MLI forms the outermost thermal protection sub-assembly of a five-layer softgoods stack,  
 1717 ordered (outer to inner) as: (1) BETA cloth exterior for atomic oxygen protection; (2) nylon-  
 1718 reinforced double-aluminised Mylar/Kapton MLI layers with perforated inner surfaces for  
 1719 venting during deployment; (3) Nextel/Kevlar stuffed-Whipple MMOD shield; (4) Vectran  
 1720 restraint layer carrying hoop and axial pressure loads; and (5) multi-redundant gas-tight  
 1721 bladder. The MLI sub-assembly in TransHab comprised over 20 individual reflector layers  
 1722 with effective emittance on the order of 0.015–0.05 [Finckenor and Dooling \[1999\]](#).

1723 BEAM’s on-orbit thermal performance has been characterised as “more benign than  
 1724 predicted” [NASA Johnson Space Center \[2017\]](#), an observation attributed to the additional  
 1725 insulation provided by folded softgoods layers that act as low-conductance barriers even  
 1726 when not specifically designed as MLI. This finding has positive implications for inflatable  
 1727 structure design: the inherent multi-layer nature of the fabric wall stack provides a degree  
 1728 of passive thermal buffering beyond that of the dedicated MLI layers alone.

## 1729 10.2 The JWST Sunshield as Deployable Thermal Barrier Prece- 1730 dent

1731 The James Webb Space Telescope (JWST) sunshield is the largest deployed thermal barrier  
 1732 ever flown and provides the benchmark for what large-area passive thermal isolation can  
 1733 achieve [Arenberg et al. \[2016\]](#). At 21.2 m × 14.2 m (approximately 300 m<sup>2</sup>), the kite-shaped  
 1734 sunshield comprises five layers of Kapton E polyimide membrane: Layer 1 (sun-facing) at  
 1735 50 μm thickness, Layers 2–5 at 25 μm. All layers are coated with 100 nm aluminium on both  
 1736 sides for reflectivity; Layers 1 and 2 additionally carry 50 nm doped silicon on the sun-facing  
 1737 surface for enhanced emissivity and electrostatic discharge grounding.

1738 The thermal performance is extraordinary: the sun-facing side of Layer 1 reaches approx-  
 1739 imately +110 °C while the telescope-facing side of Layer 5 operates at −233 °C—a gradient  
 1740 of 343 °C across five layers. Incoming solar power of approximately 200–250 kW is attenu-  
 1741 ated to ~23 mW transmitted to the cold side, an attenuation ratio of approximately 10<sup>6</sup>:1  
 1742 [Arenberg et al. \[2016\]](#). This performance is achieved through the V-groove geometry: angled  
 1743 layers radiate inter-layer thermal energy sideways to deep space through the vacuum gaps  
 1744 between membranes.

1745 However, the JWST sunshield is not an inflatable structure. Layer separation is main-  
 1746 tained by six rigid spreader bars, with centre gaps of ~25–50 mm expanding to ~250 mm  
 1747 at the edges. The deployment system required 139 of JWST’s 178 release mechanisms, 400  
 1748 pulleys, 90 cables (~0.5 km total), 8 motors, and 70 hinges [Arenberg et al. \[2016\]](#). Table 18  
 1749 compares the JWST sunshield and TransHab shell architectures.

Table 18: JWST sunshield versus TransHab inflatable shell comparison.

Feature	JWST Sunshield	TransHab Shell
Primary function	Thermal isolation	Structural + MMOD + thermal
Layer count	5 membranes	5 sub-assemblies (60+ layers)
Layer material	Kapton E (all 5)	Vectran, Kevlar, Nextel, Mylar
Structural role	None (spreader bars)	Vectran restraint carries pressure
Energy attenuation	10 <sup>6</sup> :1	~150 °C gradient
Deployment	139 mechanisms, 8 motors	Inflation pressure
Deployed area	300 m <sup>2</sup>	220 m <sup>2</sup> (cylinder)

1750 It should be noted that JWST operates at the Sun-Earth L2 point, not in LEO—the  
 1751 thermal environment is fundamentally different (no orbital cycling, no atmospheric drag, no  
 1752 atomic oxygen), and this limits the direct applicability of JWST thermal performance num-

1753 bers to LEO inflatable structures. Nevertheless, for inflatable debris shields or large-area  
1754 thermal barriers, the JWST heritage demonstrates that multi-layer Kapton stacks achieve  
1755 extreme thermal gradients at 20+ metre scales. Adapting this concept to a fully inflat-  
1756 able deployment mechanism—replacing rigid spreader bars with inflation-maintained layer  
1757 separation—remains an open engineering challenge. A hybrid approach combining inflatable  
1758 outer layers with rigid-bar-maintained inner separation represents a plausible intermediate  
1759 architecture.

### 1760 10.3 Variable Emissivity Coatings and Smart Radiators

1761 Variable emissivity materials (VEMs) offer “electronic louver” functionality for dynamic ther-  
1762 mal regulation without mechanical moving parts—a capability uniquely suited to large inflat-  
1763 able surfaces where conventional mechanical louvers are impractical due to mass, complexity,  
1764 and incompatibility with membrane substrates. Two technology families have received sus-  
1765 tained development: passive thermochromic coatings and active electrochromic devices.

1766 Among passive thermochromic approaches, vanadium dioxide ( $\text{VO}_2$ ) based coatings are  
1767 technically most advanced. Kim et al. [Kim et al. \[2019\]](#) performed the first direct calorimetric  
1768 measurement of a  $\text{VO}_2$ -based switchable radiator in a simulated space environment (vacuum  
1769  $10^{-7}$  Torr, cold block at 108 K). Their multilayer structure—Si substrate /  $\text{VO}_2$  (40–100 nm)  
1770 /  $\text{BaF}_2$  dielectric spacer (1,500 nm) / Au back reflector (200 nm)—operates as a Fabry-Pérot  
1771 resonant absorber. In the low-temperature insulating state ( $T < 340$  K), hemispherical  
1772 emissivity is  $\varepsilon_L = 0.16$ ; above the phase transition ( $T > 340$  K, metallic  $\text{VO}_2$ ),  $\varepsilon_H = 0.51$ ,  
1773 yielding  $\Delta\varepsilon = 0.35$ . The practical consequence is a net radiated power difference of  $480 \text{ W/m}^2$   
1774 between 300 K and 373 K—a factor of  $7\times$  in radiative cooling capacity [Kim et al. \[2019\]](#).  
1775 The silicon substrate provides an incidental benefit: protection of the  $\text{VO}_2$  film from atomic  
1776 oxygen erosion, addressing a known degradation mechanism. An earlier design by Hendaoui  
1777 et al. [Hendaoui et al. \[2013\]](#) achieved a higher normal emissivity swing of  $\Delta\varepsilon = 0.49$  but  
1778 without the atomic oxygen protection.

1779 The sole flight-demonstrated variable emissivity technology is the EclipseVED<sup>TM</sup> elec-  
1780 trochromic coating (Ashwin-Ushas Corporation), flown on the MidSTAR-1 satellite in 2007,  
1781 achieving TRL 7–8. EclipseVED operates by applying a low voltage (1–3 V) to an elec-  
1782 trochromic polymer film, switching emissivity across the range  $\varepsilon \approx 0.19$ – $0.90$  in the 8– $12 \mu\text{m}$   
1783 thermal infrared band. It requires no mechanical actuators, making it compatible with large-  
1784 area application including inflatable surfaces. The principal limitation is the requirement for  
1785 a thin-film conductor and electrical interconnects across the deployed area—a tractable but  
1786 non-trivial integration challenge for inflatable structures.

1787 Table 19 compares variable emissivity technologies.

1788 For the survey’s inflatable structures context, VEMs offer a path to autonomous ther-  
1789 mal self-regulation: at high temperature (sunlit, electronics active), emissivity increases to  
1790 reject heat; at low temperature (eclipse), emissivity decreases to conserve heat. This self-  
1791 regulating behaviour eliminates active heaters in many scenarios, reducing power demand  
1792 on power-constrained large inflatable platforms. The principal barrier to inflatable applica-  
1793 tion is substrate compatibility:  $\text{VO}_2$  coatings currently require rigid silicon substrates, while  
1794 EclipseVED has been demonstrated only on rigid aluminium panels. Developing these tech-  
1795 nologies on flexible polymer substrates (Kapton, polyimide) is a near-term research priority.

Table 19: Variable emissivity coating technologies for spacecraft thermal control.

Technology	$\Delta\varepsilon$	$T_{\text{switch}}$	Power	TRL	Flight Heritage
VO <sub>2</sub> (Kim 2019)	0.35 (hemi.)	67°C	Zero	3–4	None
VO <sub>2</sub> (Hendaoui 2013)	0.49 (normal)	67°C	Zero	3	None
EclipseVED (electrochromic)	~0.71	Voltage ctrl	1–3 V	7–8	MidSTAR-1 (2007)
MEMS louvers	~0.8 (eff.)	Bimetal	Zero	7–8	Multiple

## 10.4 Loop Heat Pipes for Deployed Structures

Loop heat pipes (LHPs) are the preferred heat transport technology for active thermal systems in space, offering passive capillary-driven two-phase fluid transport with zero pump power, distances up to several tens of metres, and heat loads up to 5+ kW per evaporator [Maydanik \[2005\]](#). The capillary driving force is generated by a sintered porous wick confined to a compact evaporator body; vapour and liquid travel in separate smooth-wall transport lines. A compensation chamber at the evaporator provides thermal buffering and enables active setpoint control to  $\pm 0.5^\circ\text{C}$  via low-power heaters (1–5 W). Working fluids for space include ammonia ( $-40$  to  $+70^\circ\text{C}$ , the standard), propylene ( $-60$  to  $+50^\circ\text{C}$ , when ammonia freeze risk exists), and ethane ( $-100$  to  $+30^\circ\text{C}$ ) for cryogenic applications.

LHP spaceflight heritage extends over 35 years, beginning with the Granat astrophysics satellite in 1989 and encompassing over 30 systems flown by 2005 across Russian, American, and European programmes [Maydanik \[2005\]](#). The Hughes HS-702 communications satellite (1999) demonstrated the first LHP-coupled deployable radiator—the directly relevant precedent for inflatable structures, as the LHP flexible transport lines accommodated the mechanical hinge between the deployed radiator panel and the spacecraft bus. NASA’s EOS Terra and Aqua missions, ICESat/GLAS, and Swift/BAT all employed LHP thermal control.

For inflatable habitats, LHPs are the natural technology for transporting waste heat from interior systems (avionics, crew metabolic load) to external deployable radiators. The flexible transport lines can be routed through deployment hinges and accommodate the geometric changes between stowed and deployed configurations. Current single-evaporator LHP systems transport 50–700 W in typical spacecraft configurations, with multi-loop architectures providing aggregate capacities exceeding 10 kW for large platforms. The principal engineering challenge for inflatable integration is the condenser interface: bonding or mechanically attaching the condenser panel to the flexible membrane requires a solution to the rigid-to-flexible interface problem discussed in Section [12.3](#).

## 10.5 Phase Change Materials in Fabric Layers: The TRL 2–3 Gap

Phase change materials (PCMs) offer passive thermal buffering by absorbing and releasing latent heat during orbital day/night transitions. For LEO inflatable habitats experiencing 90-minute thermal cycles, the most promising PCM candidates are n-eicosane (melting point  $36.4^\circ\text{C}$ , latent heat 247–253 J/g) and n-octadecane ( $28.2^\circ\text{C}$ , 244 J/g) [Diaconu et al. \[2023\]](#). PCM-based thermal control for rigid electronics enclosures has extensive spaceflight heritage spanning from Apollo Lunar Roving Vehicle battery management (1971) through Mars

1829 rovers (Spirit, Opportunity, Curiosity, Perseverance; TRL 9) and ISS experiments (TRL 5–6)  
1830 [Diaconu et al. \[2023\]](#).

1831 However, integration of PCMs into flexible fabric layers for inflatable structures—the  
1832 configuration needed to provide distributed thermal buffering across large membrane areas—  
1833 remains at TRL 2–3. Five specific technical barriers have been identified:

- 1834 1. **Microgravity containment:** Liquid-phase PCM migrates freely in zero-g. Microen-  
1835 capsulation (1–100  $\mu\text{m}$  capsules) addresses this at small scale, but capsule integrity  
1836 during the fold/deploy lifecycle has not been tested for space-grade materials.
- 1837 2. **Fold/deploy cycling:** PCM-loaded fabric must survive hundreds to thousands of  
1838 fold/deploy cycles without capsule rupture—a requirement with no demonstrated so-  
1839 lution in the space-qualified materials literature.
- 1840 3. **Outgassing:** PCM solvents and vapour can contaminate optical surfaces (solar cells,  
1841 sensors). Space-qualified encapsulation that meets ASTM E595 outgassing require-  
1842 ments has not been characterised for PCM-textile systems.
- 1843 4. **Thermal conductivity:** Raw paraffin PCMs have thermal conductivity  $k \approx 0.2 \text{ W}/(\text{m}\cdot\text{K})$ —  
1844 approximately  $1,000\times$  lower than aluminium—resulting in slow thermal response. Car-  
1845 bon nanotube or graphene additives can improve conductivity to 1–5  $\text{W}/(\text{m}\cdot\text{K})$  but at  
1846 the cost of reduced fabric flexibility and increased mass.
- 1847 5. **Atomic oxygen interaction:** PCM capsule shells (typically PMMA or gelatin) may  
1848 erode under atomic oxygen flux in LEO, releasing PCM material and contaminating  
1849 the local environment.

1850 Despite these barriers, the potential benefit is substantial. A  $1 \text{ kg}/\text{m}^2$  layer of microencap-  
1851 sulated n-eicosane would provide  $\sim 250 \text{ J}/\text{g} \times 1,000 \text{ g}/\text{m}^2 = 250 \text{ kJ}/\text{m}^2$  of thermal storage—  
1852 sufficient to buffer the first  $\sim 10$  minutes of eclipse entry for a membrane with low thermal  
1853 mass, significantly reducing peak-to-trough temperature excursions. The technology needs  
1854 a structured development programme analogous to what IRVE provided for flexible thermal  
1855 protection systems.

## 1856 11 State of the Art: Attitude and Orbit Control

1857 Attitude and orbit control for large inflatable space structures is dominated by a single over-  
1858 arching challenge: control-structure interaction (CSI). When structural flexibility approaches  
1859 or overlaps the attitude control bandwidth, conventional rigid-body AOCS designs become  
1860 inadequate or unstable. For 100 m-class inflatable structures, where the lowest natural fre-  
1861 quencies may fall well below 0.1 Hz, CSI is not merely a complication—it is the central design  
1862 driver. This section reviews the CSI challenge, the theoretical framework of gyroelastic body  
1863 dynamics, the drag budget for large LEO structures, and the critical gap in AOCS theory  
1864 for pressure-stabilised membranes.

## 11.1 Control-Structure Interaction for Flexible Spacecraft

CSI has been studied since the 1970s in the context of large space systems including the Solar Power Satellite concept, the Space Station, and large deployable antennas. For mechanically stiff structures—rigid trusses, mesh antennas, deployable solar arrays—the lowest structural modes typically fall in the 0.1–1 Hz range for 10–30 m scale structures, and structural damping ratios  $\zeta \approx 0.001$ –0.005 are small but predictable [Nicassio et al. \[2022\]](#). The standard approach is modal truncation and notch filtering: identify the structural modes, exclude them from the control bandwidth, and ensure adequate frequency separation between rigid-body and flexible modes.

For inflatable (pressure-stabilised) structures, the CSI problem is qualitatively different in four respects. First, structural stiffness is primarily provided by membrane tension arising from internal pressure ( $\sigma_{\text{hoop}} = pR/t$  for a cylindrical geometry) rather than material bending stiffness, and this stiffness changes if pressure is lost due to microleaks or thermal cycling. Second, the lowest natural frequencies scale inversely with structure size and can be  $\ll 0.1$  Hz for 100 m-class structures, potentially falling within the AOCS bandwidth. Third, membranes cannot carry compressive stress—they wrinkle, creating local zones of nonlinear stiffness that invalidate linear modal analysis. Fourth, actuator forces transmitted through a flexible membrane diffuse spatially rather than transmitting cleanly through a rigid structural path, degrading actuator-to-mode coupling. No paper in the published literature explicitly addresses AOCS for pressure-stabilised inflatable structures at the 100 m scale.

Angeletti et al. [Nicassio et al. \[2022\]](#) developed a “minimum complexity” hybrid ODE-PDE model for large flexible spacecraft that provides a useful methodological template: the rigid bus is treated as an ODE system (6 DOF) coupled to the flexible structure as a PDE system (beam/plate). Even a 2-mode truncation captured over 80% of the relevant dynamics for control design. However, this framework assumes conventional bending stiffness and is not directly applicable to pressure-stabilised membranes.

## 11.2 Gyroelastic Body Theory and Distributed Momentum Management

The theoretical foundation for distributed attitude actuators on flexible structures was established by D’Eleuterio and Hughes in a series of foundational papers [D’Eleuterio and Hughes \[1984, 1986, 1987\]](#). The 1984 paper introduced the concept of *gyricity*—the distribution of angular momentum per unit volume embedded within an elastic continuum. The governing equations couple elastic deformation to rigid-body rotation through the gyricity distribution  $\mathbf{g}(\mathbf{x})$ , showing that distributed angular momentum fundamentally modifies elastic wave propagation and natural frequencies. The key theoretical finding is that gyroelastic systems have complex eigenvalues (gyroelastic frequency splitting), providing passive damping-like behaviour without explicit energy dissipation—analogueous to Zeeman splitting in quantum mechanics [D’Eleuterio and Hughes \[1984\]](#). The 1986 companion paper [D’Eleuterio and Hughes \[1986\]](#) derived the modal parameters (complex mode shapes, orthogonality conditions, participation factors) needed for practical numerical analysis, while the 1987 paper [D’Eleuterio and Hughes \[1987\]](#) extended the framework to complete spacecraft systems, treating a vehicle with distributed angular momentum storage as a unified gyroelastic body.

1907 Damaren and D’Eleuterio [Damaren and D’Eleuterio \[1989\]](#) solved the optimal gyricity  
 1908 distribution problem using calculus of variations: the spatial distribution  $\mathbf{g}^*(\mathbf{x})$  that min-  
 1909 imises a quadratic performance index concentrates angular momentum where modal kinetic  
 1910 energy is highest—at the antinodes of the dominant vibration modes. This is directly analo-  
 1911 gous to collocating sensors at modal antinodes and provides the theoretical basis for actuator  
 1912 placement optimisation on large flexible structures.

1913 The most recent quantitative validation of distributed momentum management was pro-  
 1914 vided by Cachim et al. [Cachim et al. \[2024\]](#), who compared centralized (6 large reaction  
 1915 wheels on the bus) versus distributed (33 small reaction wheels throughout the structure)  
 1916 attitude control for a  $\sim 30$  m hexagonal plate-like structure (4,200 kg,  $J_{xx} = 2.2 \times 10^5$  kg·m<sup>2</sup>).  
 1917 Using LQG control with 25 retained modes below 80 Hz, the distributed configuration  
 1918 achieved  $3.3\times$  faster settling (30 s versus 100 s),  $7\times$  less structural deformation ( $0.33 \mu\text{m}$   
 1919 versus  $2.3 \mu\text{m}$ ) during a  $0.5^\circ$  slew, and improved fine pointing (RMS error 0.038 versus  
 1920 0.068 arcsec), at the cost of approximately  $2\times$  more total torque [Cachim et al. \[2024\]](#). The  
 1921 structure was modelled as a Kirchhoff plate (bending-only, shear neglected), which is valid  
 1922 for thin plates with thickness-to-span ratio  $>1:30$  but is not applicable to pressure-stabilised  
 1923 membranes.

### 1924 11.3 Drag Budget for 100 m-Class LEO Structures

1925 A 100 m-class inflatable structure in LEO faces a severe drag penalty due to its extreme area-  
 1926 to-mass ratio. At 500 km altitude, atmospheric density varies from  $\rho \approx 5 \times 10^{-13}$  kg/m<sup>3</sup> (solar  
 1927 minimum) to  $\rho \approx 3 \times 10^{-12}$  kg/m<sup>3</sup> (solar maximum)—a factor of  $6\times$  variation driven by solar  
 1928 EUV heating of the upper atmosphere [Jiang et al. \[2022\]](#), [Andreussi et al. \[2022\]](#). For a 100 m  
 1929 diameter circular membrane presented broadside to the velocity vector ( $A_{\text{eff}} \approx 7,850$  m<sup>2</sup>), the  
 1930 drag force  $F_D = \frac{1}{2}\rho v^2 C_D A$  yields the estimates in Table 20.

Table 20: Drag force estimates for a 100 m inflatable structure at 500 km altitude.  $C_D \approx 2.4$ –  
 3.2 for flat membrane in free molecular flow with atomic oxygen accommodation.

Scenario	$\rho$ (kg/m <sup>3</sup> )	$A_{\text{eff}}$ (m <sup>2</sup> )	$C_D$	$F_D$ (N)
Solar min, edge-on	$5 \times 10^{-13}$	100	2.4	0.007
Solar min, broadside	$5 \times 10^{-13}$	5,000	2.4	0.35
Solar min, broadside (max)	$5 \times 10^{-13}$	7,850	3.2	0.72
Solar max, broadside	$3 \times 10^{-12}$	5,000	3.2	14
Solar max, broadside (max)	$3 \times 10^{-12}$	7,850	3.2	21

1931 The drag coefficient range of  $C_D = 2.4$ – $3.2$  for a flat membrane in free molecular flow is  
 1932 based on the standard models of Sentman [Sentman \[1961\]](#) and Moe and Moe [Moe and Moe \[2005\]](#),  
 1933 where the upper bound corresponds to complete diffuse reflection with full thermal  
 1934 accommodation on atomic oxygen surfaces.

1935 The area-to-mass ratio is the fundamental problem: if the 100 m structure totals 5,000 kg,  
 1936  $A/m \approx 1.6$  m<sup>2</sup>/kg (broadside), compared to  $\sim 0.02$  m<sup>2</sup>/kg for the ISS—approximately  $80\times$   
 1937 higher. Using the ballistic coefficient  $\beta = m/(C_D A)$ , the orbital decay time at 500 km during

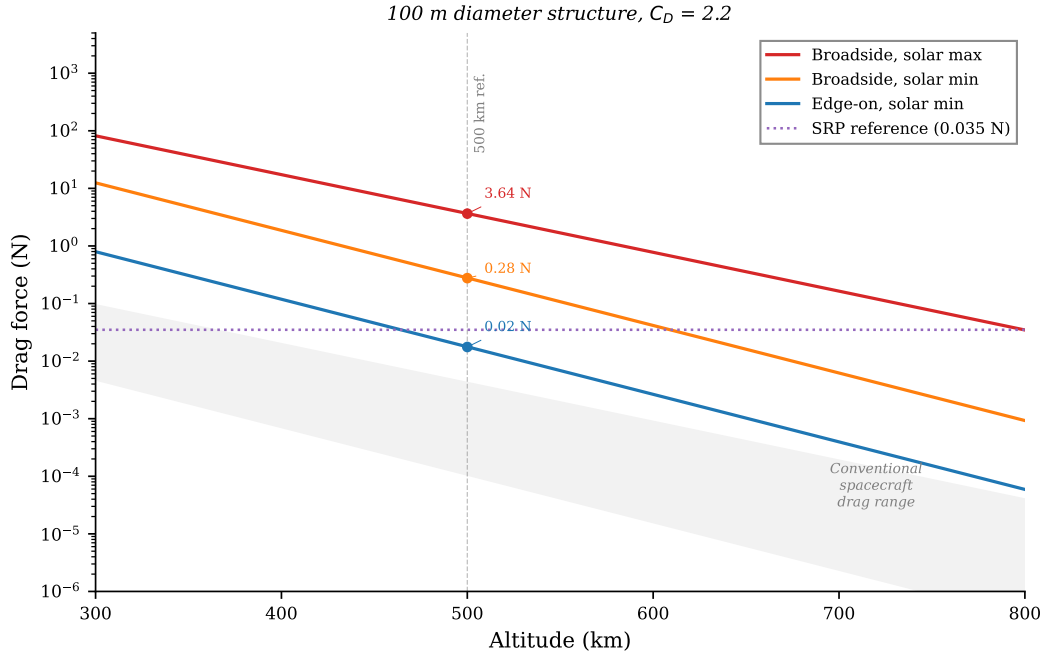


Figure 11: Drag force versus altitude for a 100 m diameter inflatable structure in LEO, showing solar minimum and solar maximum atmospheric conditions. The shaded region illustrates the factor-of-six variation in atmospheric density driven by the solar cycle, which dominates the orbit maintenance propellant budget.

1938 solar maximum can be estimated at approximately 3–6 months for broadside orientation,  
 1939 confirming that orbital lifetime without propulsion would be months, not years.

## 1940 Second-Order Effects

1941 Three additional forces merit consideration for a complete 100 m-class force budget:

1942 **Solar radiation pressure (SRP):** For a 100 m diameter membrane at 500 km, the SRP  
 1943 force is  $F_{\text{SRP}} = (P_{\odot}/c) \cdot A \cdot (1 + r) \approx (4.56 \times 10^{-6} \text{ N/m}^2) \times 7,850 \text{ m}^2 \times 1.5 \approx 0.054 \text{ N}$ , where  
 1944  $P_{\odot} = 1,361 \text{ W/m}^2$  is the solar flux,  $c$  is the speed of light, and  $r \approx 0.5$  is the reflectivity.  
 1945 This SRP force is comparable to the drag at solar minimum edge-on (0.007 N) and non-  
 1946 negligible—at solar minimum with edge-on orientation, SRP may actually dominate over  
 1947 atmospheric drag.

1948 **Attitude-dependent cross-section:** The table presents edge-on (100 m<sup>2</sup>) and broad-  
 1949 side (7,850 m<sup>2</sup>) as discrete cases, but a real membrane oscillates between attitudes unless  
 1950 actively controlled. The time-averaged effective area depends on AOCS capability—coupling  
 1951 the drag analysis to the AOCS gap (C4). Passive spin stabilisation about the minimum-  
 1952 inertia axis would yield a time-averaged  $A_{\text{eff}}$  intermediate between edge-on and broadside,  
 1953 approximately  $0.5 \times A_{\text{broadside}} \approx 3,900 \text{ m}^2$ , roughly halving the broadside drag but still orders  
 1954 of magnitude above edge-on.

1955 **Propellant mass rate derivation:** The xenon propellant consumption for Hall thruster  
 1956 drag compensation can be derived as  $\dot{m} = F_D/(g_0 I_{\text{sp}})$ , where  $g_0 = 9.81 \text{ m/s}^2$  and  $I_{\text{sp}} = 3,000 \text{ s}$

1957 for a representative Hall thruster. For the solar-minimum broadside case ( $F_D = 0.35$  N):  
 1958  $\dot{m} = 0.35/(9.81 \times 3,000) = 1.19 \times 10^{-5}$  kg/s = 1.03 kg/day = 376 kg/year. For the solar-  
 1959 maximum broadside case ( $F_D = 21$  N):  $\dot{m} = 21/(9.81 \times 3,000) = 7.14 \times 10^{-4}$  kg/s =  
 1960 61.7 kg/day—clearly unsustainable without in-orbit refuelling. The corresponding thrust  
 1961 power is  $P = F_D v_e / (2\eta)$ , where  $v_e = g_0 I_{sp} = 29,430$  m/s and  $\eta = 0.6$  (thruster efficiency):  
 1962 yielding 8.6 kW for the solar-minimum broadside case and 515 kW for the solar-maximum  
 1963 broadside case. The 1–50 kW range stated in Section 13.2 corresponds to solar-minimum  
 1964 conditions with partial edge-on attitude control.

1965 Air-Breathing Electric Propulsion (ABEP), which collects atmospheric gas for use as  
 1966 propellant, has been proposed for drag compensation in Very Low Earth Orbit (VLEO,  
 1967 150–450 km) Andreussi et al. [2022]. However, at 500 km the atmospheric density is approx-  
 1968 imately  $100\times$  lower than at the 250–350 km altitudes where ABEP is designed to operate,  
 1969 reducing achievable thrust to 0.001–0.1 mN—orders of magnitude insufficient for the 0.35–  
 1970 21 N drag forces computed above. Conventional electric propulsion (Hall effect or gridded  
 1971 ion thrusters) with onboard xenon propellant is the only viable station-keeping option. This  
 1972 propulsion requirement fundamentally constrains mission architecture and represents a sig-  
 1973 nificant fraction of the overall mass budget.

## 1974 11.4 The Missing Theory: AOCS for Pressure-Stabilised Mem- 1975 branes

1976 The gyroelastic body framework of D’Eleuterio and Hughes assumes elastic continua with  
 1977 Cauchy stress tensor constitutive relations—valid for beams, plates, and shells with inher-  
 1978 ent bending stiffness. Extending this framework to pressure-stabilised inflatable membranes  
 1979 requires four theoretical modifications that represent a significant gap in the published lit-  
 1980 erature:

- 1981 1. **Pressure-stiffness coupling:** For an inflatable structure, the effective stiffness  $K_{\text{eff}} =$   
 1982  $K_{\text{membrane}} + K_{\text{pressure}}$ , where the pressure contribution depends on inflation state and  
 1983 couples to deformation through the ideal gas law. When pressure changes due to mi-  
 1984 croleaks or thermal cycling, natural frequencies shift and gyroelastic modes reconfigure—  
 1985 a time-varying system for which fixed-gain controllers may become unstable.
- 1986 2. **Wrinkling constraint:** Membranes cannot carry compressive stress; they wrinkle,  
 1987 creating zones where  $\sigma_n = \max(0, T_{\text{membrane}} \cdot \varepsilon_n)$ . This state-dependent nonlinearity  
 1988 causes mode shapes to change with the deformation state, invalidating the linear modal  
 1989 analysis assumption that underpins both the D’Eleuterio framework and the Cachim  
 1990 optimisation.
- 1991 3. **Orthotropic fabric constitutive model:** Space fabrics (Vectran, Kevlar) are woven  
 1992 materials with highly anisotropic stiffness—warp versus weft direction stiffness can  
 1993 differ by  $2\text{--}5\times$ . The isotropic elastic continuum in the D’Eleuterio formulation requires  
 1994 replacement with an orthotropic constitutive model.
- 1995 4. **Gas-structure interaction coupling:** For large inflatable volumes, internal gas has  
 1996 its own dynamics (acoustic modes, pressure wave propagation). This is analogous to

1997 liquid sloshing in fuel tanks—a well-studied problem—but the gas-structure coupling  
1998 for inflatable membranes has received no published treatment.

1999 Each of these extensions builds upon established prior work, and the timeline can be  
2000 estimated with some granularity:

- 2001 • **Pressure-stiffness coupling** (estimated 3–4 years): The coupling of inflation pressure  
2002 to membrane stiffness is well-understood for simple geometries through the gossamer  
2003 structure dynamics literature [Jenkins \[2001\]](#). The novel challenge is coupling this to the  
2004 gyroelastic formulation, requiring a pressure-dependent constitutive model within the  
2005 D’Eleuterio framework. This is the most tractable extension and could be addressed  
2006 within a focused doctoral programme.
- 2007 • **Wrinkling constraint** (estimated 3–4 years): Tension-field theory [Stein and Hedgepeth](#)  
2008 [\[1961\]](#) provides a well-established framework for membranes that cannot sustain com-  
2009 pression. Roddeman et al. [Roddeman et al. \[1987\]](#) developed the modern computa-  
2010 tional treatment. Integrating wrinkling-induced state-dependent stiffness into gyro-  
2011 elastic eigenvalue analysis is non-trivial but has analogues in rotor dynamics (cracked  
2012 shaft models with breathing cracks).
- 2013 • **Orthotropic fabric constitutive model** (estimated 1–2 years): Replacing isotropic  
2014 with orthotropic constitutive relations requires substituting the appropriate fourth-  
2015 order stiffness tensor into the D’Eleuterio equations. The D’Eleuterio formulation uses  
2016 the general Cauchy stress tensor, making the extension algebraically systematic. This  
2017 is the most tractable extension and could constitute the early phase of a doctoral  
2018 programme or a Master’s thesis.
- 2019 • **Gas-structure interaction coupling** (estimated 4–5 years): This is the most novel  
2020 and uncertain extension. The fuel-sloshing analogy [Abramson \[1966\]](#) is useful but  
2021 incomplete—gas is compressible while classical sloshing models assume incompressibil-  
2022 ity. Coupled gas-membrane problems have been studied in the aeroelasticity literature  
2023 (flutter of inflated membrane wings [Leclercq and de Langre \[2018\]](#)), providing a starting  
2024 point, but the three-dimensional coupling for large inflatable volumes in the gyroelastic  
2025 context has no precedent. This is the genuine multi-year research challenge.

2026 The total estimated timeline is 12–15 years if pursued sequentially by individual doctoral  
2027 candidates, or 5–7 years if pursued in parallel by a coordinated research group with 2–3  
2028 concurrent doctoral projects. The sequential estimate of 10–15 years stated in Section 13  
2029 is therefore conservative but reasonable. This is among the most significant fundamental  
2030 research gaps identified in this survey.

## 2031 12 State of the Art: Robotic In-Orbit Assembly

2032 The vision of large inflatable space structures—100 m-class debris shields, large-aperture  
2033 antenna reflectors, or orbital habitats exceeding ISS volume—will likely require in-orbit  
2034 assembly of subsystems that exceed the launch vehicle fairing envelope or are too complex

2035 for single-deployment architectures. This section reviews the state of in-space servicing,  
2036 assembly, and manufacturing (ISAM) robotics, the E-Walker concept for walking robots on  
2037 large structures, and the critical gap in rigid-to-flexible interface technology that currently  
2038 prevents assembly on inflatable substrates.

## 2039 **12.1 Assembly Robot Heritage and Current Programmes**

2040 In-orbit robotic assembly heritage begins with the ISS, whose construction (1998–2011) relied  
2041 on the Canadarm2 Space Station Remote Manipulator System (SSRMS): a 17.6 m, 7-DOF  
2042 arm operating from fixed Power Data Grapple Fixtures (PDGFs) on the truss structure.  
2043 Canadarm2 demonstrated that large-scale orbital assembly is achievable with telerobotic  
2044 systems, but at the cost of extensive EVA support and ground-in-the-loop operations.

2045 The ISAM landscape has expanded substantially since ISS assembly. NASA’s 2025 State  
2046 of Play report catalogues 524 capability entries across 145 developers in 21 countries, with  
2047 over \$2 billion in government investment [NASA \[2025\]](#). Current programmes span mul-  
2048 tiple technology readiness levels: GITAI’s S2 experiment demonstrated autonomous ISS  
2049 solar array assembly (2021); Project GHOST validated tool manipulation in orbit (2024);  
2050 DARPA’s NOM4D programme targets LEO truss assembly demonstration by Caltech in  
2051 2026; and NASA Langley’s CIRAS/TALISMAN/SAMURAI/NINJAR ground demonstra-  
2052 tions have validated multi-robot truss assembly at 15 m scale [Li et al. \[2022c\]](#), [Doggett et al.](#)  
2053 [\[2018\]](#). The European PULSAR project targets autonomous assembly of a 12 m telescope  
2054 mirror [Rognant et al. \[2019\]](#). Northrop Grumman’s MEV-1 (2020) and MEV-2 (2021) rep-  
2055 resent the first commercial ISAM operations, though these are servicing (docking with client  
2056 spacecraft) rather than structural assembly.

2057 A critical observation for the present survey is that all 524 entries in the NASA ISAM  
2058 catalogue address assembly of rigid structures—trusses, beams, modular satellites, and mir-  
2059 ror segments [NASA \[2025\]](#). Not a single entry addresses assembly on or of inflatable/flexible  
2060 substrates. This is not a mere omission; it reflects a fundamental gap in the technology base:  
2061 the rigid-to-flexible interface problem remains unsolved (Section [12.3](#)).

## 2062 **12.2 Walking Robots for Large Structure Assembly: E-Walker**

2063 The End-over-End Walking Robot (E-Walker) represents the current state of the art in  
2064 walking manipulators designed for ISAM missions [Nair et al. \[2022, 2024\]](#). Inheriting the  
2065 Canadarm2 design philosophy of end-over-end locomotion via grapple fixtures, the E-Walker  
2066 is a 7-DOF dexterous manipulator at full scale of approximately 475 kg with 350 kg pay-  
2067 load capacity—sufficient to handle one primary mirror segment for a 25 m Large Aperture  
2068 Space Telescope (LAST). Maximum joint torque reaches  $\sim 70$  Nm at Joint 2, and finite ele-  
2069 ment analysis confirms maximum link deflection of only 0.04 mm under full payload, with a  
2070 buckling safety factor exceeding 129 [Nair et al. \[2022\]](#).

2071 A scaled prototype (1.3 m, 12 kg, 2 kg payload at 1:6 scale) has been demonstrated in  
2072 ground testing. [Nair et al. \[2024\]](#) evaluated 11 concepts of operations for 25 m  
2073 telescope assembly, concluding that a dual E-Walker configuration is optimal. The 8 m E-  
2074 Walker requires 4.5 m less workspace than an equivalent fixed-base arm, making walking  
2075 locomotion particularly advantageous for assembly tasks distributed over large structures.

2076 However, all E-Walker analysis assumes a rigid assembly substrate. The grapple fix-  
2077 tures are ISS-standard PDGFs requiring rigid interfaces with  $\pm 10$  mm capture tolerance and  
2078 multi-kN load capacity. When the E-Walker applies 70 Nm joint torques during assembly  
2079 operations, Newton’s third law transmits equal and opposite reactions into the mounting  
2080 substrate. On the ISS rigid truss, these are absorbed globally; on an inflatable membrane,  
2081 they would cause local deformation, potential wrinkling, and excitation of global vibration  
2082 modes. The 475 kg robot’s every movement in microgravity creates reaction forces that, on  
2083 a flexible membrane, propagate as structural disturbances.

### 2084 12.3 The Rigid-to-Flexible Interface Gap

2085 All existing docking and assembly interfaces assume rigid-to-rigid connections. Chen et al.  
2086 Liu et al. [2024] designed an androgynous docking port with  $\pm 23.5$  mm translation tolerance  
2087 for on-orbit assembly—a practical engineering specification for robotically-assisted mating  
2088 of rigid modules. ISS Power Data Grapple Fixtures, common berthing mechanisms, and all  
2089 ISAM interface concepts in the literature share this rigid-to-rigid assumption.

2090 No published work specifically addresses distributed rigid-module attachment to inflat-  
2091 able membranes in the space environment. However, several bodies of adjacent work provide  
2092 relevant design heritage that should be acknowledged:

- 2093 • **Tensegrity structures:** Tensegrity platforms Skelton and de Oliveira [2009] inher-  
2094 ently address the rigid-to-flexible interface through bar-cable connections. NASA  
2095 Ames’ Super Ball Bot Sabelhaus et al. [2015] demonstrates rigid node attachment to  
2096 tensioned cables in a reconfigurable structure; the load-spreading problem at hardpoint-  
2097 membrane interfaces is structurally analogous to the bar-cable joint in tensegrity.
- 2098 • **Deployable antenna feed support:** Large deployable mesh antennas (Harris/L3  
2099 AstroMesh, Northrop Grumman CRAF) attach a rigid feed assembly to a tensioned  
2100 cable-net/mesh reflector surface Santiago-Prowald and Rodrigues [2018]. The feed  
2101 support struts connect rigid hardware to a flexible, tension-stabilised structure—a  
2102 direct analogue to the rigid-module-on-inflatable-membrane problem.
- 2103 • **Solar sail boom-membrane attachment:** Solar sail designs (e.g., IKAROS, NEA  
2104 Scout) attach rigid booms to thin-film membranes via reinforced corner fittings. The  
2105 stress concentration and load distribution at these attachment points have been anal-  
2106 ysed in the solar sail literature Fernandez et al. [2014].

2107 The gap remains genuine: none of these analogues addresses the full combination of vac-  
2108 uum, thermal cycling, atomic oxygen, micrometeoroid exposure, and zero-gravity dynamics  
2109 on an inflatable pressure-stabilised substrate. The adjacent work provides starting points  
2110 for analysis but not validated solutions.

2111 Table 21 summarises the technology readiness of assembly interface approaches.

2112 The closest flight analog is the BEAM-ISS interface: a rigid berthing ring connects the  
2113 inflatable module to the ISS Node 3 (Tranquility) common berthing mechanism. This is a  
2114 single rigid-to-inflatable joint at the berthing interface, not a distributed attachment system  
2115 across the membrane surface. No demonstrated technology exists for attaching multiple rigid

Table 21: Assembly interface technology readiness for space structures.

Interface Type	TRL	Heritage	Notes
Rigid-to-rigid (PDGF)	9	ISS	Operational since 2001
Rigid-to-rigid (androgynous)	3–4	Ground demo	Chen et al. 2024
Rigid-to-flexible (hardpoint)	2–3	BEAM ring	Conceptual only
Rigid-to-flexible (distributed)	1–2	None	No published work

subsystems (reaction wheels, solar array drives, communications antennas) to an inflatable membrane at distributed locations. This is a novel finding of this survey and represents a critical research gap.

## 12.4 Assembly-Enabled Inflatable Platforms: Design Requirements

Based on the analysis in Sections 12.2–12.3, a set of design requirements for assembly-enabled inflatable platforms can be identified:

- Embedded rigid attachment rings:** Metallic rings (0.5–1 m diameter) must be sewn into the inflatable fabric at pre-determined assembly points during manufacturing, with integrated load-spreading plates to distribute reaction forces over sufficient membrane area. The stress concentration factor at such embedded hardpoints (2–5× local stress amplification) must be accounted for in the membrane structural design.
- Compliance layer:** A 3–5 mm silicone or elastomeric foam layer between each rigid attachment ring and the membrane accommodates local deformation and provides vibration isolation, preventing point-load damage to the fabric.
- Pre-integration requirement:** Retrofitting hardpoints onto an already-deployed inflatable is impractical. All assembly interfaces must be designed in and manufactured as part of the inflatable structure before launch. This implies that the assembly concept of operations must be fully defined before the inflatable is manufactured—a significant systems engineering constraint.
- Active vibration isolation:** Small dampers or isolation mounts between each E-Walker grapple point and the membrane surface attenuate reaction forces from assembly operations, reducing excitation of global membrane vibration modes.
- Pressure-aware operations:** Assembly operations that change the mass distribution (adding subsystems) alter both the inertia tensor and the natural frequencies of the inflatable structure. AOCS must accommodate these time-varying dynamics—connecting to the gap identified in Section 11.4.

The E-Walker on an inflatable platform is conditionally feasible with pre-integrated hardpoints, compliance layers, and active vibration isolation. However, none of these solutions has been demonstrated even at component level for space applications. A ground demonstration

2145 programme—analogue to NASA Langley’s CIRAS/TALISMAN truss assembly demonstra-  
2146 tions but on an inflatable test article—would represent a significant advance toward closing  
2147 this gap.

## 2148 13 Challenges, Open Questions, and Research Roadmap

2149 The preceding eight technology surveys (Sections 5–12) have documented a paradox that  
2150 defines the current state of soft inflatable robotic systems for space: individual enabling tech-  
2151 nologies have reached moderate-to-high readiness levels—Vectran restraint layers at TRL 9  
2152 (Section 5), shape memory alloy deployment actuators at TRL 8–9 (Section 7.5), fibre Bragg  
2153 grating sensors on rigid spacecraft at TRL 7–8 (Section 8.1)—yet no integrated soft inflat-  
2154 able robotic system has been demonstrated in space. This section consolidates the research  
2155 gaps identified throughout the survey, assesses their severity and interdependence, proposes  
2156 a structured research roadmap spanning 5-year and 15-year horizons, and identifies the most  
2157 viable path to a near-term flight demonstration.

### 2158 13.1 Critical Research Gaps

2159 A systematic analysis of the technology areas reviewed in Sections 5–12 reveals 5 critical  
2160 gaps, 9 moderate gaps, and 10 minor gaps. Here we consolidate the 5 critical gaps, each of  
2161 which represents a showstopper for at least one major application domain.

2162 **C1: Absence of Quantitative Soft-versus-Rigid Fragmentation Comparison.** The  
2163 central motivation for soft capture in active debris removal (Section 3.2) rests on the propo-  
2164 sition that compliant mechanisms reduce fragmentation risk relative to rigid robotic arms.  
2165 Qualitative evidence supports this argument: Wang et al. Wang et al. [2023] identified the  
2166 “potential to generate fragments during the capturing phase” for rigid systems; Chen et  
2167 al. Chen et al. [2024a] concluded that “single contact-based caging is excessively risky for  
2168 fast-tumbling targets”; and the RemoveDebris harpoon test demonstrated structural fail-  
2169 ure of a carbon fibre boom at  $20 \text{ m s}^{-1}$  impact Aglietti et al. [2020]. The e.deorbit mission  
2170 study computed peak joint torques of 195 N m for capture of an 8-tonne ENVISAT tumbling  
2171 at  $5^\circ \text{ s}^{-1}$  Flores-Abad et al. [2014]. However, no published study provides a quantitative  
2172 fragmentation probability as a function of contact compliance. The catastrophic fragmenta-  
2173 tion threshold ( $10 \text{ J g}^{-1}$  specific energy from the IMPACT model Johnson et al. [2001]) has  
2174 never been applied to a soft-versus-rigid capture force comparison. The fragmentation risk  
2175 is physically plausible and supported by qualitative assessments—particularly for degraded  
2176 appendages (solar panels, thermal blankets, antennas) that may have lost 30–60% of their  
2177 original strength through decades of space environment exposure—but remains experimen-  
2178 tally unquantified. This survey adopts the precautionary principle that compliant capture  
2179 is preferred until quantitative data become available, on the basis that the consequences of  
2180 inadvertent fragmentation are severe enough to warrant risk-averse technology selection. We  
2181 propose this as the single highest-priority experimental investigation the community should  
2182 undertake, requiring hypervelocity and low-velocity impact testing with debris surrogates at  
2183 varying contact compliance levels.

2184 **C2: No Soft Robotic Capture System Has Flown in Space.** Despite eight distinct  
2185 soft or compliant capture approaches documented in Section 3.2—gecko adhesive (TRL 4–  
2186 5), DEMES grippers (TRL 3–4), bistable soft grippers (TRL 2–3), cryogenic metallic cable  
2187 robots (TRL 3), inflatable origami arms (TRL 3), flytrap origami (TRL 2–3), thermally  
2188 qualified multi-layer grippers (TRL 2), and the INSIDeR system concept (TRL ~4)—none  
2189 has flown. The gecko adhesive gripper of Jiang et al. [Jiang et al. \[2017\]](#) achieved microgravity  
2190 validation with 100% capture success rate on spherical targets and capacity exceeding 400 kg,  
2191 making it the most mature candidate. However, this gripper operates on a rigid robotic arm  
2192 platform and is more accurately classified as a compliant end-effector on a conventional  
2193 manipulator (Section 3.1). The gap between ground/parabolic-flight demonstration and or-  
2194 bital flight requires addressing space environment qualification (vacuum outgassing, thermal  
2195 cycling, radiation exposure over mission-duration timescales) for which limited data exist.

2196 **C3: Rigid-to-Flexible Assembly Interface Lacks Specific Published Research.**  
2197 Section 12.3 identified that no published work specifically addresses distributed rigid-module  
2198 attachment to inflatable membranes in the space environment, though adjacent work in  
2199 tensegrity structures [Skelton and de Oliveira \[2009\]](#), [Sabelhaus et al. \[2015\]](#), deployable an-  
2200 tenna feed supports [Santiago-Prowald and Rodrigues \[2018\]](#), and solar sail boom-membrane  
2201 attachments [Fernandez et al. \[2014\]](#) provides relevant design heritage. All heritage docking  
2202 interfaces—ISS PDGF, Common Berthing Mechanism, ClearSpace-1 capture arms, and the  
2203 androgynous interfaces reviewed by Chen et al. [Chen et al. \[2024b\]](#)—assume rigid-to-rigid  
2204 mating. At the 100-metre scale required for large inflatable debris shields (Section 11.3) or  
2205 solar power platforms, the inflatable structure becomes a platform onto which functional  
2206 modules must be assembled in orbit [Nair et al. \[2024\]](#), [Li et al. \[2019\]](#). The reaction force  
2207 problem—how to apply assembly torques to a membrane that deforms under the applied  
2208 load—has no published solution specific to the space inflatable context. Embedded metallic  
2209 hardpoint rings represent a plausible design concept informed by the tensegrity and antenna  
2210 feed analogues, but require detailed finite element analysis of stress concentration at the  
2211 rigid-flexible interface, none of which has been published.

2212 **C4: No Published AOCS Theory for Pressure-Stabilized Inflatable Structures.**  
2213 The control-structure interaction literature reviewed in Section 11.1 addresses rigid trusses,  
2214 mesh antennas, and mechanically stiffened deployable arrays—structures with inherent stiff-  
2215 ness independent of pressurization. Pressure-stabilized inflatable structures exhibit funda-  
2216 mentally different dynamics: stiffness is a function of inflation pressure (a time-varying pa-  
2217 rameter), membranes wrinkle under compression introducing piecewise-linear stiffness non-  
2218 linearity, fabric is anisotropic, and internal gas couples to structural modes [D’Eleuterio  
2219 and Hughes \[1984\]](#), [Jenkins \[2001\]](#). The D’Eleuterio–Hughes gyroelastic body framework  
2220 [D’Eleuterio and Hughes \[1984, 1986, 1987\]](#) provides the most promising theoretical founda-  
2221 tion, but requires four extensions: (i) pressure-dependent constitutive model for membrane  
2222 elements, (ii) wrinkling constraints reflecting piecewise-linear stiffness transitions, (iii) or-  
2223 thotropic fabric constitutive laws, and (iv) gas-structure coupling for internal atmosphere  
2224 dynamics. Each extension constitutes a substantial theoretical undertaking; collectively they  
2225 define a research programme of 10–15 years.

2226 **C5: Inflatable-Power Integration Gap.** The PowerSphere programme (Section 9.2)  
 2227 demonstrated thin-film photovoltaic integration with an inflatable substrate using amor-  
 2228 phous silicon cells, achieving  $7.25 \text{ W kg}^{-1}$  at 10% cell efficiency Cadogan et al. [2003]. The  
 2229 programme has been inactive since approximately 2009, and no successor has been identified.  
 2230 Meanwhile, perovskite/CIGS tandem cells have achieved  $2100 \text{ W kg}^{-1}$  with  $25 \mu\text{m}$  substrates  
 2231 and greater than 85% power retention after more than 50 years of LEO-equivalent proton irra-  
 2232 diation Lang et al. [2020]. The technology exists to revive inflatable-integrated photovoltaics  
 2233 at  $20\text{--}300\times$  the specific power of the original PowerSphere, yet no programme is pursuing  
 2234 this integration. The gap is institutional rather than technical: flexible PV researchers and  
 2235 inflatable structure researchers operate in separate communities with no overlap programme.

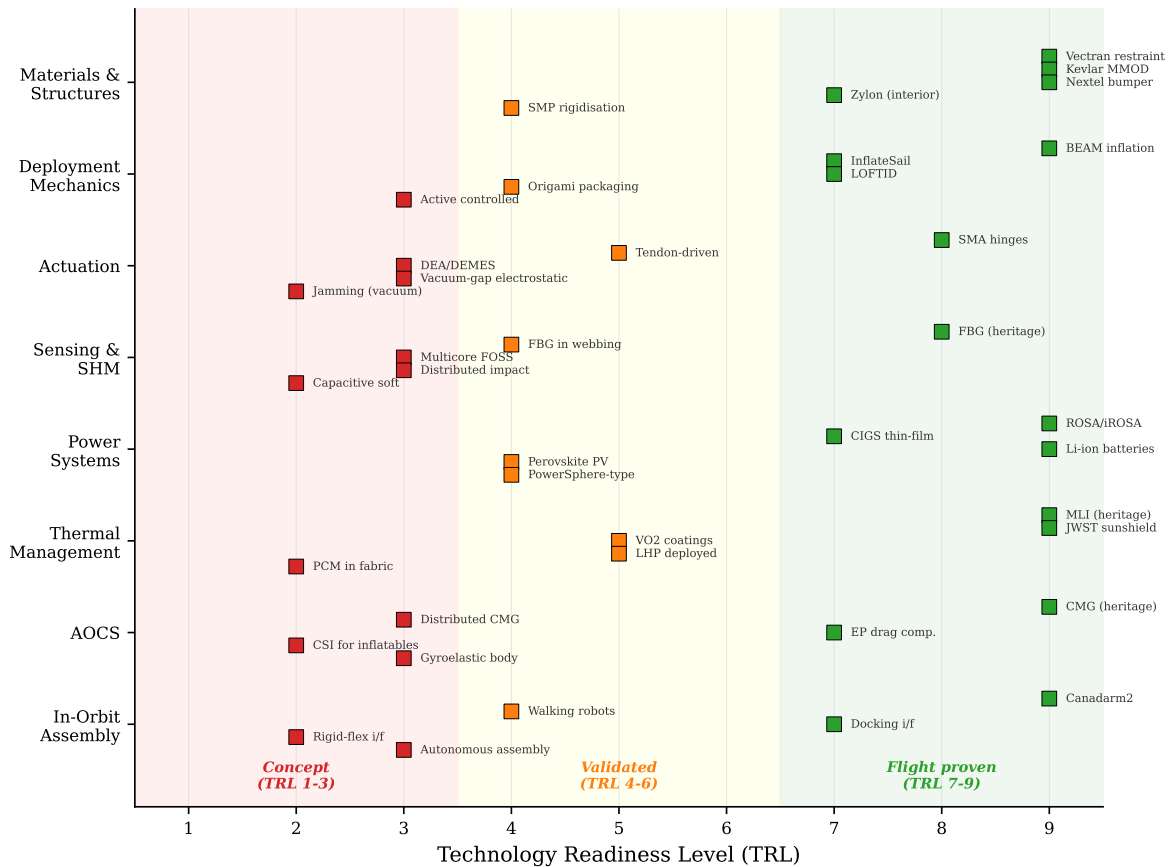


Figure 12: Technology readiness landscape across the eight enabling technology areas reviewed in Sections 5–12. Each marker represents a specific sub-technology; colour indicates TRL band (red: concept TRL 1–3; orange: validated TRL 4–6; green: flight-proven TRL 7–9). While heritage components (Vectran, FBG, ROSA, MLI, Canadarm2) have reached TRL 7–9, the integrative technologies required for soft inflatable robotic systems—vacuum-gap actuators, jamming in vacuum, rigid-to-flexible interfaces, distributed momentum management, and PCM in fabric—remain at TRL 2–3.

## 13.2 Integration Challenges at System Level

Beyond individual technology gaps, the fundamental barrier to flight-ready soft inflatable robotic systems is *system integration*. The preceding sections documented integration deficits across multiple interfaces:

- **Actuation–Structure:** Vacuum-gap electrostatic actuators (Section 7.2) achieve  $>4$  N force at 0.7 g mass [Sirbu et al. \[2025\]](#) using thin-film polymer multilayer construction that is structurally analogous to inflatable membrane wall architectures—yet no study has attempted to laminate actuator layers into an inflatable arm liner. Similarly, the jamming-in-vacuum concept (Section 7.6) has a sound physical basis [Fitzgerald et al. \[2020\]](#) but zero experimental validation in relevant conditions.
- **Sensing–Structure:** FBG sensors woven into Vectran webbing have been demonstrated at NASA JSC on 0.61 m and 2.74 m test articles (TRL 4–5) [Bally Ribbon Mills and Luna Innovations \[2020\]](#), while multicore fibre optic shape sensing achieves 0.64 mm position accuracy in soft actuators [Galloway et al. \[2019\]](#). The same FBG technology could provide both structural health monitoring for inflatable walls and proprioceptive sensing for inflatable robotic arms—a unified sensing architecture that has not been proposed or demonstrated.
- **Power–Thermal–Structure:** A large inflatable membrane with thin-film PV on the sun-facing surface, MLI on the space-facing surface, and variable-emissivity coatings for thermal regulation represents a multi-functional surface that would merge the power and thermal subsystems into a single membrane layer. The PowerSphere concept approached this integration using 2004-era materials [Cadogan et al. \[2003\]](#); 2025-era perovskite/CIGS cells on Kapton or Mylar substrates would share the same polymer base as inflatable MLI layers [Lang et al. \[2020\]](#), making the integration pathway plausible.
- **AOCS–Deployment:** BEAM’s deployment anomaly (25 inflation bursts over 7 hours; Section 6.3) illustrates that deployment is a dynamic event with angular momentum consequences. For a free-flying 100-metre inflatable, each inflation pulse imparts momentum to the structure, and as the structure changes shape during deployment its modal frequencies shift—potentially crossing into the AOCS controller bandwidth [D’Eleuterio and Hughes \[1984\]](#). No published work addresses the coupled deployment–AOCS problem for inflatables.
- **Drag–Power–Thermal Cascade:** At 500 km altitude, a 100-metre broadside inflatable experiences drag forces of 0.35–21 N depending on solar activity (Section 11.3). To illustrate the cascade quantitatively, consider a worked example for the solar-minimum broadside case ( $F_D = 0.35$  N) and the solar-maximum broadside case ( $F_D = 21$  N):  
*Step 1 — Thrust:* Hall thruster at  $I_{sp} = 3,000$  s, exhaust velocity  $v_e = g_0 I_{sp} = 29,430$  m/s.  
*Step 2 — Power:*  $P_{thrust} = F_D v_e / (2\eta)$  where  $\eta = 0.6$ . Solar-min broadside:  $P = 0.35 \times 29,430 / 1.2 = 8.6$  kW. Solar-max broadside:  $P = 21 \times 29,430 / 1.2 = 515$  kW.

2275 *Step 3 — Solar array:* At  $300 \text{ W m}^{-2}$  (BOL, triple-junction) and  $100 \text{ W kg}^{-1}$  system-  
2276 level specific power: solar-min requires  $29 \text{ m}^2 / 86 \text{ kg}$ ; solar-max requires  $1,717 \text{ m}^2 /$   
2277  $5,150 \text{ kg}$ —exceeding the entire platform mass budget.

2278 *Step 4 — Waste heat:* At 40% combined losses (thruster + PPU): solar-min generates  
2279 3.4 kW waste; solar-max generates 206 kW waste.

2280 *Step 5 — Radiator:* At  $200 \text{ W m}^{-2}$  radiator capacity: solar-min requires  $17 \text{ m}^2$ ; solar-  
2281 max requires  $1,030 \text{ m}^2$ .

2282 This cascade demonstrates that the solar-maximum broadside scenario is infeasible  
2283 without active attitude control to reduce  $A_{\text{eff}}$ , confirming that drag budget and AOCS  
2284 capability are inextricably coupled. Edge-on operation at solar minimum ( $0.007 \text{ N}$   
2285 drag,  $\sim 0.17 \text{ kW}$  power,  $< 1 \text{ m}^2$  array) is feasible; all other scenarios require either ac-  
2286 tive attitude management, altitude selection, or both. The 1–50 kW range previously  
2287 stated applies to solar-minimum conditions with partial attitude control. No pub-  
2288 lished analysis traces this full cascade end-to-end for inflatable platforms, and a com-  
2289 plete parametric study spanning altitude, solar cycle, attitude strategy, and propulsion  
2290 technology is identified as a future research need.

2291 A unifying observation emerges: the integration barriers are not gaps within individual  
2292 technology disciplines but gaps *between* disciplines. The soft robotics community, the inflat-  
2293 able structures community, the space power community, and the GNC community each have  
2294 mature capabilities; the intersections remain unexplored. This fragmentation of the research  
2295 landscape is itself a structural challenge that programmatic measures (cross-disciplinary  
2296 funding calls, joint ground demonstrators) must address.

### 2297 **13.3 Proposed Research Roadmap: 5-Year and 15-Year Horizons**

2298 Based on the gap analysis above and the technology readiness levels documented in Sec-  
2299 tions 5–12, we propose a two-horizon research roadmap. The 5-year horizon (2026–2031)  
2300 targets ground validation and component-level flight demonstration; the 15-year horizon  
2301 (2026–2041) targets system-level flight demonstration and initial operational capability.

2302 **5-Year Horizon (2026–2031).** Five priority activities are identified, each addressing one  
2303 or more critical or moderate gaps:

2304 1. **Jamming-in-vacuum experimental validation** (addresses M1). Ground experi-  
2305 ment: vacuum chamber with sealed granular/layer jamming specimen connected to a  
2306 pressurized chamber simulating an inflatable interior. Measure stiffness ratio versus  
2307 pressure differential and compare to terrestrial baselines. Space-compatible granular  
2308 media candidates include hollow glass microspheres and metallic powder. This ex-  
2309 periment is well-defined, moderate-cost, and publishable regardless of outcome. If  
2310 successful, it validates variable-stiffness robotic elements that are simpler in orbit than  
2311 on Earth—a paradigm inversion for soft space robotics.

2312 2. **FBG-in-Vectran-webbing flight demonstration** (addresses M6). Current ground  
2313 demonstrations at NASA JSC [Bally Ribbon Mills](#) and [Luna Innovations](#) [2020] have

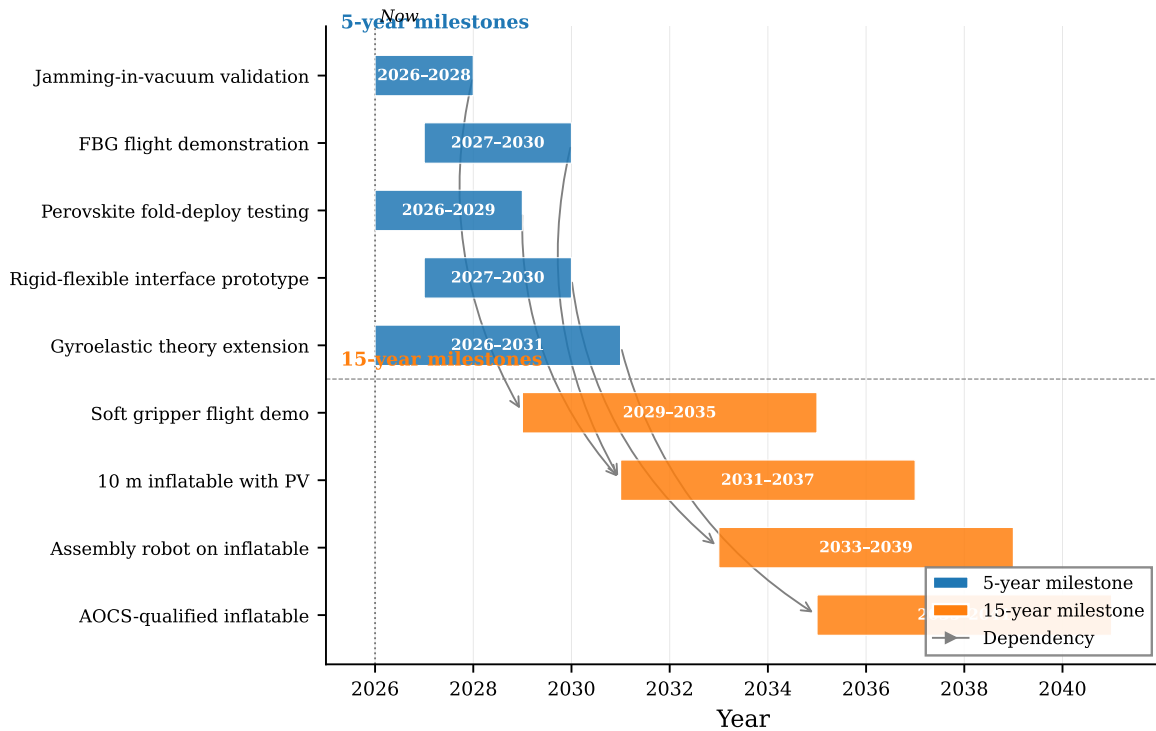


Figure 13: Research roadmap for soft inflatable robotic space systems spanning 5-year and 15-year horizons. Near-term milestones focus on ground validation of critical unknowns (jamming-in-vacuum, FBG flight, perovskite fold-deploy, rigid-flexible interface); long-term milestones target integrated flight demonstrations (soft gripper capture, 10 m inflatable with PV, assembly robot on inflatable substrate, AOCS-qualified inflatable).

2314 reached TRL 4–5. The next step is a flight experiment on an ISS external payload  
2315 platform (e.g., MISSE or Bartlett) exposing FBG-instrumented Vectran webbing to the  
2316 LEO environment (atomic oxygen, UV, thermal cycling, MMOD) for 12–24 months.  
2317 Success would advance the technology to TRL 6–7 and establish the flight heritage  
2318 base for inflatable SHM.

2319 3. **Perovskite/CIGS fold-deploy-power testing** (addresses C5, M5). Deposit per-  
2320 ovskite/CIGS tandem cells on 25  $\mu\text{m}$  polymer substrates identical to those used for  
2321 inflatable MLI. Subject samples to 1000 fold/deploy mechanical cycles, 1000 thermal  
2322 vacuum cycles ( $-100^\circ\text{C}$  to  $120^\circ\text{C}$ ), and atomic oxygen exposure at LEO-equivalent  
2323 fluences. Measure power output degradation after each environmental stress. This  
2324 establishes whether the remarkable radiation hardness of perovskite/CIGS [Lang et al.](#)  
2325 [\[2020\]](#) survives the additional mechanical and environmental stresses of inflatable in-  
2326 tegration.

2327 4. **Rigid-to-flexible interface ground prototype** (addresses C3). Design, fabricate,  
2328 and test embedded metallic load-spreader rings sewn into representative multi-layer  
2329 inflatable fabric during manufacture. Characterize load distribution, stress concentra-  
2330 tion factors, and modal response under simulated assembly loading. Compare FEA  
2331 predictions with experimental measurements. This ground programme would produce  
2332 the first published dataset on rigid-to-flexible assembly interfaces for space inflatables.

2333 5. **Gyroelastic theory extension for pressure-stabilized membranes** (addresses  
2334 C4). Mathematical extension of the D’Eleuterio–Hughes framework [D’Eleuterio and](#)  
2335 [Hughes \[1984, 1986\]](#) incorporating pressure-dependent stiffness and fabric orthotropy.  
2336 Numerical validation against commercial FEM codes for representative inflatable ge-  
2337 ometries (cylinder, torus, sphere). Publication of the extended theory would establish  
2338 the foundational AOCs framework that any 100-metre-class inflatable mission will  
2339 require.

2340 **15-Year Horizon (2026–2041).** Four system-level demonstrations define the long-term  
2341 roadmap:

2342 1. **Soft gripper flight for debris capture** (addresses C1, C2). A CubeSat or small-  
2343 satellite class mission demonstrating compliant capture of a cooperative (then non-  
2344 cooperative) target in LEO. The gripper subsystem (gecko adhesive, DEMES, or suc-  
2345 cessor technology) operates on an inflatable arm with integrated FBG sensing. This  
2346 mission provides the first orbital data on soft capture dynamics and validates the frag-  
2347 mentation risk reduction argument with flight telemetry.

2348 2. **10-metre inflatable with integrated photovoltaics** (addresses C5). A free-flying  
2349 technology demonstrator deploying a 10-metre-class inflatable membrane with lami-  
2350 nated perovskite/CIGS cells, demonstrating fold/deploy survival and power generation  
2351 in the orbital environment. This bridges the gap between ROSA-class rigid-boom flex-  
2352 ible arrays (TRL 9) and the 100-metre inflatable solar platforms envisioned for future  
2353 missions.

2354  
2355  
2356  
2357  
2358  
2359  
2360  
2361  
2362  
2363

- 3. **Assembly robot on inflatable substrate** (addresses C3). A ground or parabolic-flight demonstration of a walking or crawling robot (E-Walker class [Nair et al. \[2024\]](#)) operating on an inflatable test article, attaching and detaching rigid modules via embedded hardpoint interfaces. This validates the rigid-to-flexible assembly concept in representative (reduced) gravity conditions.
- 4. **AOCS-qualified pressure-stabilized inflatable** (addresses C4). A free-flying inflatable structure (3–10 metre scale) with onboard AOCS demonstrating three-axis attitude control of a pressure-stabilized membrane in LEO. This validates the extended gyroelastic theory and provides the first flight data on control-structure interaction for inflatable spacecraft.

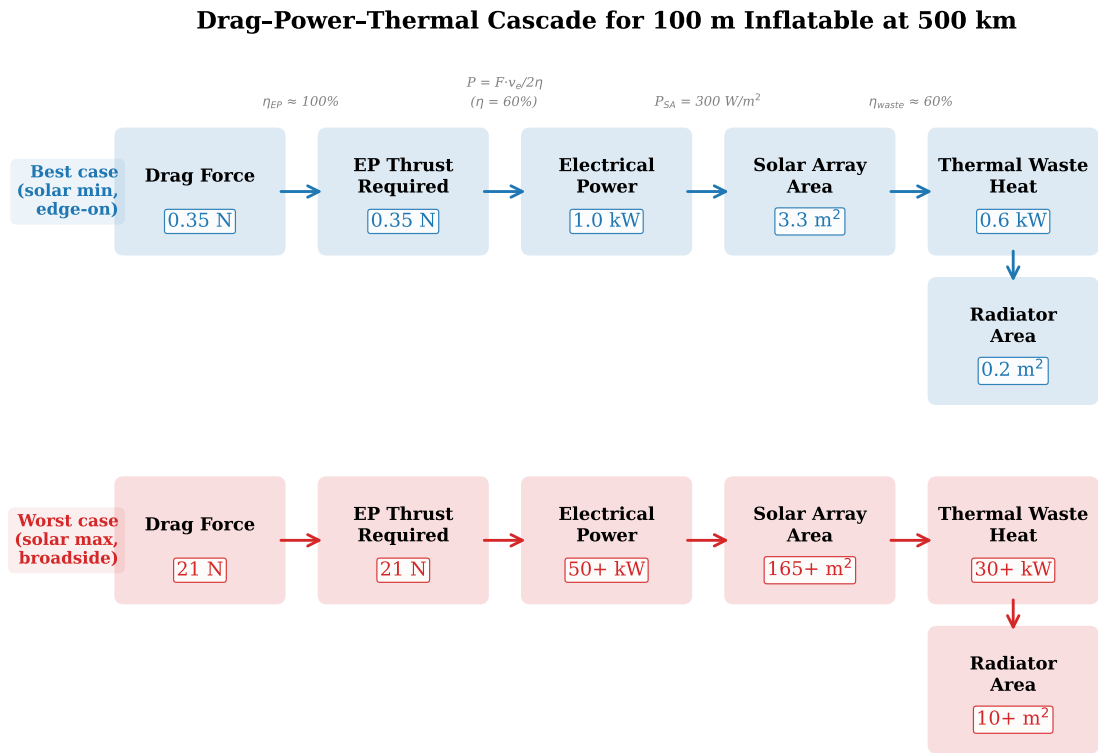


Figure 14: Drag-power-thermal cascade analysis for a 100-m-class inflatable structure in LEO, illustrating how atmospheric drag drives propulsion power requirements, which in turn drive solar array sizing and thermal dissipation budgets. The cascade quantifies the interdependence of the AOCS, power, and thermal subsystems.

## 2364 13.4 The Path to Flight Demonstration

2365 Among the roadmap milestones, the most flight-ready near-term demonstrator can be iden-  
2366 tified by selecting the highest-TRL components from each technology area and integrating  
2367 them into a single mission concept. The analysis in Sections 5–8 suggests the following  
2368 combination:

- 2369 • **Capture mechanism:** Gecko adhesive gripper (TRL 4–5, microgravity validated,  
2370 400 kg capacity) [Jiang et al. \[2017\]](#), noting that this is a compliant end-effector on a  
2371 conventional arm rather than a fully soft system.
- 2372 • **Arm structure:** Inflatable multi-link arm based on the POPUP concept (TRL 3)  
2373 [Palmieri et al. \[2023\]](#), using Vectran fabric links with FBG-instrumented webbing.
- 2374 • **Structural health monitoring:** FBG sensors in Vectran webbing (TRL 4–5 ground)  
2375 [Bally Ribbon Mills and Luna Innovations \[2020\]](#), providing both SHM and propriocep-  
2376 tive shape sensing via multicore FOSS principles [Galloway et al. \[2019\]](#).
- 2377 • **Deployment:** SMA-based hinge deployment for arm segments (TRL 8–9) [Costanza](#)  
2378 [and Tata \[2020\]](#).

2379 This combination achieves an estimated system TRL of 3–4, limited by the inflatable  
2380 arm structure. A CubeSat-class (12U–16U) demonstrator could validate the complete soft  
2381 capture concept—deploy inflatable arm, acquire cooperative target, demonstrate FBG-based  
2382 shape sensing during capture—within a 3–5 year development timeline from programme ini-  
2383 tiation. The mission would produce the first orbital dataset on: (i) inflatable arm deployment  
2384 dynamics, (ii) FBG sensor performance in the LEO environment on a flexible structure, and  
2385 (iii) compliant capture contact dynamics. These three datasets address critical gaps C2, M6,  
2386 and partially C1, making this demonstrator the highest-value single mission for advancing  
2387 the field.

2388 The key technical risk is the inflatable arm structure: POPUP-class arms have been  
2389 demonstrated only in simulation [Palmieri et al. \[2023\]](#), and the transition from analytical  
2390 design to space-qualified flight hardware requires a focused engineering programme. However,  
2391 the constituent technologies—Vectran fabric, SMA deployment mechanisms, FBG sensors—  
2392 each have independent space heritage that de-risks the integration challenge.

2393 A critical observation from the roadmap analysis is that the fragmentation paradox (Sec-  
2394 tion 3.1) will not be resolved by the flight demonstrator alone. The proposed CubeSat mission  
2395 validates soft capture *mechanics* but does not generate fragmentation data. Resolving gap  
2396 C1 requires a parallel ground campaign: hypervelocity and low-velocity impact testing with  
2397 debris surrogate materials (solar panel fragments, aluminium honeycomb, carbon fibre com-  
2398 posite) at representative contact forces, comparing rigid grasp, compliant grasp, and soft  
2399 envelopment capture modes. Parabolic flight campaigns can provide microgravity validation  
2400 of the ground results. Together, the flight demonstrator and the ground fragmentation study  
2401 would establish the quantitative evidence base that the soft ADR proposition currently lacks.

## 14 Conclusions

This survey has reviewed the state of the art in soft inflatable robotic systems for space applications, covering eight enabling technology areas across 14 sections and synthesizing findings from the active debris removal, space exploration, and robotic assembly domains. Four key findings emerge from this comprehensive analysis.

**Finding 1: The Fragmentation Paradox Demands Soft Capture Solutions.** The space debris environment has reached a critical state: over 54,000 tracked objects larger than 10 cm, an estimated 140 million fragments between 1 mm and 1 cm, and a total orbital mass exceeding 15,800 tonnes [ESA Space Debris Office \[2025\]](#). Active debris removal at the rate of at least 5 large objects per year is required to stabilize the LEO population [Liou et al. \[2010\]](#). Yet the dominant ADR approach—rigid robotic capture, as exemplified by ClearSpace-1—carries an unquantified but non-trivial fragmentation risk for tumbling targets (Section 3.1). Rigid capture of a debris object could generate new fragments, potentially exacerbating the very problem it aims to solve. Soft and compliant capture mechanisms (Section 3.2), by absorbing kinetic energy rather than transmitting contact impulses, offer a system-level safety margin that rigid capture cannot provide. The absence of a quantitative soft-versus-rigid fragmentation comparison (gap C1) is the single most important open research question identified by this survey. Until this comparison is performed, the ADR community is selecting capture mechanisms without the fundamental dataset needed for informed technology selection.

**Finding 2: Inflatable Habitats Are Flight-Proven, with a Clear Path to Deep-Space Application.** BEAM’s 8+ years of continuous operation on the International Space Station has conclusively demonstrated that pressure-stabilized inflatable modules can survive the LEO environment at TRL 9 (Section 4.1). The mass efficiency advantage is decisive:  $39 \text{ kg m}^{-3}$  for TransHab versus  $137\text{--}205 \text{ kg m}^{-3}$  for metallic ISS modules [Valle et al. \[2019a\]](#). Vectran-based restraint layers provide specific strengths exceeding  $2300 \text{ kN m kg}^{-1}$ , an order of magnitude beyond aerospace metals (Section 5.1). Current commercial programmes (Sierra Space LIFE) have demonstrated full-scale burst pressures of 77 psi, exceeding NASA structural requirements by 27% (Section 4.2). The path from BEAM to deep-space habitats requires addressing three challenges: radiation shielding (BEAM’s  $8\text{--}10\times$  higher SPE dose versus metallic modules; Section 4.4), autonomous deployment reliability (BEAM’s 25-burst, 7-hour deployment was rescued by ISS crew; Section 6.3), and the  $19\times$  volume scale-up from BEAM’s  $16 \text{ m}^3$  to a  $300+\text{ m}^3$  deep-space transit habitat. Each challenge is substantive but bounded, with identified mitigation strategies (water-wall radiation shielding, deployment sequencing control, and multi-layer restraint engineering, respectively).

**Finding 3: The Space Vacuum Is a Resource, Not Merely an Obstacle.** The traditional framing of the space environment as hostile to soft robotics—pneumatic actuation loses its working medium, elastomers outgas, lubricants evaporate—is being overturned by three developments. First, vacuum-gap electrostatic actuators [Sirbu et al. \[2025\]](#) achieve  $>4 \text{ N}$  force at  $0.7 \text{ g}$  mass with  $>100 \text{ Hz}$  bandwidth by using internal vacuum gaps as func-

2442 tional elements; these actuators *require* vacuum and are simpler in orbit than on Earth  
2443 (Section 7.2). Second, the jamming-in-vacuum principle exploits the ambient orbital vac-  
2444 uum as the external low-pressure reservoir for granular or layer jamming, eliminating the  
2445 vacuum pump required in terrestrial implementations (Section 7.6); this remains a logical  
2446 deduction requiring experimental validation (gap M1), but the physics is straightforward.  
2447 Third, the very existence of pressure-stabilized inflatable structures depends on the vacuum  
2448 environment providing the pressure differential that creates structural stiffness. Together,  
2449 these observations suggest that soft inflatable robotic systems for space constitute a distinct  
2450 engineering discipline—not merely terrestrial soft robotics adapted for space, but a field  
2451 where the space environment enables capabilities impossible on Earth.

2452 **Finding 4: The Critical Barrier Is System Integration, Not Individual Technol-**  
2453 **ogy Maturity.** Perhaps the most significant finding of this survey is negative: no single  
2454 technology gap is a showstopper for the field. Vectran and Kevlar are flight-proven for inflat-  
2455 able structures (TRL 9). SMA deployment mechanisms are flight-proven (TRL 8–9). FBG  
2456 sensors have flown on Proba-2 (TRL 7–8). iROSA-class flexible photovoltaics power the  
2457 ISS (TRL 9). Loop heat pipes transport multi-kilowatt thermal loads (TRL 9). Reaction  
2458 wheels provide attitude control for the largest operational spacecraft (TRL 9). The barrier  
2459 is at the *interfaces*: no programme has integrated FBG sensors into an inflatable structure  
2460 for flight; no programme is developing photovoltaics on inflatable substrates; no theory ad-  
2461 dresses AOCS for pressure-stabilized membranes; no interface enables rigid module assembly  
2462 onto flexible platforms. The field suffers from a fragmentation of its own—not of debris, but  
2463 of research communities. Soft roboticists, inflatable structure engineers, space power spe-  
2464 cialists, and GNC researchers each advance their disciplines without the cross-disciplinary  
2465 programmes needed to integrate their outputs into flight-ready systems.

2466 This survey has attempted to bridge that fragmentation by reviewing all eight enabling  
2467 technology areas through a single lens: the unifying thesis that the same high-strength fabric  
2468 technologies (Vectran, Kevlar, Nextel) serve both active debris removal and space exploration  
2469 applications. The cross-domain connections identified throughout—thermal management  
2470 informing actuator design (Section 10), MMOD protection materials serving as actuation  
2471 substrates (Section 5), FBG sensing unifying habitat SHM and robotic proprioception (Sec-  
2472 tion 8.1), and the drag–power–thermal cascade governing 100-metre-class platform architec-  
2473 ture (Section 11.3)—are insights that emerge only from the breadth of an integrative review.  
2474 They cannot be seen from within any single technology discipline.

2475 The research roadmap proposed in Section 13.3 identifies concrete near-term actions:  
2476 jamming-in-vacuum validation, FBG flight demonstration on inflatable webbing, perovskite/CIGS  
2477 fold-deploy testing, rigid-flexible interface prototyping, and gyroelastic theory extension. The  
2478 most flight-ready integrated demonstrator—a gecko-adhesive gripper on an inflatable arm  
2479 with FBG structural health monitoring—could fly within 3–5 years of programme initia-  
2480 tion, generating the first orbital dataset on soft inflatable robotic capture. The longer-term  
2481 vision—a 10-metre inflatable with integrated photovoltaics, assembly robots operating on  
2482 inflatable platforms, and AOCS-qualified pressure-stabilized structures—defines a 15-year  
2483 trajectory toward operational capability.

2484 The space debris crisis demands action on a timescale shorter than the 15-year technology

2485 roadmap allows. ClearSpace-1 and its successors will fly rigid capture missions within this  
2486 decade. The soft robotics and inflatable structures communities must move from component-  
2487 level demonstration to system-level integration with urgency commensurate with the prob-  
2488 lem. The technologies exist; the integration does not. Closing the integration gaps identified  
2489 in this survey is the defining challenge for the next generation of space robotics research.

## 2490 References

2491 ESA Space Debris Office. ESA space environment report 2025. Technical report, European  
2492 Space Agency, 2025. URL [https://www.esa.int/Space\\_Safety/Space\\_Debris](https://www.esa.int/Space_Safety/Space_Debris). Current  
2493 debris environment statistics: 54,000 tracked objects, 15,800 tonnes, Starlink avoidance  
2494 manoeuvre data.

2495 Donald J. Kessler and Burton G. Cour-Palais. Collision frequency of artificial satellites:  
2496 The creation of a debris belt. *Journal of Geophysical Research*, 83(A6):2637–2646, 1978.  
2497 doi: 10.1029/JA083iA06p02637. Seminal paper predicting the debris cascade (Kessler  
2498 syndrome).

2499 Jer-Chyi Liou and Nicholas L. Johnson. Risks in space from orbiting debris. *Science*, 311  
2500 (5759):340–341, 2006. doi: 10.1126/science.1121337. LEGEND simulation demonstrating  
2501 LEO instability even with zero future launches.

2502 Jer-Chyi Liou and Nicholas L. Johnson. Instability of the present LEO satellite popula-  
2503 tions. *Advances in Space Research*, 41(7):1046–1053, 2008. doi: 10.1016/j.asr.2007.04.081.  
2504 Extended 200-year LEGEND projections confirming irrecoverable LEO instability.

2505 Jer-Chyi Liou, Nicholas L. Johnson, and N. M. Hill. Controlling the growth of future LEO  
2506 debris populations with active debris removal. *Acta Astronautica*, 66(5–6):648–653, 2010.  
2507 doi: 10.1016/j.actaastro.2009.08.005. Quantifies the 5 large objects per year ADR require-  
2508 ment to stabilise LEO.

2509 Alexander Ledkov and Vladimir Aslanov. Review of contact and contactless active space  
2510 debris removal approaches. *Progress in Aerospace Sciences*, 134:100858, 2022. doi:  
2511 10.1016/j.paerosci.2022.100858. PiAS ADR review covering nets, harpoons, ion beam  
2512 shepherd, tethers; soft/compliant approaches absent.

2513 Guglielmo S. Aglietti et al. The active space debris removal mission RemoveDebris: Part  
2514 2, in orbit operations. *Acta Astronautica*, 168:310–322, 2020. doi: 10.1016/j.actaastro.  
2515 2019.09.001. Documents RemoveDebris harpoon boom failure at 20 m/s contact velocity;  
2516 in-orbit results.

2517 Gerald D. Valle et al. System integration comparison between inflatable and metallic  
2518 spacecraft structures. In *2019 IEEE Aerospace Conference*, pages 1–10, 2019a. doi:  
2519 10.1109/AERO.2019.8742000. Definitive mass/volume comparison: TransHab 39 kg/m<sup>3</sup> vs  
2520 Columbus 137 kg/m<sup>3</sup> vs Tranquility 205 kg/m<sup>3</sup>. Vectran specific strength 2,330 kN-m/kg.

- 2521 NASA Johnson Space Center. BEAM ISS year-one science results. Technical Report JSC-  
2522 CN-39950, NASA, 2017. BEAM Year-One data: 16 m<sup>3</sup>, 1,415 kg, deployment anomaly  
2523 (25 bursts over 7 hours), September 2017 SPE radiation data (2-2.5 mGy vs 0.25 mGy in  
2524 metallic modules).
- 2525 Angel Flores-Abad, Ou Ma, Khanh Pham, and Steve Ulrich. A review of space robotics  
2526 technologies for on-orbit servicing. *Progress in Aerospace Sciences*, 68:1–26, 2014. doi: 10.  
2527 1016/j.paerosci.2014.03.002. Foundational PiAS review establishing the four-phase capture  
2528 framework; pre-dates soft robotics wave.
- 2529 Zheyao Zhao et al. Robotic manipulators for in-orbit servicing and active debris removal:  
2530 Review and comparison. *Progress in Aerospace Sciences*, 152:101046, 2024. doi: 10.1016/  
2531 j.paerosci.2024.101055. PiAS rigid manipulator review; soft and inflatable manipulators  
2532 are outside scope.
- 2533 Yongchang Zhang, Pengchun Li, Jiale Quan, et al. Progress, challenges, and prospects of  
2534 soft robotics for space applications. *Advanced Intelligent Systems*, 5(3):2200071, 2023a.  
2535 doi: 10.1002/aisy.202200071. Most relevant prior soft-robotics-for-space survey; does not  
2536 cover inflatable platforms, power, thermal, AOCS, or dual application principle.
- 2537 Ion-Dan Sirbu et al. Vacuum-gap electrostatic multilayer actuators for soft robotics in  
2538 space. *Nature Communications*, 16, 2025. doi: 10.1038/s41467-025-66232-7. Break-  
2539 through: vacuum-gap actuators require vacuum to function. 0.7 g mass, >4 N force,  
2540 >100 Hz bandwidth, 1.4 kW/kg. TRL 3-4; no space environment testing reported.
- 2541 Siobhan G. Fitzgerald, Gareth W. Delaney, and David Howard. A review of jamming ac-  
2542 tuation in soft robotics. *Actuators*, 9(4):104, 2020. doi: 10.3390/act9040104. Review of  
2543 jamming mechanisms and variable stiffness. Stiffness ratios >25:1 achievable. Basis for  
2544 space jamming-for-free insight.
- 2545 O. Araromi, I. Gavrilovich, J. Shintake, S. Rosset, M. Richard, V. Gass, and H. Shea.  
2546 Rollable multisegment dielectric elastomer minimum energy structures for a deployable  
2547 microsatellite gripper. *IEEE/ASME Transactions on Mechatronics*, 20(1):438–446, 2015.  
2548 doi: 10.1109/TMECH.2014.2329367. DEMES gripper for CleanSpace One: 860,000+  
2549 cycles, 0.8-2.2 mN force, passive negative feedback in microgravity.
- 2550 NASA. NASA Systems Engineering Processes and Requirements. NPR 7123.1B, 2020.  
2551 Defines the Technology Readiness Level (TRL) scale used throughout this survey.
- 2552 Xiang Wang et al. Compliant capture approaches for active debris removal missions.  
2553 *Aerospace*, 10(1):60, 2023. States explicitly that rigid manipulation has the potential  
2554 to generate fragments during capture.
- 2555 Yan Chen et al. Risks of contact-based caging for tumbling debris targets. arXiv preprint  
2556 arXiv:2405.00943, 2024a. Characterises single contact-based caging as excessively risky  
2557 for fast-tumbling targets.

- 2558 Hao Jiang et al. A robotic device using gecko-inspired adhesives can grasp and ma-  
2559 nipulate large objects in microgravity. *Science Robotics*, 2(7):eaa4545, 2017. doi:  
2560 10.1126/scirobotics.aan4545. Microgravity-validated gecko adhesive gripper: 100% suc-  
2561 cess rate for spheres, up to 400 kg objects. Highest TRL soft capture approach (TRL  
2562 4-5).
- 2563 Paolo Palmieri et al. An inflatable 7-DOF space robotic arm for active debris removal. In  
2564 *CISM International Centre for Mechanical Sciences, Courses and Lectures*, 2023. POPUP  
2565 inflatable 7-DOF arm for ADR; Vectran fabric links; TRL 3.
- 2566 DuPont. Kevlar 49 Aramid Fiber Technical Data Sheet, 2019. Filament-level UTS = 3.6  
2567 GPa; density = 1.44 g/cm<sup>3</sup>; specific strength = 2,500 kN-m/kg at filament level.
- 2568 Sierra Space Corporation. LIFE habitat ultimate burst pressure test results. Corporate press  
2569 release, 2024. LIFE 285: full-scale burst at 77 psi; LIFE 10 (1/3 scale): burst at 255 psi,  
2570 FOS 16× LEO, 23× lunar. Note: corporate press release, not peer-reviewed.
- 2571 Kriss J. Kennedy. Lessons from TransHAB: An architect’s experience. In *AIAA Space*  
2572 *Architecture Symposium*, number AIAA 2002-6105, 2002. TransHab design philosophy,  
2573 burst tests to 4× operating pressure, restraint-layer preloading for deployment. Primary  
2574 reference for TransHab programme.
- 2575 John W. Norbury et al. Passive shielding materials for space radiation protection: A review.  
2576 *Materials*, 2025. Polyethylene achieves 27.8% mass saving vs aluminium for equivalent  
2577 proton shielding. Three-layer shields: up to 70% TID improvement for electrons.
- 2578 Timothy L. Weadon. Long term loading properties of Vectran fabric for inflatable space  
2579 habitats. Master’s thesis, West Virginia University, 2013. Vectran creep characterisation:  
2580 exponential sensitivity to load level, manufacturing variability ±10% UTS. Primary data  
2581 source for restraint layer lifetime prediction.
- 2582 Roberto Destefanis et al. Enhanced space debris shields for manned spacecraft. In  
2583 *International Journal of Impact Engineering*, volume 29, pages 217–228, 2003. doi:  
2584 10.1016/j.ijimpeng.2003.09.019. Nextel/Kevlar stuffed Whipple shield: protects against  
2585 2× larger projectiles at equal areal density vs standard Whipple.
- 2586 Jun-Ho Cha et al. Inflatable origami multi-shock shield (IMSS) structure for space habitation  
2587 module. In *Proceedings of the 34th Congress of the International Council of Aeronautical*  
2588 *Sciences (ICAS)*, 2024. IMSS: waterbomb tessellation, UHMWPE/Kevlar/Nextel, 90%  
2589 volume savings vs rigid Whipple. Demonstrates origami geometry serving both packaging  
2590 and debris protection simultaneously.
- 2591 Douglas A. Litteken. Inflatable technology: Using flexible materials to make large space  
2592 structures. In *Proceedings of SPIE 10966, Earth and Space 2018*, volume 10966, 2019.  
2593 doi: 10.1117/12.2500091. Comprehensive heritage review from NASA JSC SME: Echo to  
2594 BEAM, including Mars lander airbags with Vectran, structural design principles.

- 2595 Koryo Miura. Method of packaging and deployment of large membranes in space. Technical  
2596 Report 618, Institute of Space and Astronautical Science, 1985. Foundational Miura-ori  
2597 fold pattern: single-actuator, rigid-foldable, unlimited compaction.
- 2598 Mark Schenk, Andrew D. Viquerat, Keith A. Seffen, and Simon D. Guest. Review of inflat-  
2599 able booms for deployable space structures: Packing and rigidization. *Journal of Spacecraft*  
2600 *and Rockets*, 51(3):762–778, 2014. doi: 10.2514/1.A32598. Review of packaging ratios for  
2601 inflatable booms; cylindrical adaptations of Miura-ori; rigidization classification.
- 2602 Felix Lang et al. Proton radiation hardness of perovskite tandem photovoltaics. *Joule*, 4(5):  
2603 1054–1069, 2020. doi: 10.1016/j.joule.2020.03.012. Perovskite/CIGS tandem: 2,100 W/kg  
2604 with 25  $\mu\text{m}$  substrate, >85% retention after >50 year LEO-equivalent proton irradiation.  
2605 Key enabler for inflatable-integrated PV.
- 2606 William Foster-Hall, David Harvey, Ling Yin, and Rini Akmeliawati. Soft robotics for space  
2607 applications: Cryogenic performance of modular metallic cable structures. *Soft Robotics*,  
2608 2025. doi: 10.1177/21695172251364758. Metallic cable-based soft robots: only 5% stiff-  
2609 ness increase over 100 cycles at  $-196^\circ\text{C}$ . Solves elastomer embrittlement for deep-space  
2610 applications.
- 2611 Wei Zhang, Feng Li, Junlin Li, and Qinkun Cheng. Review of on-orbit robotic arm active de-  
2612bris capture removal methods. *Aerospace*, 10(1):13, 2022. doi: 10.3390/aerospace10010013.
- 2613 Andrea Stolfi, Paolo Gasbarri, and Marco Sabatini. A combined impedance-pd approach  
2614 for controlling a dual-arm space manipulator in the capture of a non-cooperative target.  
2615 *Frontiers in Robotics and AI*, 4:34, 2017. doi: 10.1016/j.actaastro.2017.07.014.
- 2616 Aerospace Corporation. IMPACT satellite breakup model. Technical report, The Aerospace  
2617 Corporation, 2020. Catastrophic fragmentation threshold: 10 J/g specific energy.
- 2618 ClearSpace SA and European Space Agency. ClearSpace-1: ESA’s first space debris re-  
2619 moval mission. [https://www.esa.int/Space\\_Safety/ClearSpace-1](https://www.esa.int/Space_Safety/ClearSpace-1), 2020. Contract  
2620 value €86M; target changed from VESPA to Proba-1; launch  $\sim$ 2029.
- 2621 Nicholas L. Johnson, Paula H. Krisko, J.-C. Liou, and Phillip D. Anz-Meador. NASA’s new  
2622 breakup model of EVOLVE 4.0. *Advances in Space Research*, 28(9):1377–1384, 2001. doi:  
2623 10.1016/S0273-1177(01)00423-9. Original experimental basis for the 10 J/g catastrophic  
2624 fragmentation threshold.
- 2625 Jun Shintake, Vito Cacucciolo, Dario Floreano, and Herbert Shea. Soft robotic grippers.  
2626 *Advanced Materials*, 30(29):1707035, 2018. doi: 10.1002/adma.201707035.
- 2627 Yuhang Liu, Kai Luo, Shuai Wang, Xiping Song, and Zhijuan Zhang. A soft and bistable  
2628 gripper with adjustable energy barrier for fast capture in space. *Soft Robotics*, 10(1):77–87,  
2629 2022. doi: 10.1089/soro.2021.0147.
- 2630 Yongchang Zhang, Jiale Quan, Pengchun Li, Wenping Song, and Guozheng Zhang. A flytrap-  
2631 inspired bistable origami-based gripper for rapid active debris removal. *Advanced Intelli-*  
2632 *gent Systems*, 5(7):2200468, 2023b. doi: 10.1002/aisy.202200468.

2633 Miguel Ruiz Vincueria et al. A thermally-resilient multi-layered soft gripper for space appli-  
2634 cations. *arXiv preprint*, 2023. arXiv:2311.08942; accepted IROS 2024.

2635 CT Ingénierie, AirCaptif, and CNES. INSIDeR: Innovative Net and Space Inflatable struc-  
2636 ture for active Debris Removal. In *Proceedings of the 7th European Conference on Space*  
2637 *Debris (SDC7)*, number Paper 714. ESA, 2017.

2638 CT Ingénierie, AirCaptif, CNES, and ESA. INSIDeR: Ground demonstrator development  
2639 and net capture simulations. In *Proceedings of the 8th European Conference on Space*  
2640 *Debris (SDC8)*, number Paper 91. ESA, 2021.

2641 J. L. Arnold, Eric L. Christiansen, A.J. Davis, James L. Hyde, Dana M. Lear, J.-C. Liou,  
2642 Frankel Lyons, Thomas G. Prior, George Studor, Martin Ratliff, Shannon Ryan, F. Gio-  
2643 vane, and B. Corsaro. Handbook for designing MMOD protection. Technical Report  
2644 NASA/TM-2009-214785, NASA, 2009.

2645 Roberto Destefanis, Frank Schaefer, Michel Lambert, and Michel Faraud. Selecting enhanced  
2646 space debris shields for manned spacecraft. *International Journal of Impact Engineering*,  
2647 33(1–12):219–230, 2006. doi: 10.1016/j.ijimpeng.2006.09.065.

2648 NASA. NextSTEP-2 partners develop ground prototypes for deep space habitats. <https://www.nasa.gov/nextstep>, 2016. Six companies selected August 2016: Bigelow, Boeing,  
2649 Lockheed Martin, Orbital ATK, Sierra Nevada, NanoRacks.

2651 Lockheed Martin. Bursting the bubble with inflatable habi-  
2652 tats. [https://www.lockheedmartin.com/en-us/news/features/2022/  
2653 bursting-the-bubble-with-inflatable-habitats.html](https://www.lockheedmartin.com/en-us/news/features/2022/bursting-the-bubble-with-inflatable-habitats.html), 2022. Burst pressure  
2654 285 psi; Waterton Canyon facility; NextSTEP-2 prototype.

2655 Hassell Studio and European Space Agency. Inflatable lunar habitat at Shackleton crater,  
2656 2024. Scalable inflatable pod system; regolith 3D printing; capacity up to 144 people.

2657 Skidmore, Owings & Merrill and European Space Agency. Moon village habitat concept,  
2658 2019. Semi-inflatable shell; 4-person crew; 300-day missions.

2659 European Space Agency. Pneumocell: Inflatable lunar habitat for regolith burial, 2018.  
2660 Designed for burial under 4–5 m of regolith for radiation protection.

2661 NASA. LOFTID: Low-earth orbit flight test of an inflatable decelerator. [https://www.  
2662 nasa.gov/mission/loftid/](https://www.nasa.gov/mission/loftid/), 2022. 6 m diameter; orbital reentry at Mach 30; November  
2663 2022.

2664 ESA/ESTEC. First European workshop on inflatable space structures, 2002. ESA-WPP-200;  
2665 Noordwijk, The Netherlands.

2666 G. D. Valle, D. Litteken, and T. Jones. Review of habitable softgoods inflatable design,  
2667 analysis, testing, and potential space applications. In *AIAA SciTech 2019 Forum*, 2019b.  
2668 doi: 10.2514/6.2019-1528. AIAA 2019-1528.

- 2669 R. Destefanis et al. Space environment characterisation of Kevlar. In *ESA-ESTEC ISME-09*,  
2670 2009.
- 2671 Toyobo Co., Ltd. ZYLON (PBO fiber) technical information. Technical report, Toyobo Co.,  
2672 Ltd., 2005.
- 2673 M. A. Said, B. Dingwall, A. Gupta, A. M. Seyam, G. N. Mock, and T. Theyson. Investigation  
2674 of ultra violet (UV) resistance for high performance fibers. *Advances in Space Research*,  
2675 37(11):2052–2058, 2006. Independent UV degradation data for PBO (Zylon) fibre.
- 2676 E. Christiansen and B. Davis. Heat-cleaned Nextel in MMOD shielding. In *NASA/JSC*,  
2677 2019. NTRS 20190033497.
- 2678 Roger C. Linton, Ann F. Whitaker, and Miria Finckenor. Space environment durability of  
2679 beta cloth in LDEF thermal blankets. In *NASA Conference Publication*, 1993. NTRS  
2680 19940026510.
- 2681 B. A. Banks, K. K. de Groh, and S. K. Miller. Low Earth orbital atomic oxygen interactions  
2682 with materials. Technical report, NASA Glenn Research Center, 2004. NASA/TM-2004-  
2683 213400.
- 2684 M. M. Finckenor and D. Dooling. Multilayer insulation material guidelines. Technical report,  
2685 NASA Marshall Space Flight Center, 1999. NASA/TP-1999-209263.
- 2686 K. J. Kennedy. TransHab inflatable habitat case study. Technical report, NASA, 2016.  
2687 NTRS 20160011581.
- 2688 J. Edgecombe, H. DeLaFuente, and Gerald D. Valle. Damage tolerance testing of a NASA  
2689 TransHab derivative woven inflatable module. In *NASA*, 2009. doi: 10.2514/6.2009-2167.  
2690 NTRS 20090014832.
- 2691 D. G. Gilmore. *Spacecraft Thermal Control Handbook, Volume I: Fundamental Technologies*.  
2692 The Aerospace Press, 2nd edition, 2002.
- 2693 D. Cadogan and S. E. Scarborough. Rigidizable materials for use in gossamer space inflatable  
2694 structures. In *42nd AIAA/ASME/ASCE/AHS/ASC Structures, Structural Dynamics, and*  
2695 *Materials Conference*, 2001. AIAA 2001-1417.
- 2696 Andrew D. Viquerat et al. InflateSail de-orbit flight demonstration results and follow-on  
2697 drag sail applications. *Acta Astronautica*, 162:203–219, 2019. doi: 10.1016/j.actaastro.  
2698 2019.06.005. InflateSail (2017): 1 m Al-Mylar boom, 10 m<sup>2</sup> sail, 72-day deorbit from 505  
2699 km. TRL 8-9 for strain-rigidised CubeSat booms.
- 2700 C. Underwood, A. Viquerat, M. Schenk, S. Fellowes, B. Taylor, Chiara Massimiani, Richard  
2701 Duke, Brian Stewart, C. Bridges, D. Masutti, and A. Denis. The InflateSail CubeSat  
2702 mission: The first European demonstration of drag-sail de-orbiting. In *4S Symposium*,  
2703 2017.

- 2704 B. Defoort, V. Peypoudat, M. Bernasconi, K. Chuda, and X. Coqueret. Recent advances in  
2705 the rigidization of gossamer structures. In *45th AIAA/ASME/ASCE/AHS/ASC Struc-*  
2706 *tures, Structural Dynamics, and Materials Conference*, 2005. doi: 10.1007/1-4020-3317-6\_  
2707 16. AIAA 2004-1561.
- 2708 R. Allred et al. UV rigidizable carbon-reinforced isogrid inflatable booms. In *43rd*  
2709 *AIAA/ASME/ASCE/AHS/ASC Structures, Structural Dynamics, and Materials Confer-*  
2710 *ence*, 2002. AIAA 2002-1202.
- 2711 Adherent Technologies Inc. Rigidization on command (ROC) materials for inflatable space-  
2712 craft. In *SAE Technical Paper*, 2001. doi: 10.4271/2001-01-2220. 2001-01-2220.
- 2713 Vikas Rastogi, Sanjay H. Upadhyay, and Kripa Sankar Singh. Rigidization analysis of SMA-  
2714 based inflatable toroidal space structures. *Mechanics Based Design of Structures and*  
2715 *Machines*, 52(11), 2024. doi: 10.1080/15397734.2024.2345375.
- 2716 R. Verker, E. Keren, N. Refaeli, Y. Carmiel, A. Bolker, D. David, S. Katz, E. Sagi, D. Bashi,  
2717 I. Finkelstein, T. Nahum, A. Haran, A. Shemesh Sadeh, M. Ariel, I. Gouzman, O. Amrani,  
2718 Y. Simhony, and M. Murat. Measurements of material erosion in space by atomic oxygen  
2719 using the on-orbit material degradation detector. *Acta Astronautica*, 2023. doi: 10.1016/  
2720 j.actaastro.2023.07.020.
- 2721 R. Zhai, Xiaoning Yang, Lixiang Jiang, Hong Gao, Yuxin Zhang, and Zi-Long Jiao. Syner-  
2722 gistic effects of atomic oxygen and thermal cycling in low earth orbit on polymer-matrixed  
2723 space material. *Polymers*, 2023. doi: 10.1016/j.heliyon.2023.e17431. PMC 10404884.
- 2724 M. Schenk, S. Kerr, A. M. Smyth, and S. Guest. Inflatable cylinders for deployable space  
2725 structures. In *Proc. Transformables 2013*, 2013.
- 2726 C. H. M. Jenkins. *Gossamer Spacecraft: Membrane and Inflatable Structures Technology for*  
2727 *Space Applications*, volume 191 of *Progress in Astronautics and Aeronautics*. AIAA, 2001.  
2728 doi: 10.2514/4.866616.
- 2729 A. C. Horn. A low cost inflatable CubeSat drag brake utilizing sublimation. Master’s thesis,  
2730 Old Dominion University, 2017.
- 2731 D. P. Cadogan, S. E. Scarborough, J. K. Lin, and G. H. Sapna. PowerSphere multifunctional  
2732 ultraviolet-rigidizable inflatable structures. *Journal of Spacecraft and Rockets*, 43(5), 2006.
- 2733 Na Li, Haijun Peng, and Fei Li. Instantaneous optimal control of inflatable folded structures.  
2734 *Acta Astronautica*, 194:52–62, 2022a. doi: 10.1016/j.actaastro.2022.02.024.
- 2735 S. J. Hughes, R. A. Dillman, B. R. Starr, R. A. Stephan, M. C. Lindell, C. J. Player, and F. M.  
2736 Cheatwood. Inflatable re-entry vehicle experiment (irve) design overview. In *18th AIAA*  
2737 *Aerodynamic Decelerator Systems Technology Conference*, 2005. doi: 10.2514/6.2005-1636.  
2738 AIAA 2005-1636.

- 2739 Thomas W. Murphey, Jeremy A. Banik, and Sergio Pellegrino. TRAC boom technology.  
2740 *AIAA SciTech Forum*, (AIAA 2015-0434), 2015. Triangular Rollable and Collapsible  
2741 boom: primary competitor to inflatable booms for CubeSat-class deployables.
- 2742 Jeremy A. Banik and Thomas W. Murphey. Performance validation of the triangular rollable  
2743 and collapsible mast. In *AIAA Structures, Structural Dynamics, and Materials Conference*,  
2744 number AIAA 2010-2585, 2010.
- 2745 C. Sickinger and L. Herbeck. Deployment strategies, analyses, and tests for the CFRP booms  
2746 of a solar sail. In *ESA SP-561*, 2004. CFRP boom deployment for solar sails.
- 2747 J. Santiago-Prowald and G. Rodrigues. Deployable antennas. In *Handbook of Antenna*  
2748 *Technologies*. Springer, 2018. Comprehensive comparison of mesh, solid, and inflatable  
2749 antenna architectures.
- 2750 O. A. Araromi, I. Gavrilovich, J. Shintake, S. Rosset, M. Richard, V. Gass, and H. R.  
2751 Shea. Towards a deployable satellite gripper based on multisegment dielectric elastomer  
2752 minimum energy structures. In *Proc. SPIE 9056, Electroactive Polymer Actuators and*  
2753 *Devices (EAPAD) 2014*, page 90562G, 2014. doi: 10.1117/12.2044667.
- 2754 Haopeng Liang, Yong Zhao, Bingxiao Du, Wensheng Wu, and Xiaoqian Chen. Design, fabri-  
2755 cation and modeling of a dielectric elastomer tridimensional minimum energy structure for  
2756 space mission. *Sensors and Actuators A: Physical*, 2023. doi: 10.1016/j.sna.2023.114747.
- 2757 A. Punning, K. J. Kim, V. Palmre, F. Vidal, C. Plesse, N. Festin, A. Maziz, K. Asaka,  
2758 T. Sugino, G. Alici, et al. Ionic electroactive polymer artificial muscles in space applica-  
2759 tions. *Scientific Reports*, 4:6913, 2014. doi: 10.1038/srep06913.
- 2760 J. S. Mehling et al. NASA tendril: A slender continuum robot for inspection. Technical  
2761 report, NASA, 2006.
- 2762 X. Ouyang, D. Meng, X. Wang, C. Wang, B. Liang, and N. Ding. Hybrid rigid-continuum  
2763 dual-arm space robots: Modeling, coupling analysis, and coordinated motion planning.  
2764 *Aerospace Science and Technology*, 116:106861, 2021. doi: 10.1016/j.ast.2021.106861.
- 2765 Fernando Ruíz, Begoña C. Arrue, and Ambal Ollero. Thermally-resilient soft gripper for  
2766 on-orbit operations. In *IEEE/RSJ International Conference on Intelligent Robots and*  
2767 *Systems (IROS)*, 2023. doi: 10.48550/arxiv.2311.08942.
- 2768 G. Costanza and M. E. Tata. Shape memory alloys for aerospace, recent developments, and  
2769 new applications: A short review. *Materials*, 13(8), 2020. doi: 10.3390/ma13081856.
- 2770 Alain Blanc, Damien Chassoulier, Fabrice Champandard, and Xavier François. Solar array  
2771 root hinge based on shape memory alloy (SMA) actuator. In *ESMATS*, 2013.
- 2772 Y. Zhang, P. Li, J. Quan, L. Li, G. Zhang, and D. Zhou. Progress, challenges, and prospects  
2773 of soft robotics for space applications. *Advanced Intelligent Systems*, 5(3):2200071, 2023c.  
2774 doi: 10.1002/aisy.202200071.

- 2775 Ahmad Ataka, Peng Qi, Ali Shiva, Ali Shafti, Helge A. Wurdemann, Hongbin Liu, and  
2776 Kaspar Althoefer. Real-time pose estimation and obstacle avoidance of a pneumatic soft  
2777 growing robot. In *IEEE International Conference on Robotics and Automation (ICRA)*,  
2778 2020. Closed-loop pneumatic eversion arm for space-relevant inspection.
- 2779 Elliot W. Hawkes, Laura H. Blumenschein, Joseph D. Greer, and Allison M. Okamura. A  
2780 soft robot that navigates its environment through growth. *Science Robotics*, 2(8), 2017.  
2781 doi: 10.1126/scirobotics.aan3028.
- 2782 Jianglong Guo, Troy Bamber, Kirk Hovell, et al. Electroadhesion technologies for robotics:  
2783 A comprehensive review. *Soft Robotics*, 2020. doi: 10.1109/tro.2019.2956869. Electroad-  
2784 hesion gripping for non-cooperative surfaces.
- 2785 Yoonho Kim, Hyunwoo Yuk, Ruike Zhao, Shawn A. Chester, and Xuanhe Zhao. Printing  
2786 ferromagnetic domains for untethered fast-transforming soft materials. *Nature*, 558:274–  
2787 279, 2018. doi: 10.1038/s41586-018-0185-0.
- 2788 I. Mckenzie, S. Ibrahim, E. Haddad, S. Abad, A. Hurni, and Lun K. Cheng. Fiber optic  
2789 sensing in spacecraft engineering: An historical perspective from the European Space  
2790 Agency. *Frontiers in Physics*, 9:719441, 2021. doi: 10.3389/fphy.2021.719441.
- 2791 S. Girard et al. Radiation effects on fiber Bragg gratings: Vulnerability and hardening  
2792 studies. *Sensors*, 2022.
- 2793 Tamana Baba, N. Saidin, N. F. Hasbullah, and Ishaq Ahmad. Radiation tolerant fiber  
2794 Bragg gratings: Review of FBG sensing. *Journal of Optics*, 2025. doi: 10.1007/  
2795 s12596-025-02861-x.
- 2796 Bally Ribbon Mills and Luna Innovations. Inflatable space habitats use sensors embedded in  
2797 webbing for structural health monitoring. Technical report, NASA SBIR Program, 2020.
- 2798 K. C. Galloway, Y. Chen, E. Templeton, B. Rife, I. S. Godage, and E. J. Barth. Fiber optic  
2799 shape sensing for soft robotics. *Soft Robotics*, 6(5):671–684, 2019. doi: 10.1089/soro.2018.  
2800 0131.
- 2801 Davide Paloschi, Sergei Bronnikov, Kirill Raspopin, et al. 3D shape sensing with multicore  
2802 optical fibers. *IEEE Sensors Journal*, 20(24):14702–14710, 2020. doi: 10.1109/metroind4.  
2803 0iot48571.2020.9138221.
- 2804 Shahriar Sefati, Rachel A. Hegeman, Farshid Alambeigi, et al. FBG-based large deflection  
2805 shape sensing of a continuum manipulator. *IEEE Transactions on Medical Robotics and*  
2806 *Bionics*, 2021. Multicore FBG shape sensing on continuum robots.
- 2807 Ginu Rajan, Madhav Ramakrishnan, Yuliya Semenova, Eliathamby Ambikairajah, Ger-  
2808 ald Farrell, and Gang-Ding Peng. Overview of fiber optic sensor technologies for  
2809 strain/temperature sensing applications in composite materials. *Sensors*, 21(4):1–25, 2021.  
2810 Comprehensive review of FBG sensing for structural health monitoring.

- 2811 A. M. White, Isaac Little, Anastasiya Artyuk, Nicholas McKibben, Fereshteh Rajabi Kouchi,  
2812 Claire Chen, David Estrada, and Zhangxian Deng. On-demand fabrication of piezoelectric  
2813 sensors for in-space structural health monitoring. *Advanced Materials*, 2024. doi: 10.1088/  
2814 1361-665x/ad3d16.
- 2815 Pengfei Li, Suyu Xu, Chao Xu, Fei Du, and Shancheng Cao. Development of a miniature  
2816 dynamic stiffness measurement prototype toward structural health monitoring of space  
2817 inflatable structures. *Measurement*, 2022b. doi: 10.1016/j.measurement.2022.111051.
- 2818 Brian R. Spence, Steven White, Michael LaPointe, Steven Kiefer, Paul LaCorte, Jeremy  
2819 Banik, Darren Chapman, and Jay Merrill. International space station (ISS) roll-out so-  
2820 lar array (ROSA) spaceflight experiment mission and results. In *2018 IEEE Aerospace*  
2821 *Conference*, pages 1–13. IEEE, 2018. doi: 10.1109/AERO.2018.8396796.
- 2822 Baochen Yan et al. Development and challenges of large space flexible solar arrays. *Space*  
2823 *Solar Power and Wireless Transmission*, 2:33–42, 2025. doi: 10.1016/j.sspt.2024.12.001.
- 2824 Hyun-Deok Kim et al. Flexible perovskite/CIGS tandem solar cells with record specific  
2825 power. *Joule*, 2024. 23.6% efficiency, 6,150 W/kg cell-level specific power, 100,000 bending  
2826 cycles.
- 2827 David P. Cadogan, Christina Withrow, John Keller, and Barmac K. Taleghani. Development,  
2828 design, and testing of PowerSphere multifunctional ultraviolet-rigidizable inflatable struc-  
2829 tures. *Journal of Spacecraft and Rockets*, 43(5):1049–1056, 2003. doi: 10.2514/1.19882.
- 2830 David Scheiman, Phillip Jenkins, David Brinker, and Joseph Appelbaum. Low-intensity  
2831 low-temperature (LILT) measurements and coefficients on new photovoltaic structures for  
2832 the PowerSphere concept. *Thin Solid Films*, 480–481:61–66, 2005.
- 2833 Phillip P. Jenkins et al. PowerSphere thermal cycling results. Technical Report NASA/TM-  
2834 2009-215511, NASA Glenn Research Center, 2009.
- 2835 Kneev Sharma and A. Santasalo-Aarnio. Energy storage systems for space applications.  
2836 *Journal of Energy Storage*, 120:116315, 2025. doi: 10.1016/j.est.2025.117131.
- 2837 J. Arenberg, J. Flynn, A. Cohen, R. Lynch, and J. Cooper. Status of the JWST sunshield  
2838 and spacecraft. In *Proc. SPIE 8442, Space Telescopes and Instrumentation 2012*. SPIE,  
2839 2016. doi: 10.1117/12.928154.
- 2840 Hyunsu Kim, Kevin Cheung, Raymond C. Y. Auyeung, David E. Wilson, Kristin M. Charipar,  
2841 Alberto Piqué, and Nicholas A. Charipar. VO<sub>2</sub>-based switchable radiator for space-  
2842 craft thermal control. *Scientific Reports*, 9:11329, 2019. doi: 10.1038/s41598-019-47572-z.
- 2843 Almamoun Hendaoui, Nath Emond, Mohamed Chaker, and Emile Haddad. VO<sub>2</sub>-based smart  
2844 coatings with improved emittance-switching properties for an energy-efficient near room-  
2845 temperature thermal control of spacecrafts. *Solar Energy Materials and Solar Cells*, 117:  
2846 494–498, 2013. doi: 10.1016/j.solmat.2013.07.023.

- 2847 Yury F. Maydanik. Loop heat pipes. *Applied Thermal Engineering*, 25(5–6):635–657, 2005.  
2848 doi: 10.1016/j.applthermaleng.2004.07.010.
- 2849 B. Diaconu, M. Cruceru, and L. Angheliescu. Phase change materials in space systems: Fun-  
2850 damental applications, materials and special requirements—a review. *Acta Astronautica*,  
2851 214:60–77, 2023. doi: 10.1016/j.actaastro.2023.12.040.
- 2852 F. Nicassio, Daniele Fattizzo, Michele Giannuzzi, G. Scarselli, and G. Avanzini. Attitude  
2853 dynamics and control of a large flexible space structure by means of a minimum complexity  
2854 model. *Acta Astronautica*, 200, 2022. doi: 10.1016/j.actaastro.2022.05.047.
- 2855 Gabriele M. T. D’Eleuterio and Peter C. Hughes. Dynamics of gyroelastic continua. *Journal*  
2856 *of Applied Mechanics*, 51(2):415–422, 1984. doi: 10.1115/1.3167639.
- 2857 Gabriele M. T. D’Eleuterio and Peter C. Hughes. Modal parameter analysis of gyroelastic  
2858 continua. *Journal of Applied Mechanics*, 53(4):918, 1986. doi: 10.1115/1.3171874.
- 2859 Gabriele M. T. D’Eleuterio and Peter C. Hughes. Dynamics of gyroelastic spacecraft. *Journal*  
2860 *of Guidance, Control, and Dynamics*, 10(4):401–405, 1987. doi: 10.2514/3.20238.
- 2861 Christopher J. Damaren and Gabriele M. T. D’Eleuterio. Optimal control of large space  
2862 structures using distributed gyricity. *Journal of Guidance, Control, and Dynamics*, 12(5):  
2863 723–731, 1989. doi: 10.2514/3.20474.
- 2864 Pedro Cachim, Wolfgang Kraus, Zachary Manchester, Pedro Lourenço, and Rodrigo Ventura.  
2865 Optimal attitude control of large flexible space structures with distributed momentum  
2866 actuators. In *2025 IEEE Aerospace Conference*, 2024. doi: 10.1109/AERO58975.2025.  
2867 10957060. arXiv:2410.07376.
- 2868 Yifan Jiang, Jun Zhang, Peng Tian, Tengfei Liang, and Zhihui Li. Aerodynamic drag anal-  
2869 ysis and reduction strategy for satellites in very low earth orbit. *Aerospace Science and*  
2870 *Technology*, 126:107389, 2022. doi: 10.1016/j.ast.2022.108077.
- 2871 Tommaso Andreussi, Enrico Ferrato, et al. A review of air-breathing electric propulsion:  
2872 From mission studies to technology verification. *Journal of Electric Propulsion*, 2:24,  
2873 2022. doi: 10.1007/s44205-022-00024-9.
- 2874 Lee H. Sentman. Free molecule flow theory and its application to the determination of aero-  
2875 dynamic forces. *LMSC Technical Report*, (LMSC-448514), 1961. Standard free-molecular-  
2876 flow drag coefficient models.
- 2877 Kenneth Moe and Mildred M. Moe. Gas-surface interactions and satellite drag coefficients.  
2878 *Planetary and Space Science*, 53(8):793–801, 2005. doi: 10.1016/j.pss.2005.03.005.
- 2879 Manuel Stein and John M. Hedgepeth. Analysis of partly wrinkled membranes. Technical  
2880 Report TN D-813, NASA, 1961. Foundational tension-field theory for partially wrinkled  
2881 membranes.

- 2882 D. G. Roddeman, J. Drukker, C. W. J. Oomens, and J. D. Janssen. The wrinkling of thin  
2883 membranes: Part I—theory. *Journal of Applied Mechanics*, 54:884–887, 1987.
- 2884 H. Norman Abramson. *The Dynamic Behavior of Liquids in Moving Containers*. Number  
2885 SP-106. NASA, 1966. Foundational reference for fuel-sloshing dynamics analogy.
- 2886 Tristan Leclercq and Emmanuel de Langre. Vortex-induced vibrations of cylinders bent by  
2887 the flow. *Journal of Fluids and Structures*, 83:371–395, 2018. doi: 10.1016/j.jfluidstructs.  
2888 2018.03.008. Gas-structure coupling relevant to inflated membrane dynamics.
- 2889 NASA. In-space servicing, assembly, and manufacturing (ISAM) state of play—2025 edition.  
2890 Technical Report NASA/TM-20250008988, NASA Space Technology Mission Directorate,  
2891 2025.
- 2892 Wenjiang Li, Li Zhong, Weijun Zhu, Zhiyou Xu, Qiang Tang, and Wei Zhan. A survey  
2893 of space robotic technologies for on-orbit assembly. *Space: Science & Technology*, 2022:  
2894 9849170, 2022c. doi: 10.34133/2022/9849170.
- 2895 William Doggett et al. NASA puts in-space assembly robots to the test  
2896 (CIRAS/TALISMAN/SAMURAI/NINJAR). Technical report, NASA Langley Research  
2897 Center, 2018.
- 2898 Mathieu Rognant et al. Autonomous assembly of large structures in space (PULSAR  
2899 project). In *8th European Conference for Aeronautics and Space Sciences (EUCASS)*,  
2900 2019. doi: 10.13009/eucass2019-685.
- 2901 Aadarsh Nair et al. Design engineering a walking robotic manipulator for in-space assembly  
2902 missions (E-Walker). *Frontiers in Robotics and AI*, 9, 2022. doi: 10.3389/frobt.2022.  
2903 941672.
- 2904 Aadarsh Nair et al. The new era of walking manipulators in space: Feasibility and operational  
2905 assessment of assembling a 25 m LAST in orbit. *Acta Astronautica*, 2024. doi: 10.1016/j.  
2906 actaastro.2024.10.002.
- 2907 Shuai Liu, Enyang Zhang, Zhenbang Xu, and Jingxu Zhang. Design of docking interfaces for  
2908 on-orbit assembly of large structures in space. *Sensors*, 24(20):6534, 2024. doi: 10.3390/  
2909 s24206534.
- 2910 Robert E. Skelton and Mauricio C. de Oliveira. *Tensegrity Systems*. Springer, 2009. doi:  
2911 10.1007/978-0-387-74242-7. Foundational reference for rigid-to-flexible structural connec-  
2912 tions.
- 2913 Andrew P. Sabelhaus, Jonathan Bruce, Ken Caluwaerts, et al. System design and locomotion  
2914 of SUPERball, an untethered tensegrity robot. In *IEEE International Conference on*  
2915 *Robotics and Automation (ICRA)*, 2015. NASA Ames tensegrity robot with rigid-bar to  
2916 cable-net interfaces.

- 2917 Juan M. Fernandez, Vaios J. Lappas, and Andrew J. Daton-Lovett. Completely stripped  
2918 solar sail concept using bi-stable reeled composite booms. *Acta Astronautica*, 69:78–85,  
2919 2014. Boom-membrane attachment analysis for solar sails.
- 2920 Huaiming Chen et al. Design and analysis of androgynous docking interface for in-space  
2921 assembly. *Sensors*, 24(20), 2024b.
- 2922 Wei-Jie Li, Da-Yi Cheng, Xin-Gang Liu, Yan-Bin Wang, Wen-Hao Shi, Zhi-Xiang Tang,  
2923 Feng Gao, Fa-Ming Zeng, Hong-Yu Chai, Wen-Bo Luo, Qi Cong, and Zhong-Liang Gao.  
2924 On-orbit service (OOS) of spacecraft: A review of engineering developments. *Progress in*  
2925 *Aerospace Sciences*, 108:32–120, 2019. doi: 10.1016/j.paerosci.2019.01.004.